UNIVERSITY OF OKLAHOMA

GRADUATE COLLEGE

MID-INFRARED EMITTER TECHNOLOGY

A DISSERTATION

SUBMITTED TO THE GRADUATE FACULTY

in partial fulfillment of the requirements for the

degree of

Doctor of Philosophy

By

CHUN YAO
Norman, Oklahoma
2006

Downloaded from SHAREOK. Persistent Handle URL: https://hdl.handle.net/11244/1104

UMI Number: 3237837



UMI Microform 3237837

Copyright 2007 by ProQuest Information and Learning Company.
All rights reserved. This microform edition is protected against
unauthorized copying under Title 17, United States Code.

ProQuest Information and Learning Company
300 North Zeeb Road
P.O. Box 1346
Ann Arbor, MI 48106-1346

MID-INFRARED EMITTER TECHNOLOGY

A DISSERTATION APPROVED FOR THE
SCHOOL OF ELECTRICAL AND COMPUTER ENGINEERING

BY

_____
Dr. Patrick J. McCann, Chair

_____
Dr. Chen Ling

_____
Dr. James J. Sluss

_____
Dr. Hong Liu

_____
Dr. Monte Tull

©Copyright by CHUN YAO 2006
All Rights Reserved.

ACKNOWLEDGEMENTS

I would like to express my deep gratitude to my graduate and dissertation advisor, Dr. Patrick McCann, for his guidance, assistance, encouragements and his generous support throughout this research. I would like to express my thanks to Dr. James Sluss, Dr. Chen Ling, Dr. Monte Tull, and Dr. Hong Liu for accepting to serve on my dissertation committee.

I would also like to thank all the Ekips Technologies employees and Solid State Device Research Group members for their friendship and support. Special thanks go to Dr. Rui Yang, Dr. Chad Roller, Dr. Khosrow Namjou, Dr. Sheena Murphy, Dr. Yuefa Li and Arnaud Sow for their assistance, their help, and their invaluable advice in my research work.

I dedicate my work to my parents Shuren Yao and Meixian Dong, for if it were not for them I would not have become who I am. It is their love and endless support that got me through my study. I want to thank my wife Yuan Ma for believing in me and for her moral support.

Finally, I would like to thank god for seeing me through my research, for his care, provisions and absolute love towards me and my family.

TABLE OF CONTENTS

ACKNOWLEDGEMENTS iv
TABLE OF CONTENTS v
LIST OF TABLES vii
LIST OF FIGURES viii
ABSTRACT xii
Chapter 1 1
Fabrication, packaging and application of mid-infrared emitter technology 1
1.1 Introduction 1
1.2 Objectives for this project 2
1.3 IV-VI materials system 2
1.4 History of lead salt lasers 6
1.5 Quantum cascade lasers 6
1.6 History of quantum cascade laser development 9
1.8 Laser packaging techniques 14
1.9 Laser applications in gas detection 19
1.10 Dissertation organization 23
Chapter 2 25
Filter wheel based mid-infrared spectrometer 25
2.1 Introduction 25
2.2 Components of the filter wheel mid-infrared spectrometer 26
2.3 Theoretical blackbody power estimation 51
2.4 Estimation of IR-12 emission power between 1873 cm^{-1} to 3658cm^{-1} 56
2.5 Photoluminescence power estimation of IV-VI quantum well W336 58
2.6 Summary and future work 63
Chapter 3 65
Quantum Cascade Laser Packaging 65
3.1 Introduction 65
3.2 First packaged laser with boron nitride heat sink and Au-In metal bonding by epi-side down method 73
3.3 Second packaged laser with the boron nitride heat sink and a special mechanical part design by epi-side down method 84
3.4 Third packaged laser with the copper heat sink and gold wire bonding by epi-side up method 89
3.5 Comparison of different packaging techniques 93
Chapter 4 96
Interband cascade lasers and its application in gas detection 96
4.1 Introduction 96
4.2 Testing equipment 98
4.3 Electrical behavior of quantum cascade lasers 104
4.4 Optical behavior of quantum cascade lasers 106
4.5 Theoretical analysis of gas detection by JPL #J653 115

4.6 Conclusion 121
Chapter 5 123
System setup for a interband cascade laser based hollow waveguide gas sensing system 123
5.1 Introduction 123
5.2 Hollow waveguide structure 124
5.3 Experimental setup 127
5.4 Preamplifier circuit analysis 128
5.5 Beam profile analysis in the optical path 135
5.5.1 Beam width analysis in region D 138
5.5.2 Beam shape analysis in region D 143
5.6 The whole optical setup and tested results 148
5.7 Using a ball lens to narrow the beam width 153
5.8 The whole optical setup with a ball lens 156
5.9 Summary 157
Chapter 6 159
Summary and suggestions for future work 159
REFERENCES 162
APPENDIX A 173
APPENDIX B 178
APPENDIX C 181

LIST OF TABLES

TABLE 2.1: ESTIMATIONS OF EMISSION POWER BETWEEN 1873CM^{-1} AND 3658CM^{-1} (APERTURE DIAMETER = 0.02 MM) 53
TABLE 2.2: TEMPERATURE ESTIMATIONS OF INFRARED BLACKBODY IR-12....55
TABLE 2.3: SUMMARY OF THE POWER ESTIMATION OF W336 PHOTOLUMINESCENCE VERSUS DIFFERENT IR-12 TEMPERATURE 62
TABLE 3 1: COMPARISON OF DIFFERENT PACKAGING TECHNIQUES 94
TABLE 4.1: COMPARISON OF TUNING CAPABILITY OF JPL ICL #J435 AND #J653....114
TABLE 4.2: SUMMARY OF POSSIBLE DETECTION MECHANISM FOR JPL ICL #J653....120
TABLE 5.1: VALUES OF FEEDBACK RESISTOR AND SIMULATED OUTPUT VOLTAGE VS. THREE DIFFERENT INPUT CURRENTS....135
TABLE 5.2: DIAMETER OF THE HOLLOW WAVEGUIDE VERSUS THE OPTIMIZED DISTANCE FROM THE BALL LENS TO THE HOLLOW WAVEGUIDE 156

LIST OF FIGURES

FIGURE 1.1: THE BANDGAP ENERGY VERSUS LATTICE PERIODICITY LENGTH OF SOME SEMICONDUCTOR COMPOUNDS [3] 3
FIGURE 1.2: THE BAND STRUCTURE OF GAAS AND PBSE [4]....4
FIGURE 1.3: THE REFRACTIVE INDEX OF LEAD-SALT MATERIALS [5]....5
FIGURE 1.4: SCHEMATIC OF INTRABAND TRANSITIONS....7
FIGURE 1.5: SCHEMATIC OF INTERBAND TRANSITIONS 8
FIGURE 1.6: SCHEMATIC OF N-TYPE QUANTUM CASCADE LASER BASED ON INTERBAND QUANTUM WELLS [13]....9
FIGURE 1.7: TEMPERATURE TUNING PROFILE (91-107K) OF AN INTERBAND QUANTUM CASCADE LASER (JPL ICL #J653) IN 2002 12
FIGURE 1.8: CURRENT TUNING PROFILE OF PBTE-PBEUTESE MESA STRUCTURE LASER IN 1989 [24]....13
FIGURE 1.9: A. SEM OF AU-20SN SURFACE B. SEM OF AU-39SN SURFACE C. SEM OF AU-71SN SURFACE [25]....14
FIGURE 1.10: A. SEM PICTURE OF CU-SN B. SEM PICTURE OF AG-SN BONDING....15
FIGURE 1.11: SCANNING ELECTRON MICROSCOPIC CROSS-SECTIONAL VIEW OF A CLEAVED FILM OF PBSE MQW ATTACHED ONTO A SEPARATED COPPER BAR USING NI/AU/IN-SN/IN/IN-SN/AU/NI BONDING METALLURGY [27]....15
FIGURE 1.12: SCHEMATIC DIAGRAM OF A DIMENSIONAL STABILITY TEST VEHICLE WITH HIGH CTE MISMATCHES [28]....16
FIGURE 1.13: A DESIGN OF DISTRIBUTED FEEDBACK IN QUANTUM CASCADE LASER [30]..18
FIGURE 1.14: SCHEMATIC OF THE BREATH-COLLECTION APPARATUS AND THE TLAS SYSTEM EQUIPPED WITH A IV–VI MID-IR LASER [31] 20
FIGURE 1.15: MEASURED SECOND-HARMONIC ABSORPTION FEATURES OF NO (1912.79 CM^{-1}) FOR CONCENTRATIONS OF 50, 124, 244, AND 475 PPB [31] 21
FIGURE 1.16: SIGNAL TO NOISE VS ETHANOL VAPORS CONCENTRATION IN PPM [32]....22
FIGURE 2.1: PICTURE OF FILTER WHEEL BASED MID-INFRARED SPECTROMETER....27
FIGURE 2.2: SCHEMATIC OF BI-CONVEX LENS....28
FIGURE 2.3: TRANSMITTANCE OF THE CAF_2 BI-CONVEX LENS [34] 29
FIGURE 2.4: SCHEMATIC OF CONCAVO-CONVEX LENS SHOWING THE FOCAL LENGTH....29
FIGURE 2.5: TRANSMITTANCE OF ZINC SELENIDE LENS [34]....30
FIGURE 2.6: A FRONT VIEW OF CIRCULAR VARIABLE FILTER WHEEL IN THE SPECTROMETER 31
FIGURE 2.7: HALF SEGMENT OF FILTER WHEEL SHOWING THE LINEAR VARIATION OF THE FILM THICKNESS WITH THE ANGULAR POSITION [36]....32
FIGURE 2 8: (A) SCHEMATIC OF THE BLACKBODY BEAM PASSING THROUGH THE FILTER WHEEL. (B) COMPARISON OF BLACK BODY RADIATION ON THE FTIR SPECTROMETER BEFORE AND AFTER THE FILTER WHEEL.....33
FIGURE 2.9: TRANSMITTANCE OF THE CIRCULAR VARIABLE FILTER WHEEL FOR EVERY 2 DEGREES [37]....34
FIGURE 2.10: PICTURE OF THE CIRCULAR VARIABLE FILTER WHEEL WITH ITS STAND 35
FIGURE 2.11: MC3479P STEPPER MOTOR [38]....36
FIGURE 2.12: PICTURE OF THE SPECIAL SAMPLE HOLDER 37
FIGURE 2.13: SCHEMATIC OF HEAT DISSIPATION ON THE SPECIAL SAMPLE HOLDER 38
FIGURE 2.14: LDC 3900 DIODE LASER CURRENT SOURCE WITH A TEC TEMPERATURE CONTROLLER.....39
FIGURE 2.15: PICTURE OF THE SPECIAL LASER HOLDER 39
FIGURE 2.16: PICTURE OF AND PVI-2TE-5 TYPE QUANTUM DETECTOR AND ITS CONTROLLER [41] 41
FIGURE 2.17: SPECTRAL RESPONSE OF VARIOUS VIGO SYSTEM DETECTORS AVAILABLE IN INFRARED REGION [41]....42
FIGURE 2.18: PICTURE OF A HP OSCILLOSCOPE, A FREQUENCY GENERATOR AND SR 830 LOCK-IN AMPLIFIER....43
FIGURE 2.19: SCREEN SHOT OF THE LABVIEW PROGRAM GRAPHICAL USER INTERFACE (GUI)

FOR SPECTROMETER....44
FIGURE 2.20: SCREEN SHOT OF THE CODING ARCHITECTURE IN THE LABVIEW PROGRAM 45
FIGURE 2.21: WINDOWS DISPLAYING THE PICTURE OF THE DATA SAVED DURING THE EXPERIMENT....46
FIGURE 2.22: SCHEMATIC PICTURE OF HAWKEYE TECHNOLOGIES IR-12 SERIES INFRARED EMITTER (ALL THE NUMBERS ARE IN MM.) [43] 47
FIGURE 2.23: EMISSVITY OF HAWKEYE TECHNOLOGIES IR-12 SERIES INFRARED EMITTER [43]....48
FIGURE 2.24: TEMPERATURE VERSUS CURRENT FOR HAWKEYE TECHNOLOGIES IR-12 SERIES INFRARED EMITTER [43] 49
FIGURE 2.25: SPECIAL HOLDER FOR INFRARED BLACKBODY IR-12....50
FIGURE 2.26: SPECIAL HOLDER FOR INFRARED BLACKBODY IR-12....50
FIGURE 2.27: SCHEMATIC OF AN IDEAL BLACKBODY 51
FIGURE 2.28: SCHEMATIC OF WAVELENGTH VERSUS INTENSITY IN CASES OF COLDEST, HOTTEST AND CLASSICAL THEORY 52
FIGURE 2.29: SCHEMATIC OF SOLID ANGLE CALCULATION FOR IR-12 54
FIGURE 2.30: SCHEMATIC OF EXPERIMENTAL SETUP FOR IR-12 EMISSION POWER ESTIMATION....56
FIGURE 2.31: SCHEMATIC OF EXPERIMENTAL SETUP FOR IR-12 EMISSION POWER ESTIMATION....58
FIGURE 2.32: BLACKBODY IR-12 SPECTRUM AT DIFFERENT TEMPERATURES AND PL OF W336 AT 1500 MA OF PUMPING CURRENT ON THE SPECTROMETER 61
FIGURE 3.1: PICTURE OF OZONE GENERATOR (MODEL GL-1, PCI OZONE CORP)....67
FIGURE 3.2: PICTURE OF HUMMER 10.2 SPUTTERING SYSTEM (ANATECH LTD.)....68
FIGURE 3 3: PICTURE OF DENTON VACUUM DV-502A FOR THERMAL METALLIC DEPOSITION 69
FIGURE 3.4: HP 4061A I-V CHARACTERIZATION EQUIPMENT (LEFT) AND ITS LABVIEW INTERFACE (RIGHT)....71
FIGURE 3.5: PICTURE OF TENCOR P-1 LONG SCAN PROFILER....72
FIGURE 3.6: SCHEMATIC OF A SCANNING PROCESS PERFORMED BY TENCOR P-1 LONG SCAN PROFILER 73
FIGURE 3.7: SCHEMATIC OF THE JET PROPULSION LAB QUANTUM CASCADE LASER STRUCTURE....74
FIGURE 3.8: AU-IN PHASE DIAGRAM []....75
FIGURE 3.9: SCHEMATIC OF METAL BONDING DESIGN....75
FIGURE 3.10: SCHEMATIC OF BN PLATE AND PICTURE A STACK OF BN PLATES 76
FIGURE 3.11: SCHEMATIC OF THE BN PLATE AND THE BN SLICES....77
FIGURE 3.12: SCHEMATIC OF HOLES' DRILLING ON BN PIECES....78
FIGURE 3.13: SCHEMATIC FOR SPACER'S PREPARATION....78
FIGURE 3.14: SCHEMATIC OF THE COPPER BARS BINDING....79
FIGURE 3.15: SCHEMATIC OF WIRE SOLDERING....80
FIGURE 3.16: SCHEMATIC OF PHOTORESIST MECHANISM....81
FIGURE 3.17: SCHEMATIC OF WIRE SOLDERING....82
FIGURE 3.18: CURRENT VERSUS VOLTAGE FOR AN EPI-SIDE DOWN PACKAGED QUANTUM CASCADE LASER....83
FIGURE 3.19: FTIR DATA FOR PACKAGED QUANTUM CASCADE LASER 84
FIGURE 3.20: SCHEMATIC OF A SPECIAL MECHANICAL WALL DESIGN FOR SECOND PACKAGING METHOD....85
FIGURE 3.21: FINAL STACK OF A SPECIAL MECHANIC WALL DESIGN FOR SECOND PACKAGING METHOD....86
FIGURE 3.22: EACH APPLIED CURRENT ON PACKAGED LASER STACK CAUSED DECREASED RESISTANCE AND FINALLY SATURATED TO A CERTAIN VALUE 87
FIGURE 3.23: I-V CURVE FOR SECOND PACKAGING METHOD 88
FIGURE 3.24: PICTURE OF THE LASER PACKAGING FROM DR. RUI YANG'S AT JPL....89
FIGURE 3.25: SCHEMATIC OF COPPER BASE HEAT SINK SIZE....90

FIGURE 3.26: SCHEMATIC OF NICKEL WIRE SOLDERING 90
FIGURE 3.27: SCHEMATIC TO PUT SILVER PAINT ON THE EDGE OF CU HEAT SINK 90
FIGURE 3.28: SCHEMATIC OF GOLD WIRE BONDING 91
FIGURE 3.29: SCHEMATIC OF COPPER BARS 91
FIGURE 3.30: THRESHOLD EMISSION AT LOW CURRENTS FOR A QUANTUM CASCADE LASER 92
FIGURE 3.31: MULTI MODE EMISSION FROM A QUANTUM CASCADE LASER 93
FIGURE 3.32: COMPARISON FOR EPI-UP AND EPI-DOWN BONDED LASER SUBMOUNTS [53] 95
FIGURE 4.1: SCHEMATIC OF LASER BEAM ABSORPTION BY A GAS CELL 97
FIGURE 4.2: TOP VIEW OF A HUNTINGTON EV-150 PUMPING STATION 99
FIGURE 4.3: FRONT VIEW OF A LAKESHORE 330 TEMPERATURE CONTROLLER 100
FIGURE 4.4: PICTURES OF A JANIS CRYOSTAT: 101
FIGURE 4.5: PICTURE OF LASER PHOTONICS CRYOSTAT 102
FIGURE 4.6: PICTURE OF A MIR 8000 FTIR SYSTEM 104
FIGURE 4.7: CURRENT VERSUS VOLTAGE FOR JPL INTERBAND CASCADE LASER #J435 105
FIGURE 4.8: DIFFERENTIAL RESISTANCE VERSUS VOLTAGE FOR JPL INTERBAND CASCADE LASER #J435 106
FIGURE 4.9: SCHEMATIC OF ELECTRON TRANSITION IN A TWO STAGE CASCADE LASER 107
FIGURE 4.10: THRESHOLD CURRENT CHECK FOR JPL INTERBAND CASCADE LASER #J435 108
FIGURE 4.11: MULTI MODE EMISSION FOR JPL INTERBAND CASCADE LASER #J435 109
FIGURE 4.12: CURRENT TUNING PROFILE FOR JPL INTERBAND CASCADE LASER #J653 110
FIGURE 4.13: TEMPERATURE TUNING PROFILE FOR JPL INTERBAND CASCADE LASER #J653 111
FIGURE 4.14: CURRENT TUNING PROFILE (19.5 TO 23MA) FOR JPL INTERBAND CASCADE LASER #J435 112
FIGURE 4.15: CURRENT TUNING PROFILE (23.5 TO 27MA) FOR JPL INTERBAND CASCADE LASER #J435 113
FIGURE 4.16: METHANE ABSORPTION PEAKS FROM 3060CM^{-1} TO 3120CM^{-1} (FROM HITRAN) 116
FIGURE 4.17: THREE MATCHED METHANE ABSORPTION PEAKS WITH JPL ICL #J653 117
FIGURE 4.18: TWO EMISSION PEAKS OF JPL ICL #J653 LASER WITH ITS MATCHED TOLUENE ABSORPTION 119
FIGURE 5.1: STRUCTURE DESIGN OF HOLLOW WAVEGUIDES 124
FIGURE 5.2: BEAM PATHS IN A HOLLOW WAVEGUIDE AS A ABSORPTION CELL [62] 125
FIGURE 5.3: TRANSMISSION PROFILE OF THE OMNIGUIDE INFRARED WAVEGUIDE 126
FIGURE 5.4: EXPERIMENTAL SETUP OF AN OMNIGUIDE INFRARED WAVEGUIDE BASED SPECTROSCOPY 127
FIGURE 5.5: CIRCUIT DIAGRAM OF A ONE STAGE DIFFERENTIAL OPERATIONAL AMPLIFIER 129
FIGURE 5.6: A SIMPLIFIED DESIGN FOR AN OPERATIONAL AMPLIFIER 130
FIGURE 5.7: A SIMPLIFIED FEEDBACK DESIGN FOR AN OPERATIONAL AMPLIFIER 131
FIGURE 5.8: A SIMPLIFIED NEGATIVE FEEDBACK PREAMPLIFIER DESIGN 131
FIGURE 5.9: THE DESIGNED PREAMPLIFIER CIRCUIT DIAGRAM FOR MCT INFRARED DETECTORS 132
FIGURE 5.10: SIMULATED RESULTS OF THE CIRCUIT DESIGN A 20 K OHM FEEDBACK RESISTOR IN FIGURE 5.9 BY ORCAD 10.5 134
FIGURE 5.11: BEAM PROFILE OF A LASER 136
FIGURE 5.12: SCHEMATIC OF THE OPTICS SETUP TO FOCUS LASER BEAMS ONTO THE INFRARED DETECTOR 137
FIGURE 5.13: SCHEMATIC OF A TEC COOLER AND DETECTING THE LASER BEAMS 139
FIGURE 5.14: SCHEMATIC OF BEAM WIDTH MEASUREMENTS IN REGION D 139
FIGURE 5.15: MEASURED BEAM WIDTH AT POSITIONS WITH INTERVAL DISTANCES 140
FIGURE 5.16: CALCULATION OF BEAM WIDTH ON CAF_2 LENS 142
FIGURE 5.17: SCANNING DIRECTIONS OF DETECTOR FOR BEAM SHAPE MEASUREMENT 143
FIGURE 5.18: BEAM SHAPE IN X DIRECTION 144
FIGURE 5.19: BEAM SHAPE IN Z DIRECTION 145

FIGURE 5.20: POSITION TO CHECK THE FOCUSED BEAM SPOT.....147
FIGURE 5.21: BEAM SPOT ON THE FOCUSED POSITION WHICH WAS TAKEN BY A NIKON INFRARED CAMERA 148
FIGURE 5.22: THE PICTURE OF THE WHOLE SETUP WITH A CRYOSTAT WITH THE JPL ICL LASER, OPTICS, A 1 MM DIAMETER HOLLOW WAVEGUIDE AND THE MCT INFRARED DETECTOR 149
FIGURE 5 23: THE PICTURE OF THE ALIGNMENT OF THE TIP OF 1 MM DIAMETER HOLLOW WAVEGUIDE AND THE MCT INFRARED DETECTOR 150
FIGURE 5.24: (A) LASER BEAM PROFILE WITHOUT THE 1 MM WAVEGUIDE AND ALIGNING OPTICS; (B) LASER BEAM PROFILE WITH THE 1 MM WAVEGUIDE AND ALIGNING OPTICS 151
FIGURE 5.25: TRANSMITTED BEAM PROFILES AT THE THRESHOLD CONDITIONS AT DIFFERENT HEAT SINK TEMPERATURES.....152
FIGURE 5.26: TRANSMITTED LASER BEAM PROFILES AT DIFFERENT INJECTION CURRENTS 153
FIGURE 5.27: A SETUP WITH A BALL LENS TO FOCUS BEAMS INTO THE HOLLOW WAVEGUIDE.....154
FIGURE 5.28: SCHEMATIC OF ANGLE Θ AT THE FOCUSING POINT.....155
FIGURE 5.29: THE WHOLE SETUP OF THE HOLLOW WAVEGUIDE BASED SYSTEM FOR GAS SENSING 157

ABSTRACT

Mid-infrared emitters (3 – 30 μm spectral region) have numerous applications in spectroscopy and communications. Two major types of semiconductor material systems offer great potential for the fabrication of mid-infrared emitters with continuous wave (cw) operation at room temperature: IV-VI materials (lead salts) and III-V quantum cascade laser materials. Compared with quantum cascade lasers, IV-VI double heterostructure lasers are easier to fabricate, are widely tunable, and operate at lower voltages.

To characterize the optical emission of the mid-infrared emitters, a filter wheel based mid-infrared spectrometer was developed to detect mid-infrared radiation between 1875 cm^{-1} and 3627 cm^{-1}. Photoluminescence (PL) tests of a molecular beam epitaxy (MBE) grown IV-VI quantum well sample (MBE# W336) were performed using the filter wheel based mid-infrared spectrometer. By comparing the PL emission intensity to blackbody emission spectra, the cw PL emission power from the IV-VI quantum well sample at room temperature was estimated to be 0.183 mW when illuminated with a near-IR (911 nm) pump laser having a power of 970 mW.

As part of an effort to improve heat dissipation from mid-infrared laser materials during operation, work was performed on mounting laser bars in an epi-side-down configuration. Results obtained from packaging interband cascade laser (ICL) bars provided by the Jet Propulsion Laboratory (JPL) were partially successful. Epi-side down packaged devices exhibited current-versus-voltage characteristics similar to epi-side up packaged devices, but mid-infrared emission was not observed when mounted devices were tested using a Fourier transform infrared (FTIR) spectrometer.

Mid-infrared emission spectra for epi-side up packaged JPL ICLs measured using FTIR spectroscopy are presented and analyzed. Injection current tuning for ICL #J653 at 86 K was observed to be 0.10 cm^{-1}/ mA, while the tuning rate for ICL #J435 at 80 K was 1.2 cm^{-1}/ mA. This difference may be caused by different sized mesa stripes. ICL #J653 has a mesa width of 15 μm and a cavity length of 1.5 mm, while ICL #J435 has a mesa width of 150 μm and a cavity length of 1 mm. A smaller current tuning rate is consistent with less active region heating, and ICL #J653 with its thinner mesa width will have more effective active region heat dissipation due to better lateral heat flow normal to the laser cavity. By contrast, ICL #J435 with its much larger mesa area will experience more heating with increasing current thus giving a larger current tuning rate.

Further work was performed to evaluate the utility of hollow-core waveguides to manipulate mid-infrared radiation. Emission from a JPL ICL laser beam was focused and aligned into a 1 mm diameter hollow waveguide from Polymicro Technologies and measured with an FTIR spectrometer after traveling a distance of 1 meter through the waveguide. By comparison, it can be seen that there are no obvious difference for the laser beam profile with or without a hollow waveguide. When the laser was operated at 29 mA injection current and 82 K heat sink temperature, the mode intensity was reduced by 80% compared with emission without the waveguide. Improvement in fiber-coupling optical alignment by using an infrared transparent ball lens is also analyzed theoretically. The optimal distance between the ball lens and a 0.22 mm inner diameter hollow waveguide was determined to be 0.228 mm when placed at the focal point of a 4 inch focal length CaF_2 lens.

Chapter 1

Fabrication, packaging and application of mid-infrared emitter technology

1.1 Introduction

Mid-infrared emitters (3 – 30 μm spectral region) have numerous applications in spectroscopy and communications, such as trace gas detection, ultra-low-loss fiber communication, chemical process monitoring, and molecular spectroscopy. Mid-infrared emitters are more useful than near infrared emitters for chemical sensing applications since strong fundamental absorption bands reside in the mid-infrared spectral region.

To date, two semiconductor material systems offer the potential for fabrication of mid-infrared emitters: IV-VI materials (Lead salts) and III-V quantum cascade laser materials. Different packaging techniques are developed on mid-infrared emitters, which include lead free soldering, optoelectronic adhesives and distributed feedback design in quantum cascade lasers. Both IV-VI lasers and III-V quantum cascade lasers are good candidate sources for applications to trace gas sensing. By applying IV-VI lasers or III-V quantum cascade lasers, parts per billion (ppb) and sub-ppb detection limits could be achieved.

1.2 Objectives for this project

To estimate emission power, new ways are developed to measure mid-infrared emitters. Since thermal management is one of the most important factors for achieving room temperature operation of mid-infrared emitters, this project investigates new device packaging methods (epi-side down) to improve active region heat dissipation. To find possible applications for molecular spectroscopy, the emission properties of novel interband cascade lasers (ICLs) are measured and analyzed. Finally, the project explores methods for coupling mid-infrared emission into waveguides, which can facilitate multiplexing of two or more lasers, make optical alignment easier, and can lead to the development of a more compact gas cell technology. Work in these areas will help to advance the state-of-the-art for mid-infrared emitter technology.

1.3 IV-VI materials system

As early as 1950's, lead-sulphide (PbS) detectors were made to study infrared radiation in 1-4 μm range by astronomers [1]. After that, most commercial infrared detectors were made from PbS, and IV-VI diode lasers were reported in the 1960's too [2]. Infrared detectors and diode lasers, which were made from IV-VI binaries PbS, PbTe and PbSe, and their alloys with SnSe and SnTe are able to cover a large wavelength range (3 – 30 μm).

Methods to grow IV-VI semiconductors for optoelectronic devices fabrication include chemical or vapour deposition or liquid phase epitaxy and molecular beam epitaxy (MBE).

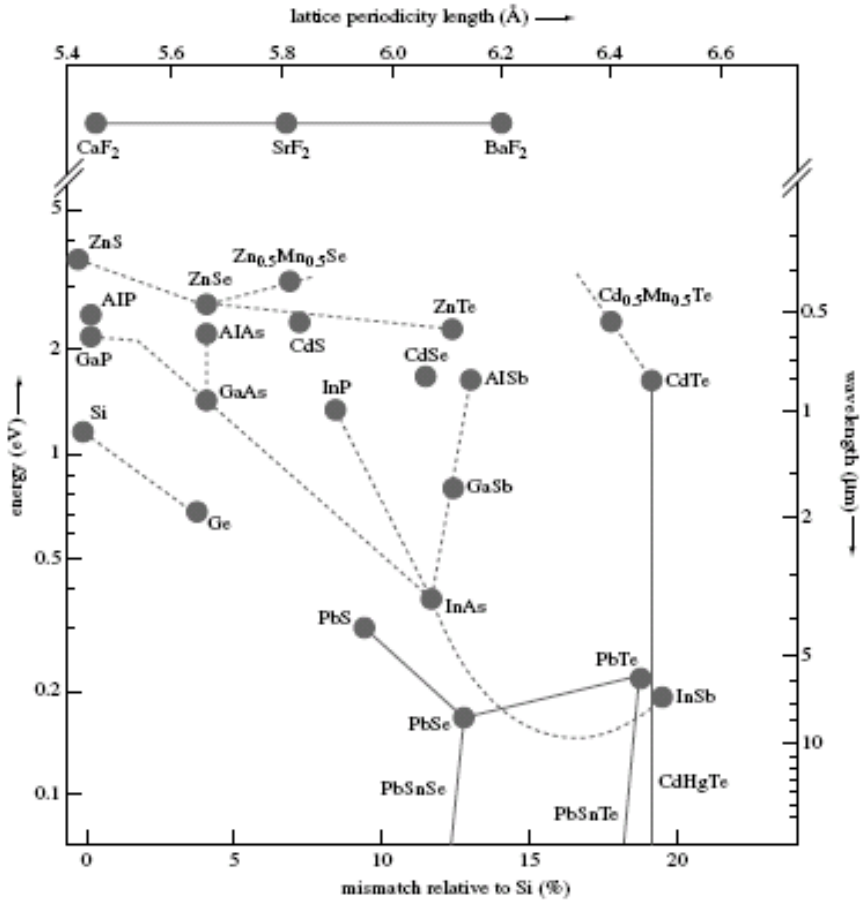


Figure 1.1: The bandgap energy versus lattice periodicity length of some semiconductor compounds [3].

MBE is a special evaporation technique, where usually the lead-salt part is evaporated from PbSe, Se, SnSe, etc.. In Figure 1.1, PbS, PbSe and PbTe cover a large lattice constant interval from below 6 to above 6.4 Å, and have almost the same bandgap energy. After 20 years application, MBE has proven to be very well suited for the growth of lead-salt heterostructures as well as III-V quantum structures.

Similar to GaAs semiconductor lasers, lead-salt diode lasers consists of a crystal of a lead-salt semiconductor ($Pb_{1-x}Sn_xSe$ or $Pb_{1-x}Sr_xSe$). A p–n junction is formed by

epitaxial growth. The front and rear are both cleaved and forms the facets for the laser cavity. IV-VI material systems differ from III-V material systems in their band structure.

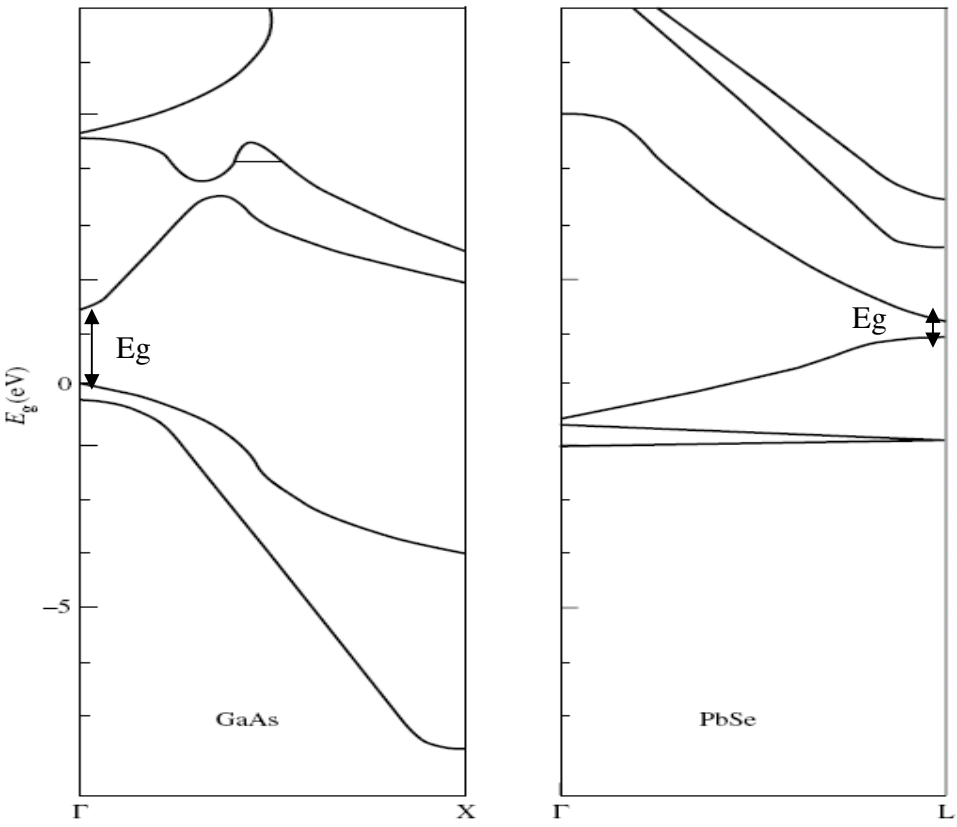


Figure 1.2: The band structure of GaAs and PbSe [4]

For example, GaAs and PbSe band structures are shown in Figure 1.2. The direct bandgap minimum of lead salts is not located at the Γ-point, or in the centre of the Brillouin zone. Instead, there are four minima located at the L-points, or on the (111)-axes and on the Brillouin-zone surface. Electrons and holes also have similar masses due to the similar conduction and valence band dispersion relations. Due to lack of valence band degeneracy, IV-VI optoelectronic devices will have much less Auger recombination than III-V devices.

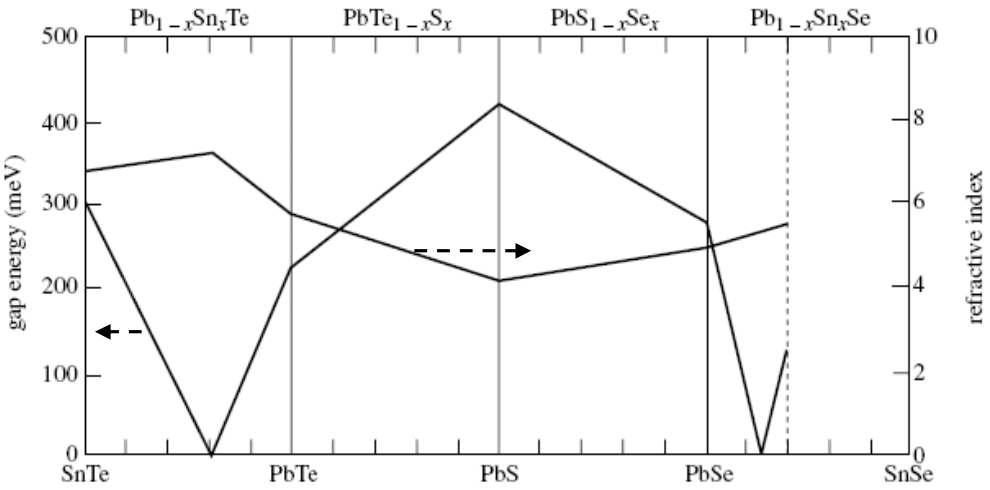


Figure 1.3: The refractive index of lead-salt materials [5]

From Figure 1.3, it is shown that an increase in bandgap energy is associated with a decrease in refractive constant. IV-VI materials have relatively large dielectric constants, increases carrier mobility, and results in longer recombination lifetimes.

However, IV-VI materials have some disadvantages in its applications. The major disadvantage is low operating temperature. Cryogenic coolers or liquid nitrogen cryostats are required for IV-VI lasers operation. Cryogenic coolers are expensive, and liquid nitrogen cryostats are expensive and bulky. Mechanical stress may be caused by the different thermal expansion coefficients of the laser and packaging material during the cycling of cooling and heating, and it can cause microscopic changes in the interface between chip and heat sink, which will decrease cooling efficiency and affect the laser emission parameters [6].

1.4 History of lead salt lasers

In 1964, laser emission at much longer wavelengths was reported from PbTe and PbSe p-n junction diodes by J.F. Butler et al. [7]. During past years, new methods of fabrication, such as liquid phase epitaxy (LPE), hot wall epitaxy (HWE), and molecular beam epitaxy (MBE), were developed. Significant improvement in IV-VI laser was accomplished based on these techniques. To date, molecular beam epitaxy (MBE) has become more popular than other techniques for IV-VI laser fabrications.

Due to advances in MBE techniques, much progress in IV-VI laser development has been achieved in recent years [7]. High temperature operation was achieved in the 3-5 μm wavelength region based on PbSe/PbSrSe IV-VI laser diodes. Lead salt lasers achieved above room temperature (85^{o}C) operated in pulsed mode in 1999 [8]. High operating temperature (223K) in continuous wave mode (CW) operation was reported in 1996 [9].

1.5 Quantum cascade lasers

Another choice for mid-infrared emitters is III-V quantum cascade structure lasers. Quantum cascade (QC) lasers are a new type of semiconductor laser based on electronic transitions between quantized band states of a multiple quantum well structure [10]. They have been developed through bandgap engineering and grown by molecular beam epitaxy(MBE) [11]. To date, quantum cascade lasers are mainly divided into three types: intraband cascade laser, interband cascade laser and interband cascade laser with “W” structure.

For an intraband cascade structure, multiple photons are generated when injected electrons transit at steps of a quantum well structure. Intersubband transitions can suppress the possible phonon non-radiative relaxation path, and result in lower laser threshold current [12]. Figure 1.4 shows how electrons transit between conduction subband bands for intraband transitions.

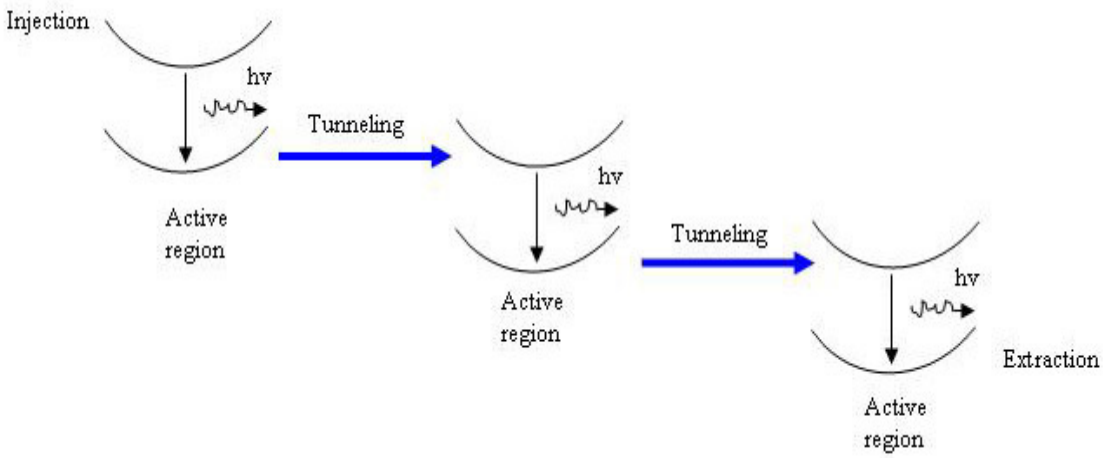


Figure 1.4: Schematic of intraband transitions

Theoretical calculations show type-II interband lasers have the feasibility to operate in continuous wave mode up to room temperature [12].

In Figure 1.5, it is shown that electrons transit between conduction subbands and valence subbands for interband transitions.

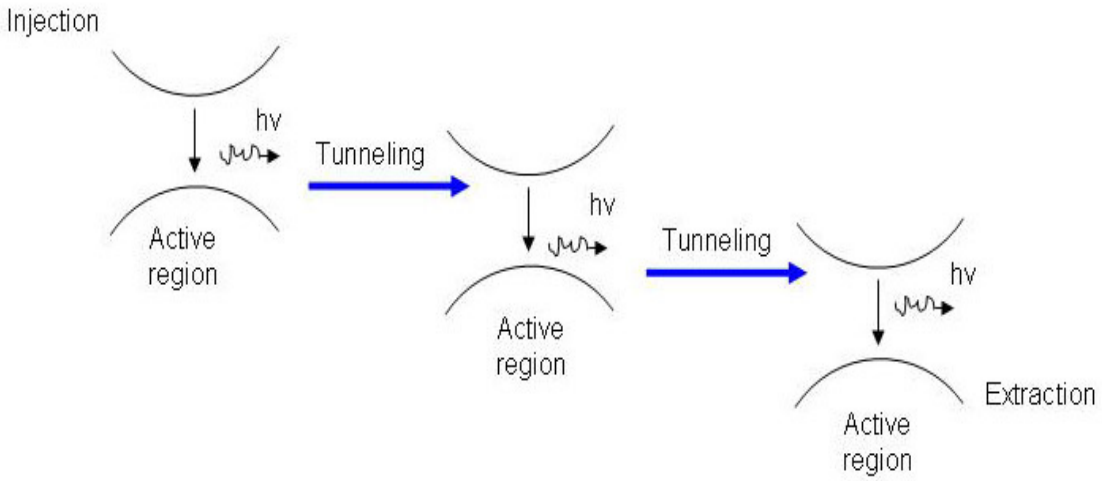


Figure 1.5: Schematic of interband transitions

Interband transitions require a type II band alignment. Figure 1.6 shows a typical band alignment in a type II interband quantum cascade laser. Due to much longer relaxation time from E_e to E_h compared with the carrier transportation time, a population inversion is easily achieved. Electrons at state E_h will tunnel through the thin AlSb barriers and GaSb wells, and scattered into the conduction band of the next injection region. Because of a strong spatial interband coupling, electrons are ready to be injected into the next active region [13].

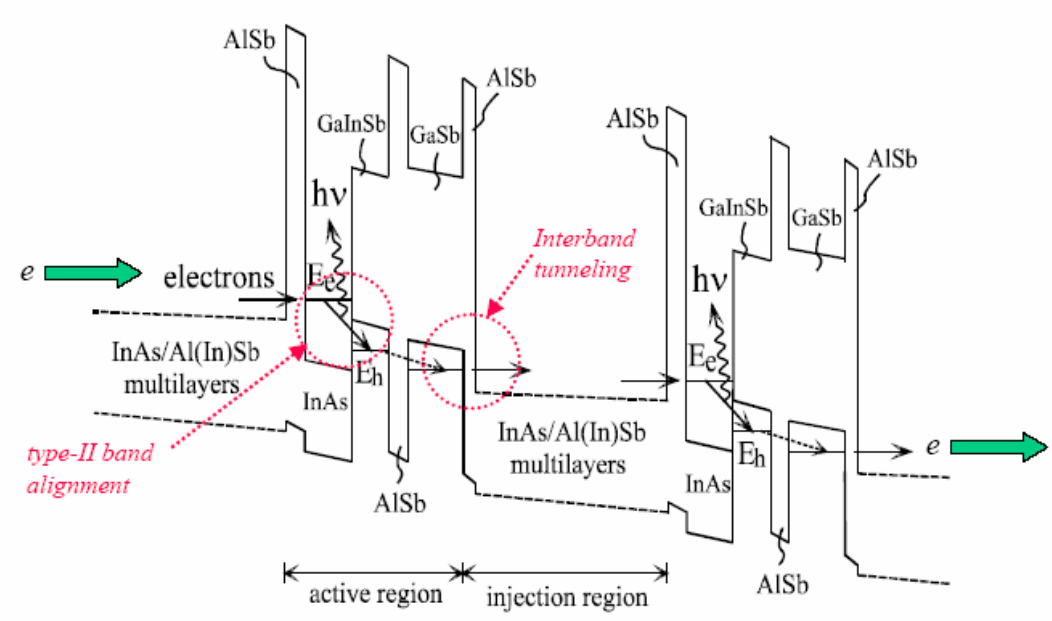


Figure 1.6: Schematic of n-type quantum cascade laser based on interband quantum wells [13]

The interband cascade laser with "W" structure is an improved quantum structure based on interband cascade structure. It uses two-sided quantum well confinements for a active region in the laser, instead of one side quantum well confinement in type II interband cascade laser structure [14]. This kind of design offers even better Auger suppression, excellent electrical confinement, strong wavefunction overlay and two dimensional density of states for both electrons and holes.

1.6 History of quantum cascade laser development

The idea of fabricating an infrared emitter based on intersubband transitions within semiconductor quantum well was first proposed by Russian scientists Kazarinov and Suris

in 1971 [15]. Due to limited growth technology and limited understanding of nonradiative relaxation mechanisms at that time, no device was demonstrated for twenty years. With developments of molecular beam epitaxy growth technology after 1980s, the first electrically pumped intersubband or intraband laser was demonstrated at 4.2μm wavelength in 1994 by Faist et al.[16]. A year later, the lasers were fabricated to operate in CW mode at cryogenic temperatures, and in pulsed mode up to room temperature [17,18,19]. Distributed feedback (DFB) lasers were first introduced in 1996, providing continuously tunable single-mode laser output [20]. Parallel to that, the quest for higher power and longer-wavelength devices led to the invention of the superlattice active region in 1997 [21]. In 1998, QC-DFB lasers were demonstrated for the first time in trace-gas sensing applications [22]. Based on his model in early 1994, Rui Yang fabricated the first room temperature quantum superlattice (type II) interband quantum cascade lasers with a emission wavelength of 3.3-3.5 μm in 2002 [23].

1.7 Comparison of IV-VI double heterostructure laser and quantum cascade laser

Compared with quantum cascade lasers, IV-VI double heterostructure lasers are easier to fabricate, are widely tunable, and operate with lower voltages. A comparison of fabrication technology and tunability is provided below.

- **Fabrication technology:**

Quantum cascade lasers are composed with thousands to ten of thousands of quantum well layers with exact calculated quantum layer thickness. So the fabrication process requires precise control of epitaxy layer thickness, and needs several hours for epitaxial layer growth.

By comparison, IV-VI lasers can consist of just a few dozen (at most) layers. The process thus requires less time, so the cost will be less and the yield can be much higher than that of quantum cascade lasers.

- **Tunability:**

IV-VI lasers can achieve 200 cm^{-1} wavelength tunable range over a 30 degree temperature range, and the highest tunability for type II quantum cascade lasers will have around 10 cm^{-1} temperature tunability over a 10 degree temperature range, see Figure 1.7.

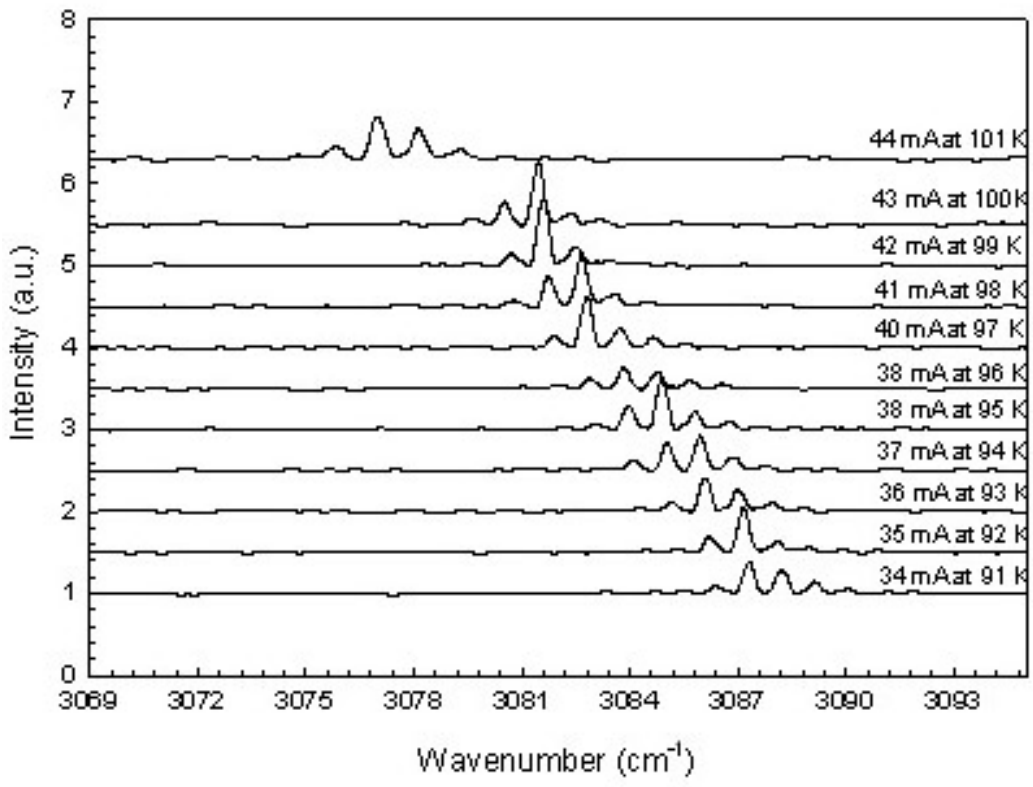


Figure 1.7: Temperature tuning profile (91-101K) of an interband quantum cascade laser (JPL ICL #J653) in 2002

For some types of quantum cascade lasers, current tuning capability is much less than temperature tuning capability. For example, current tuning of the JPL ICL #J653 quantum cascade laser is ~ 0.05 cm^{-1} /mA, compared with 1.0 cm^{-1}/ K temperature tuning for the same laser. So the major tuning choice for JPL ICL #J653 quantum cascade laser will be the temperature tuning technique. In Figure 1.7, the temperature tunable rate for JPL ICL #J653 is around 1.0 cm^{-1}/ K, and laser operating temperature is from 91 K to 107 K.

Figure 1.8 shows current tuning (from 10 to 70 mA) spectra from a PbTe-PbEuTeSe mesa structure laser. From characteristics, the temperature tunable rate of the PbTe-PbEuTeSe laser is around 0.33 cm^{-1}/ mA, and the laser operating temperature is at 30 K.

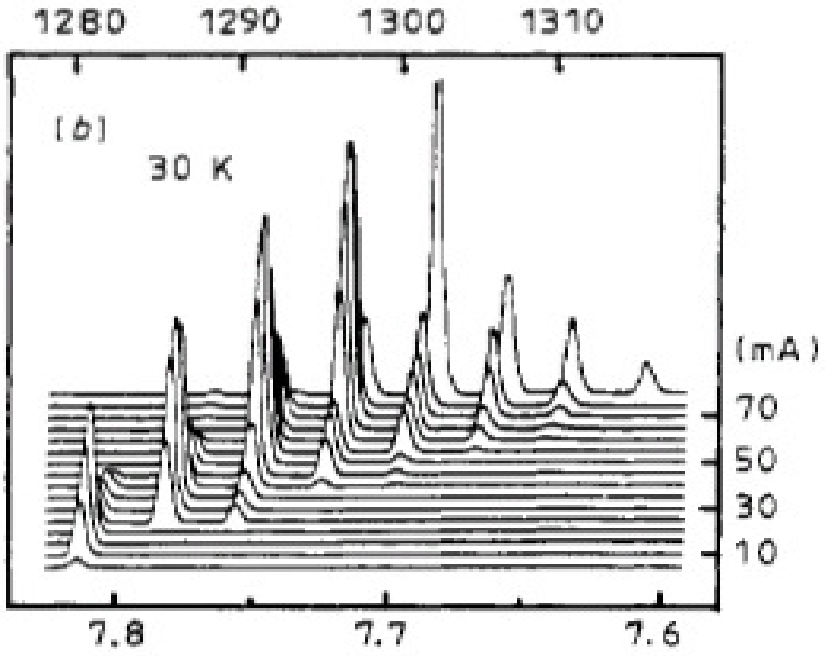


Figure 1.8: Current tuning profile of PbTe-PbEuTeSe mesa structure laser in 1989 [24]

From the above data, the PbTe-PbEuTeSe laser has a higher capability of current tuning than the JPL ICL #J653 quantum cascade laser does. Due to the limited current tuning capability, the JPL ICL #J653 quantum cascade laser mainly uses operating temperature as a tuning choice. In contrast, IV-VI lasers can use the operating current as a tuning choice. In addition, much lower voltages indicate that IV-VI lasers can be more reliable than the quantum cascade lasers, since much less heat is deposited into the device.

1.8 Laser packaging techniques

Future packaging trends for optoelectronic devices will be focused on miniaturization, increased integration, designing for automated assembly and testing under standards. Existing packaging techniques include: lead free soldering, laser welding and optoelectronic adhesives.

1.8.1 Lead free soldering

Au-Sn-based, Cu-Sn-based, Ag-Sn-based and Ni-Sn-based solders are desirable lead free choices in optoelectronic device packaging. A group in Greece [25] studied optimized composition percent for Sn in An-Su bonding. In the experiments, three different compositions were tested: 80% Au / 20% Sn, 61% Au / 39% Sn and 29% Au / 71% Sn.

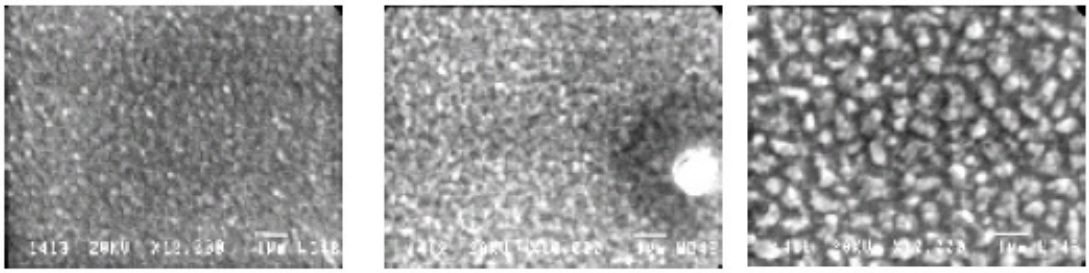


Figure 1.9: a. SEM of Au-20Sn surface b. SEM of Au-39Sn surface c. SEM of Au-71Sn surface [25]

Figure 1.9 shows that the surface roughness increases with Sn content. And surface condition with 71% Sn is relatively rough. The SEM results indicate the surface profile is poor when Sn metallic composition is 71% [26].

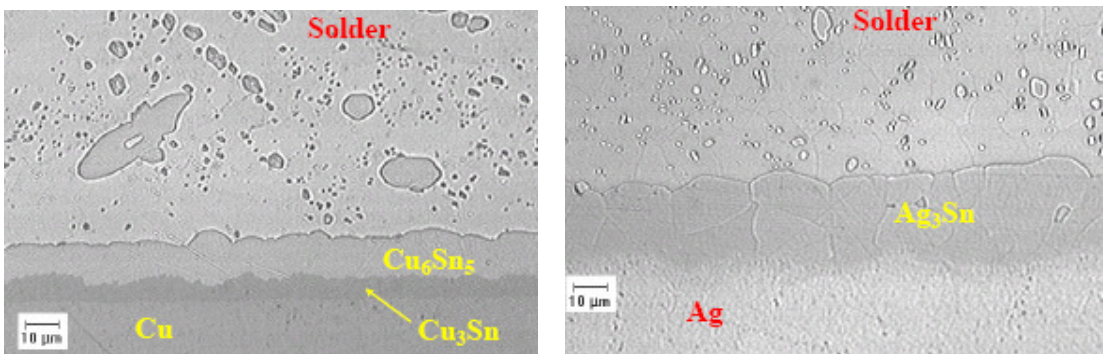


Figure 1.10: a. SEM picture of Cu-Sn b. SEM picture of Ag-Sn bonding [26]

Richard R. Chromik, et al. [26] investigated the phase structure, microstructure development and hardness of Cu-Sn-based and Ag-Sn-based solders. These studies mainly concentrate on the kinetics and mechanical behavior for interfacial reactions. Results in Figure 1.10 show both lead free solders can achieve a uniform bonding layer.

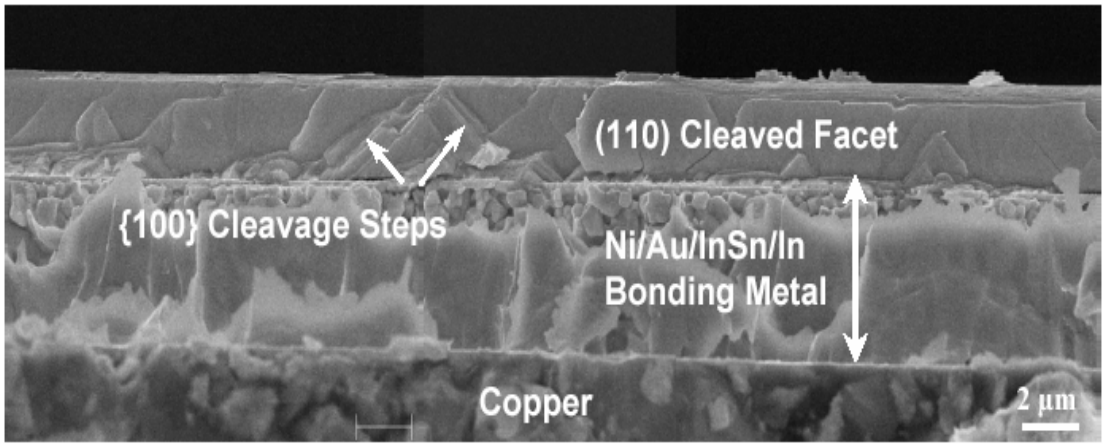


Figure 1.11: Scanning electron microscopic cross-sectional view of a cleaved film of PbSe MQW attached onto a separated copper bar using Ni/Au/In-Sn/In/In-Sn/Au/Ni bonding metallurgy [27]

Figure 1.11 is an SEM micrograph showing a (110) cleaved facet of the IV-VI semiconductor epilayer structure bonded to copper using Ni/Au/In-Sn/In/In-Sn/Au/Ni bonding metallurgy. The observed bonding medium thickness is about 5 µm, and the total thickness of the deposited metals is 5.7 µm. the bonding layer is also very uniform over hundreds of microns of the cleaved sample surface. This section shows good void-free bonding between the IV-VI epilayer and the copper heat sink [27].

In a summary, Au-Sn-based, Cu-Sn-based, Ag-Sn-based and Ni-Sn-based bondings are desirable lead free choices in optoelectronic device packaging. Desirable results of the formed bonding layer obtained indicate their future applications in optoelectronic device packaging for both IV-VI and III-V quantum cascade laser materials.

1.8.2 Optoelectronic adhesives study

Characterization metrologies of the optoelectronic adhesives for laser packaging were studied recently. Figure 1.12 is a testing model for optoelectronic adhesives study [28].

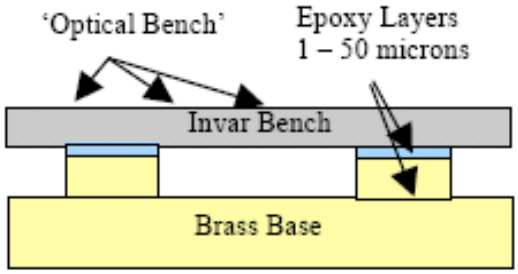


Figure 1.12: Schematic diagram of a dimensional stability test vehicle with high CTE mismatches [28]

Based on various viscoelastic characterizations of selected optoelectronic adhesives, the constitutive equations were developed to be fed into finite element models. Three different optoelectronics adhesives were tested: epoxy based Adhesive A (Epo-Tek 353 ND), and acrylic-based Adhesives B and C.

Testing results indicate that the viscoelastic behavior of optoelectronic adhesives can be modeled using a stretched exponential, and the dimensional stability of adhesives can be calculated based on the strength of the relaxation phenomena and their respective time constants.

1.8.3 Distributed Feedback (DBF) design in quantum cascade lasers

For gas sensing spectroscopy, lasers have to operate with the stable single-mode emission and controlled tunability. Researchers are trying to develop distributed feedback quantum cascade lasers (QC-DBF). Figure 1.13 shows one design of a distributed feedback quantum cascade laser [29].

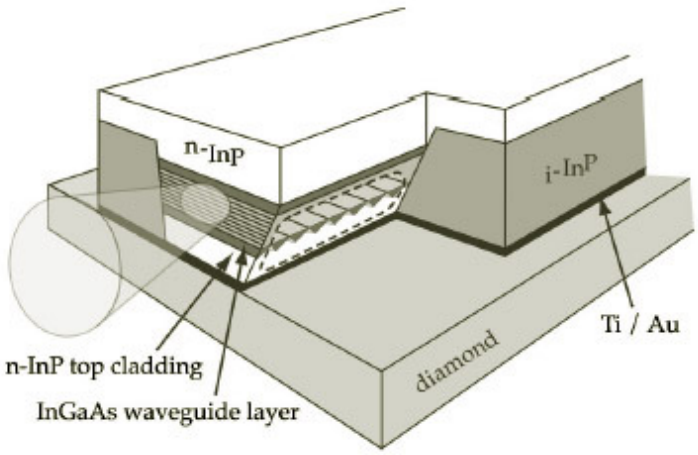


Figure 1.13: A design of distributed feedback in quantum cascade laser [30]

The laser in Figure 1.13 is a first order DFB QC laser with continuous wave operation on a thermoelectric cooler at an emission wavelength of 1115 cm^{-1}.

In Figure 1.13, a junction-down mounted QC laser with the DFB grating etched into the upper InGaAs layer on top of the active laser core before regrowth of the InP top cladding. The DFB grating with a period of 1.43 μm was defined and etched in the InGaAs waveguide

Single-frequency emission with a side mode suppression ratio of >27 dB and with a tuning range of 5 cm^{-1} between 200 and 245 K is obtained for this distributed feedback structure quantum cascade laser. And the tunability of this DFB laser is around 0.08 cm^{-1} / K.

1.9 Laser applications in gas detection

Both III-V quantum cascade lasers and IV-VI lasers represent good candidate sources for applications to trace gas sensing. Recently, the high tuning capability of those developed lasers considerably improved the sensitivity, selectivity, and response time of optical trace-gas sensors. In potential commercial applications, the reduced size and low cost of the IV-VI diode lasers make them particularly competitive with respect to the III-V quantum cascade lasers, especially if reliable continuous wave operation can be achieved

For the IV-VI diode laser, achieving single mode emission with mW output powers at room temperature represented a major objective for the development of commercially viable gas sensors. The emission wavelength of quantum cascade lasers can cover the 3–25 um range, which virtually is the whole MIR spectrum. By applying quantum cascade lasers in gas detection, parts per billion (ppb) and sub-ppb detection limits could be achieved, even though exotic spectroscopic solutions such as multipass cells will be required.

1.9.1 Nitric oxide detection by an IV-VI diode laser

Nitroic oxide detection was performed by a tunable-diode laser absorption spectrometer (TLAS) in the Solid State laboratories at the University of Oklahoma in 2002.

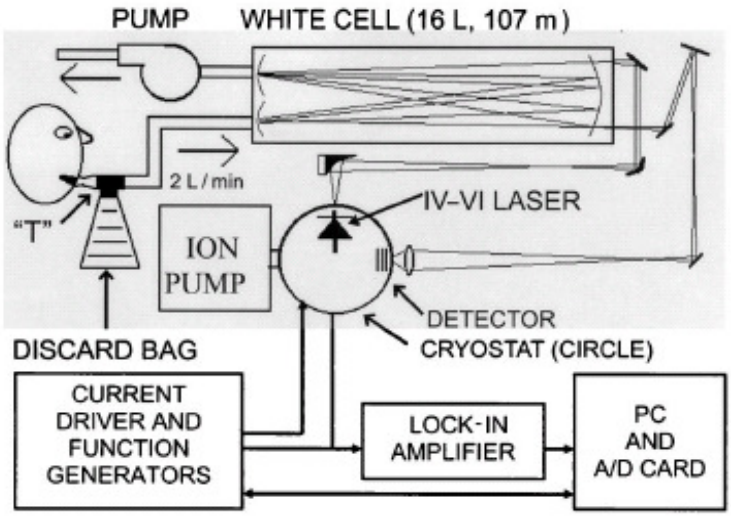


Figure 1.14: Schematic of the breath-collection apparatus and the TLAS system equipped with a IV–VI mid-IR laser [31]

The experimental setup for the TLAS system design is shown in Figure 1.14. The laser source in this TLAS is a single IV–VI laser with typical optical output power of 300 μW. A closed cycle cryogenic refrigerator was used to cool the laser, which provides a liquid nitrogen free system. An integrated heater and temperature controller maintained stable laser operating temperatures at 102 K with an accuracy of 0.01 K. The beam traversed a 100 meter cell before being focused onto an HgCdTe mid-IR photovoltaic detector inside the cryostat.

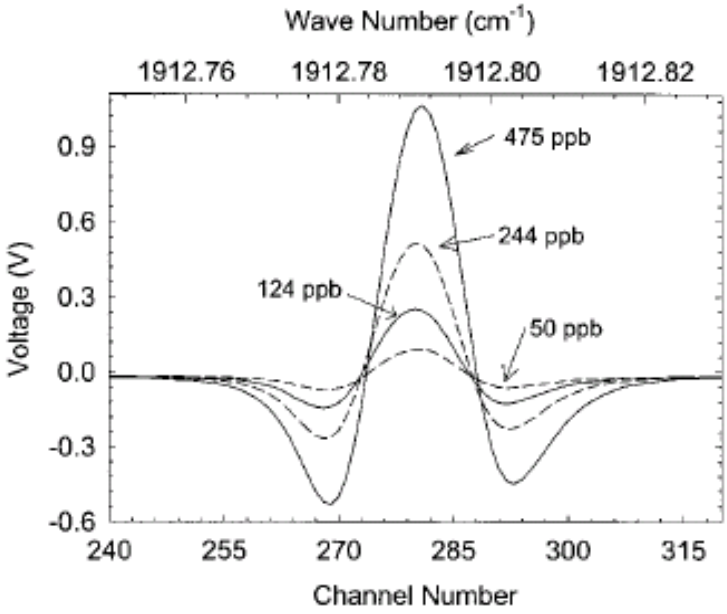


Figure 1.15: Measured second-harmonic absorption features of NO (1912.79 cm^{-1}) for concentrations of 50, 124, 244, and 475 ppb [31]

Figure 1.15 shows second harmonic absorption spectra for NO concentrations ranging from 50 ppb to 475 ppb. The measured minimum NO detection limit was 1.5 ppb based on a four second integration time period. Further improvement in the lower detection limits will be possible when faster electronics are able to collect more spectra in a given time. Moreover, nitric oxide research indicated that a gas sensor based on IV-VI laser can be developed to measure exhaled NO for managing therapy [31].

1.9.2 C_2H_4 and CH_3CH_2OH detection by quantum cascade lasers

Organic molecule detection can be performed with quantum cascade lasers. Based on a wavelength emission of 10 μm by a quantum cascade laser, ethylene (C_2H_4)

concentrations can be determined by a rotational component in the fundamental absorption band.

An ethylene gas sensor was developed by a group at Rice University. The minimum C_2H_4 detection sensitivity of the sensor was in the low ppb range. The ethylene sensor can been used to monitor C_2H_4 in vehicle exhaust and in air collected in a high-traffic urban tunnel.

In 2002, another research group in Switzerland developed a new organic gas detection system with quantum cascade lasers, which used an adapted photoacoustic sensor based on Helmholtz resonance [32]. By plotting "signal to noise" vs ethanol vapors concentration in Figure 1.16, linear extrapolation leads to ~1 ppm minimum detectable concentration.

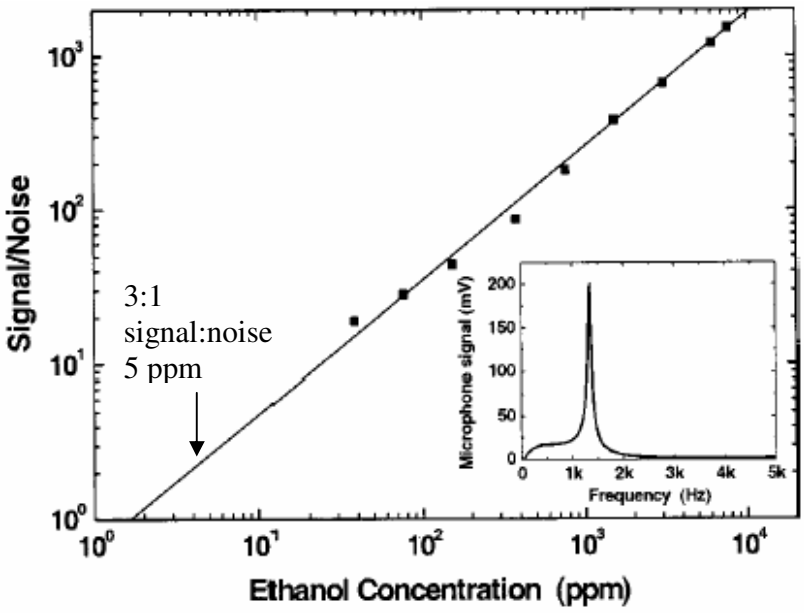


Figure 1.16: Signal to noise vs ethanol vapors concentration in ppm [32]

In summary, mid-infrared laser choices for trace gas sensing includes III-V quantum cascade lasers and IV-VI diode lasers. Recently, quantum cascade lasers can be operated either in CW mode at cryogenic temperatures or in pulse mode with operating temperatures from -40 °C to above room temperature. In contrast, IV-VI lasers can only work at cryogenic temperatures to date. Improvements in the operating temperatures of quantum cascade lasers eliminate the need for liquid-N_2 cooling or cryogenic cooling. However, the better yield, lower voltage and fabrication cost of IV-VI diode lasers make them particularly competitive with respect to III-V quantum cascade lasers in potential commercial use. Currently, both III-V quantum cascade lasers and IV-VI lasers are the leading approaches being pursued to meet needs in ultrahigh-sensitivity chemical detection.

1.10 Dissertation organization

This dissertation presents the study of Mid-IR emitter technology. It includes the investigation of photoluminescence power estimation of IV-VI quantum well materials using a filter wheel based testing system, investigating laser packaging techniques (epi-side down and epi-side up techniques), and gas detection using type II interband quantum cascade lasers.

Chapter One gives a detailed overview of IV-VI lasers and quantum cascade lasers and recent developments. Chapter Two describes the photoluminescence power estimation of IV-VI quantum well materials by a filter wheel based system. Chapter Three presents

laser packaging techniques based on type II quantum cascade lasers, including epi-side down and epi-side up techniques. FTIR testing results of temperature and current tuning on quantum cascade lasers are summarized in Chapter Four and possible gas detection applications using type II quantum cascade lasers are discussed. Chapter Five details strengths of waveguide based sensor system, study of emission modes tuning by a hollow waveguide, and its potential in gas detection. Chapter Six provides a summary and suggestions for future research.

Results from this work show that it should be possible to make significant improvements in mid-infrared emitter technology by improving active region heat dissipation, controlling mode structure of emission, and coupling of emission to hollow waveguides.

Chapter 2

Filter wheel based mid-infrared spectrometer

2.1 Introduction

A filter wheel based mid-infrared spectrometer generates mid-infrared spectra by combining a circularly variable filter wheel with an accurate voltage measuring device like lock-in amplifier to obtain a signal from an infrared detector.

In the spectrometer, a circular variable filter wheel, one of the most important components, has a characteristic of passing only a band of light in a specific spectral region. By rotating the filter wheel, a certain wavelength range of the incident infrared emission can be selected.

The incident mid-infrared emission is modulated by a pulse mode current source or chopped by a mechanic chopper, filtered by the circular variable filter wheel, and focused on to a detecting window of an infrared detector with CaF_2 and ZnSe lenses. The lock-in amplifier will acquire the signal from the infrared detector, which helps to significantly reduce the detector signal noise. An infrared spectrum is generated in the computer by a Labview program which extracts signals from the lock-in amplifier by an ISA GPIB card.

This technique is an alternative way to measure photoluminescence and laser emission of optoelectronic devices.

I. Advantages of this system

- A better sensitivity than the standard FTIR spectrometer because the lock-in amplifier in the spectrometer can reduce the impact of detector noise
- Simple and easy to align
- Capability to measure time-resolved light emission and thus extract excited state electron lifetimes

II. Disadvantages of this system

- Time consuming compared with FTIR measurement. Each measurement will take about 3-5 minutes in optical wheel based system
- Detector limitation: Due to 3 -5 μm detectivity, the measuring range is relatively narrow compared with Fourier Transform Infrared spectrometer (FTIR)

With this filter wheel based mid-infrared spectrometer, infrared blackbody emission power and photoluminescence power of IV-VI quantum well structure materials in the infrared region were estimated. External quantum efficiency can be also calculated based on estimated power data and experimental input power. Furthermore, this system should allow measurement of photon lifetime.

2.2 Components of the filter wheel mid-infrared spectrometer

The main parts of the filter wheel mid-infrared spectrometer are shown in Figure 2.1. Newport brand optical mechanical parts (posts, optical tables, rails, and so on) were used for the system setup and alignment.

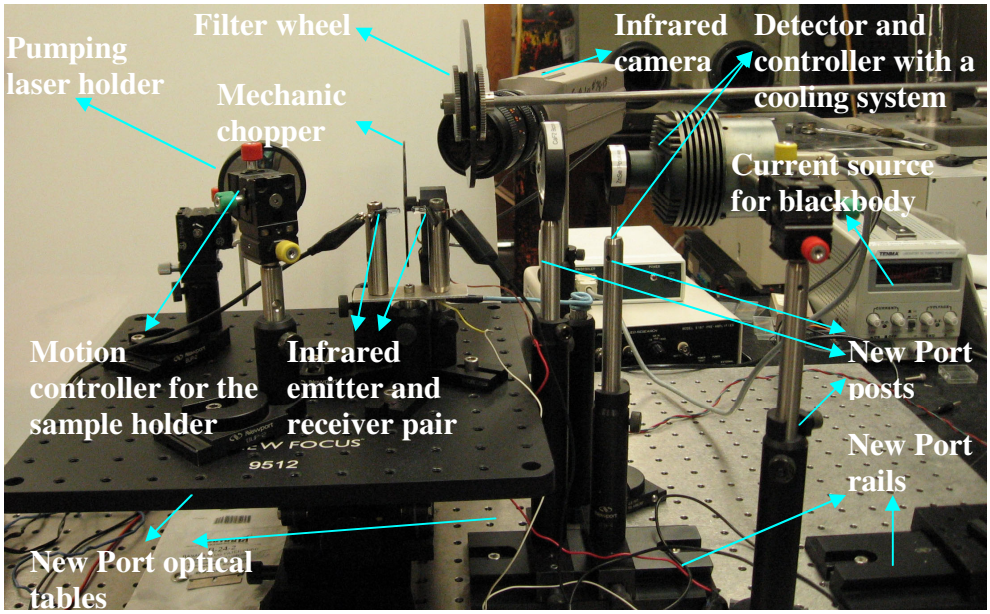


Figure 2.1: Picture of filter wheel based mid-infrared Spectrometer

The primary components for a filter wheel mid-infrared spectrometer are:

1. Optical lens (Bi-convex CaF_2 lens and Positive ZnSe meniscus): Focusing infrared light onto the infrared detector.
2. Circular Variable Filter (CVF) wheel for selecting a specific wavelength
3. Stand for the circular variable filter wheel to hold and align the circular variable filter wheel
4. Sample holder for holding samples and controlling sample temperature
5. Fiber-coupled laser at λ=911 nm and the current source for optically pumping emission of IV-VI quantum well samples
6. Infrared detector for detecting photoluminescence
7. Lock-in amplifier for amplifying the detector signal. It reduces noise by many-fold and increases system sensitivity

8. GPIB card and Labview program for acquiring signals and displaying results
9. Infrared blackbody IR-12 used for the system aligning and calibrating

Details of each main component will be provided as next.

2.2.1 Optical lens

Bi-convex CaF_2 lens: A lens is a transparent medium which has two surfaces that are designed to either converge or diverge light. Bi-convex lenses, which are used for focusing and image magnification, are the simplest converging lenses. They have convex surfaces on both the ends. Due to the symmetric nature of this lens, the spherical aberrations are reduced [33].

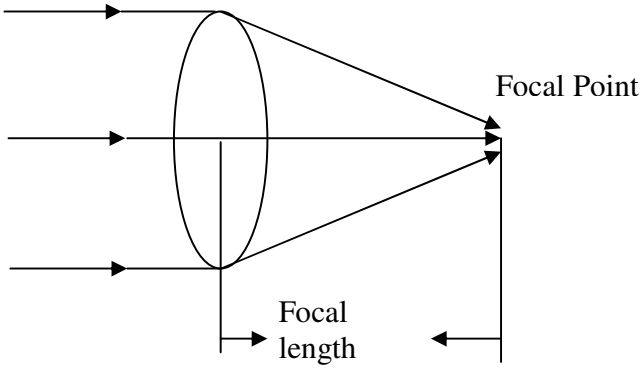


Figure 2.2: Schematic of bi-convex lens

Figure 2.2 shows the focusing properties of a bi-convex lens which is dependent on the nature of the used material and angle of curvature of the faces.

A CaF_2 bi-convex lens was chosen for this experiment due to its inexpensive price, good convergance and 90% transmittance for mid-infrared radiation. Figure 2.3 below

shows the transmittance of CaF_2. The diameter of this CaF_2 lens is 2 inches and the focal length is 2 inches.

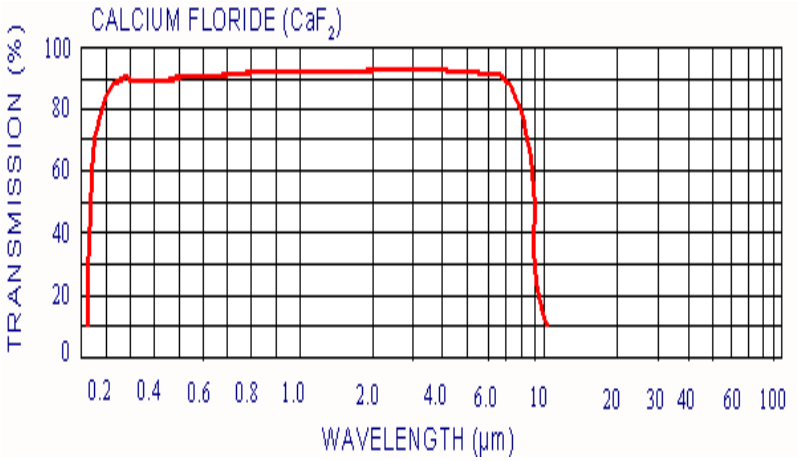


Figure 2.3: Transmittance of the CaF_2 Bi-convex lens [34].

Positive ZnSe meniscus: These lenses are also called as concavo-convex lens. This type of lens is very good for infrared light focusing. One of the faces is concave while other is convex hemispherical shape (Figure 2.4) [34].

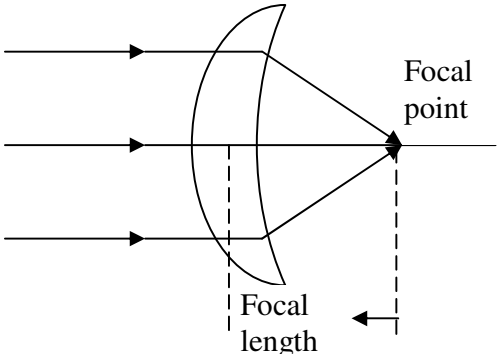


Figure 2.4: Schematic of Concavo-convex lens showing the focal length

Though Zinc Selenide concavo-convex lens has just 65% infrared transmittance (Figure 2.5), this lens is chosen due to its property which can focus the light to a very small

area with a short focal length. This lens also can be used in conjunction with another converging lens to change the focal length of the combination [34]. Both the diameter and the focal length are 1 inch for the ZnSe lens.

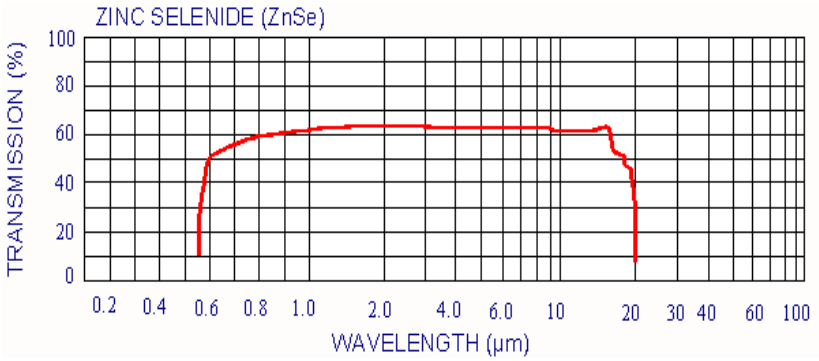


Figure 2.5: Transmittance of Zinc Selenide lens [34]

2.2.2 Circular variable filter (CVF) wheel

The critical component for filter wheel based mid-infrared spectrometer is the filter wheel, which has a characteristic of passing only a band of light in a specific spectral region. There are two different types of filter wheels available, a circular variable filter wheel and linear variable filter wheel. In this spectrometer, a circular variable filter was chosen for its good wavenumber selectivity, compact size, and easy positioning.

Dimensions for circular variable filter (CVF) wheel:

Diameter : 4.0 inches

Thickness : 0.125 inches

The spectral range for circular variable filter split into two segments: 0 degrees to 180 degrees and 180 degrees to 360 degrees. Both spectral ranges are from 1880 cm^{-1} to 3600 cm^{-1}.

1883 cm^{-1} to 2300 cm^{-1}, Bandwidth of 200 cm^{-1} or less

2300 cm^{-1} to 3000 cm^{-1}, Bandwidth is between 200 cm^{-1} and 400 cm^{-1}

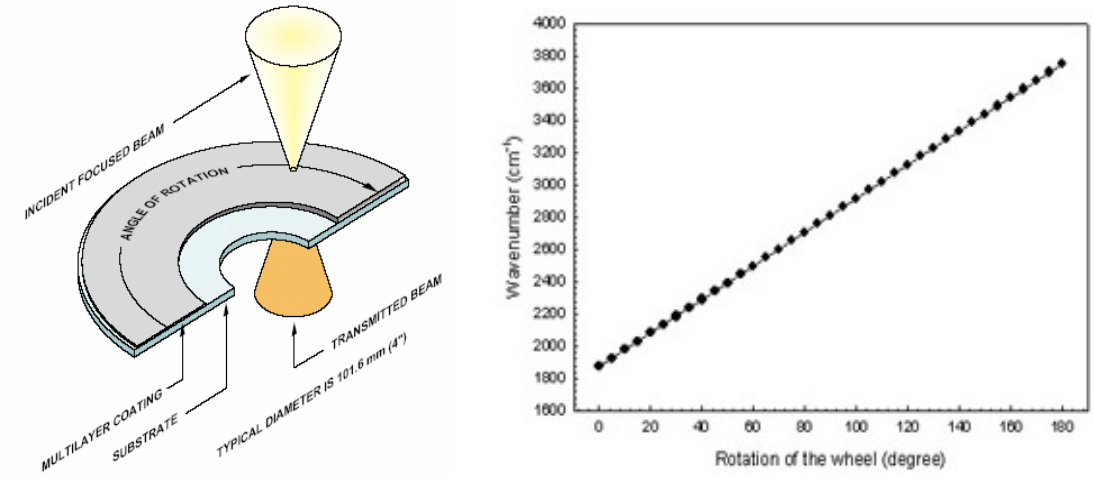
3000 cm^{-1} to 3600 cm^{-1}, Bandwidth of 100 cm^{-1} or less

Circular variable wheels are prepared by depositing thin films on a circular substrate, and the film thickness is varied to get different wavelengths for infrared transmission. The deposited film thickness is linearly varied with the angular position on the substrate. By changing the film thickness, the peak wavenumber allowed by the filter wheel is varied linearly with the angular position [35,36]. Figure 2.6 shows a front view of filter wheel used in the spectrometer.



Figure 2.6: A front view of circular variable filter wheel in the spectrometer

From Figure 2.7 (a), a small portion of the filter wheel is just like a narrow band pass filter. By rotating the filter wheel to an appropriate angle, a specific wavelength can be selected. In Figure 2.7 (b), a half rotation of the wheel (from 0 degree to 180 degree) will make a complete scan of the filter's spectrum from 1873 cm^{-1} to 3751 cm^{-1}. Since the peak wavenumber is almost linearly dependent on the angular position, calibration for the filter wheel can be accomplished [35, 36].



(a) (b)

Figure 2.7: Half segment of filter wheel showing the linear variation of the film thickness with the angular position [36]

Figure 2.8 (a) shows the setup of the blackbody, the filter wheel and the MCT infrared detector. Figure 2.8 (b) is the blackbody spectrum with and without the filter wheel. The solid plot in Figure 2.8 (b) indicates that the filter wheel drastically narrows the band of light passing through it.

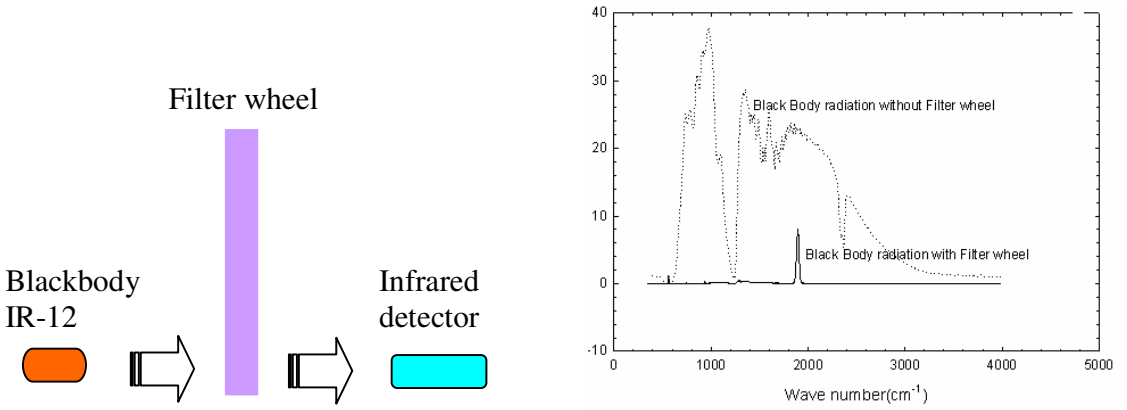


Figure 2 8: (a) Schematic of the blackbody beam passing through the filter wheel. (b) Comparison of black body radiation on the FTIR spectrometer before and after the filter wheel. [37]

Based on the setup in Figure 2.8 (a), the filter wheel was moved in anticlockwise direction and the IR spectra were saved for every two degrees. Simultaneously, peak wavenumber and the peak intensity were recorded. The following plot in Figure 2.9 shows the IR spectrum, which was tested by the rotating filter wheel every two degrees in the counterclockwise direction.

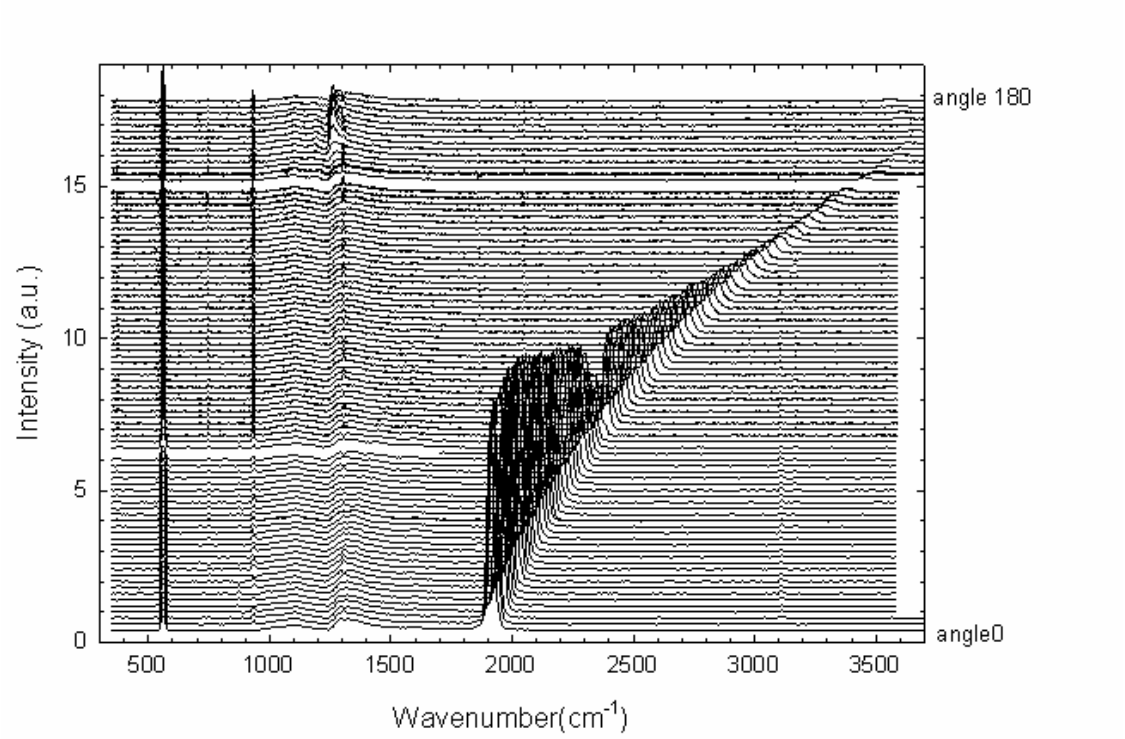


Figure 2.9: Transmittance of the Circular Variable Filter wheel for every 2 degrees [37]

There are several conventional methods to clean a filter wheel, such as dry nitrogen gas blowing, a clean specific wiper for lens cleaning, and so on. The lowest operating temperature for these filter wheels are 7K. Since the optical alignment with a filter wheel is easy to obtain, a filter wheel is more flexible than a grating monochrometer, which requires bulky and expensive beam handling optics.

2.2.3 Special stand for the circular variable filter wheel

In the laboratory, a special stand was prepared for holding and rotating the filter wheel. Five components were used for this special stand.

- Two cylindrical rods
- Two gears
- Base to hold all components
- Stepper Motor
- Circular scale with an indicator

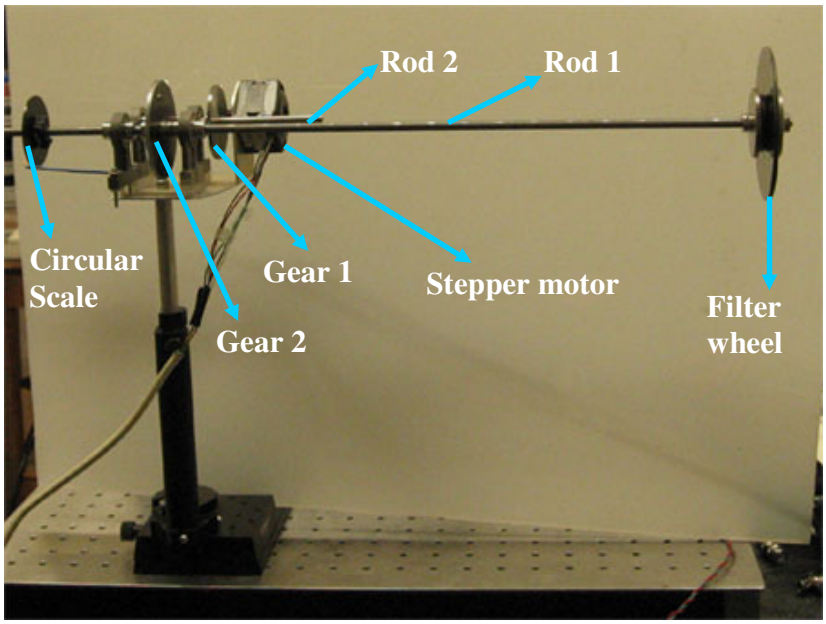


Figure 2.10: Picture of the circular variable filter wheel with its stand

Figure 2.10 shows a steel cylindrical rod 1 (15 inches long and 0.25 inches diameter), the filter wheel, Gear 1 and a stepper motor all connected together. Gear 2 is fixed on a shorter cylindrical rod 2 (5 inches long and 0.25 inches wide) and geared with gear 1. The circular scale was also connected on the side of rod 2.

A stepper motor driven by a stepper motor controller MC3479P was used to rotate the filter, and the circular scale was able to display the current degree. The stepper motor was interfaced to the computer through a data acquisition connector block (BNC 2110)

[38]. The circuit of BNC 2110 shown in Figure 2.11 was constructed on the bread board for automated operation.

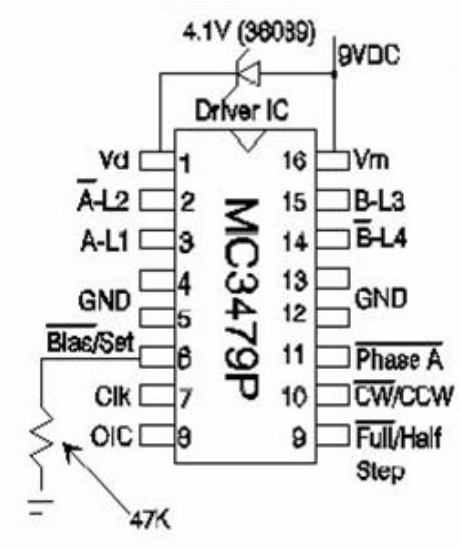


Figure 2.11: MC3479P Stepper motor controller used on BNC 2110 [38]

2.2.4 Special sample holder

A special sample holder was prepared for sample temperature controlling during characterization. Five components were used.

- Thermo-electric cooler (TEC)
- Thermistor
- Copper bar
- Heat sink with a DC fan motor
- Thermal interface adhesive pad

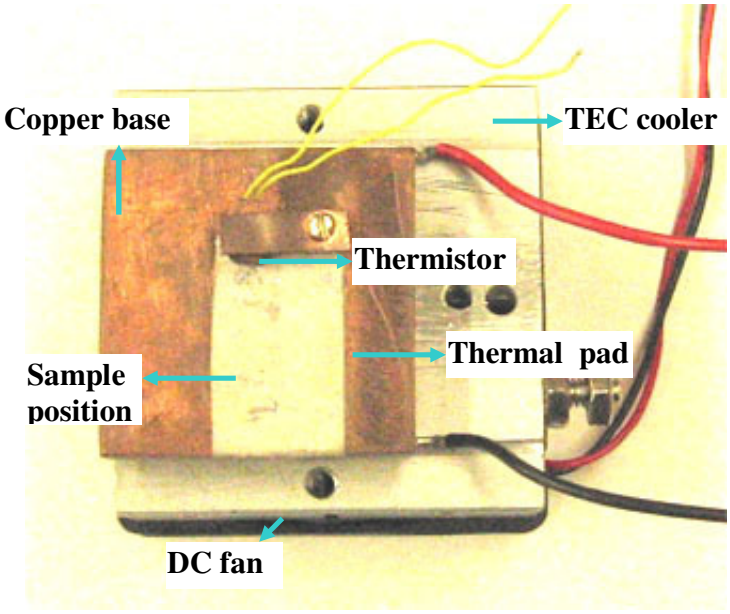


Figure 2.12: Picture of the special sample holder

Figure 2.12 shows a picture of the sample holder consisting of a copper base (1"x 1"x 0.12") and a thermal interface adhesive pad (ADI-ALO-119-135) for attaching a sample. A thermistor was also fixed on thermal pad for temperature monitoring, and temperature data from the thermistor was coupled with a TEC module in a LDC-3900 modular laser diode controller to control the TEC module. The TEC module in a LDC-3900 modular laser diode controller can adjust the copper base temperature by controlling the TEC driving current [39].

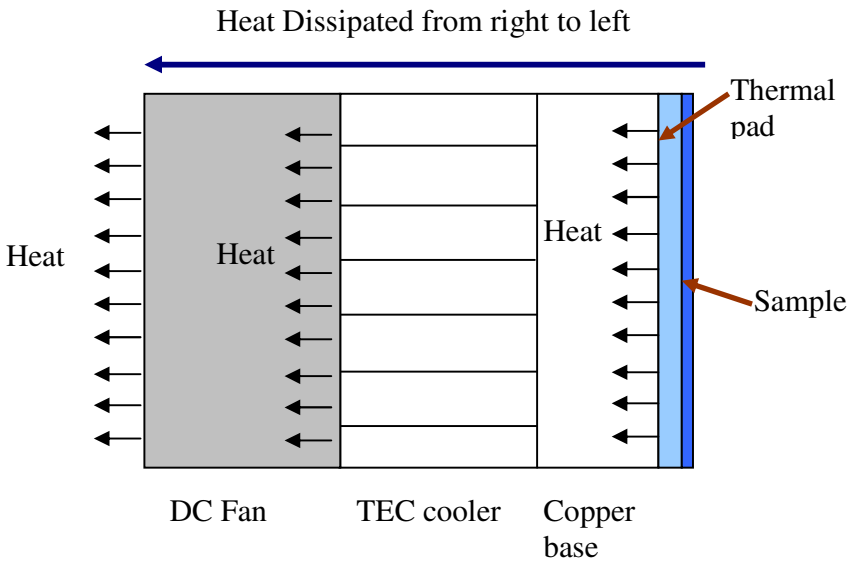


Figure 2.13: Schematic of heat dissipation on the special sample holder

Figure 2.13 shows heat dissipation direction is from right to left. Sample heat generated during the measuring process is transferred to the hot side of TEC cooler by conduction. The TEC cooler can transfer heat from hot side to cold side by its P-N junctions. After that, a DC fan will transfer the heat to the ambient air by convection. So sample heat produced during testing will be dissipated from right to the left.

2.2.5 Pumping with a 911nm laser

Figure 2.14 shows an ILX lightwave LDC-3900 modular laser diode controller is used as a temperature controller for TEC and current source for the pump laser. Both the TEC and thermistor were connected to the temperature controller module of the laser diode controller. Since the thermistor is a thermal sensitive resistor, which resistance can change as the ambient temperature changes, the thermistor was used to monitor the heat sink temperature



Figure 2.14: LDC 3900 diode laser current source with a TEC temperature controller.

The heat sink temperature was set to 10 – 12 ℃. At lower temperature, ambient water condensing could happen on the sample surface, which should be avoided since it could dissolve the BaF_2 layers that are often used in IV-VI semiconductor materials growth.

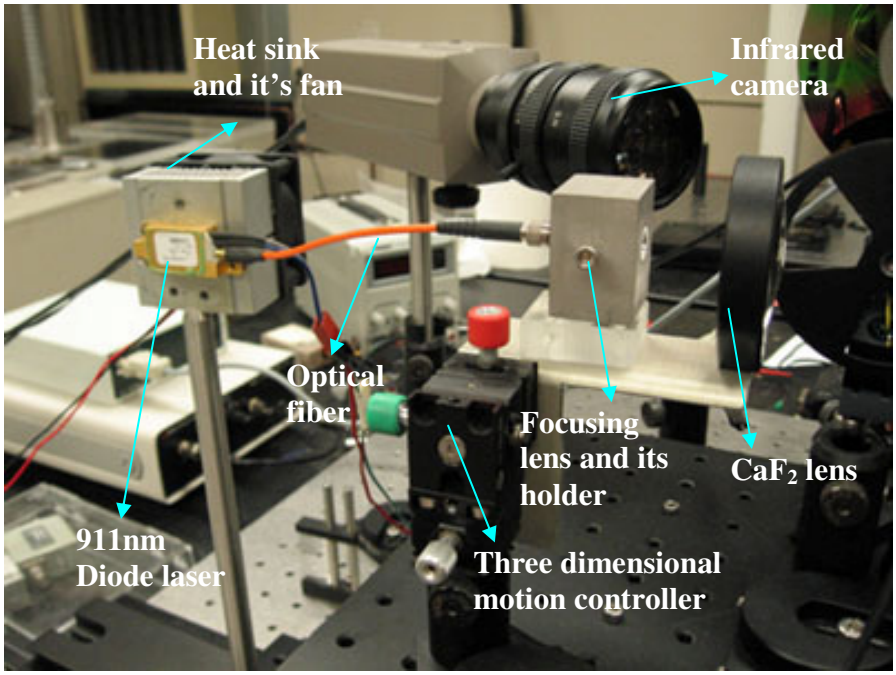


Figure 2.15: Picture of the special laser holder

A fiber-coupled InGaAs diode laser with continuous wave emission is shown in

Figure 2.15. A heat sink and its fan helps to cool the 911 nm laser up to 2 amps of current. The optical fiber and its coupling parts deliver the laser beam to the focusing lens fixed in an aluminum mount, which can be adjusted by a three dimensional axis positioner. A 2 inch diameter focusing CaF_2 lens is able to focus the laser beams on the testing sample surface. By this kind of laser and optical fiber transmission design, the pump laser is easily to be focused on the sample surface.

2.2.6 Infrared detector

The infrared detector is an important component in the spectrometer. An infrared detector is a device which converts the electromagnetic energy from the source to an electrical signal. The detector element is usually put behind an infrared transparent window [40]. Today, Infrared detectors can be classified into two categories, thermal detectors and quantum detectors.

Thermal detectors have a very large negative temperature coefficient (about 4 % / ℃), and a large voltage responsitivity. The main advantages of thermal detectors are room temperature operation, and small responsitivity dependence on wavelength. However, compared with quantum detectors, thermistor detectors have a lower sensitivity and responsivity.

Semiconductor quantum detectors have a higher responsivity and sensitivity than thermal detectors. The detectors detect the infrared emission by changing conductivity (photoconductive detectors) or generating electrical current (photovoltaic detectors) with incident infrared light.

In this spectrometer, a PVI-2TE-5 type quantum detector from Vigo System is

chosen for infrared light detection since it has a 3 - 5 μ m detection range. PVI-2TE-5 type detector is equipped with a two-stage TE-cooled HgCdZnTe IR photovoltaic detector, which is optically immersed with a high refractive index CdZnTe.

PVI-2TE-5 type quantum detector is cooled by a thermocooler driven by a standard thermoelectric cooler controller. Figure 2.16 shows a picture of a PVI-2TE-5 type detector with its thermoelectric cooler controller.



Figure 2.16: Picture of and PVI-2TE-5 type quantum detector and its controller

Figure 2.17 shows that PVI-2TE-5 detector has good detectivity, $D^*>1\times10^{10}$ $cmHzW^{1/2}$, in a range from 2.5 to 5 μm. This range matches the spectral range covered by the circular variable filter wheel.

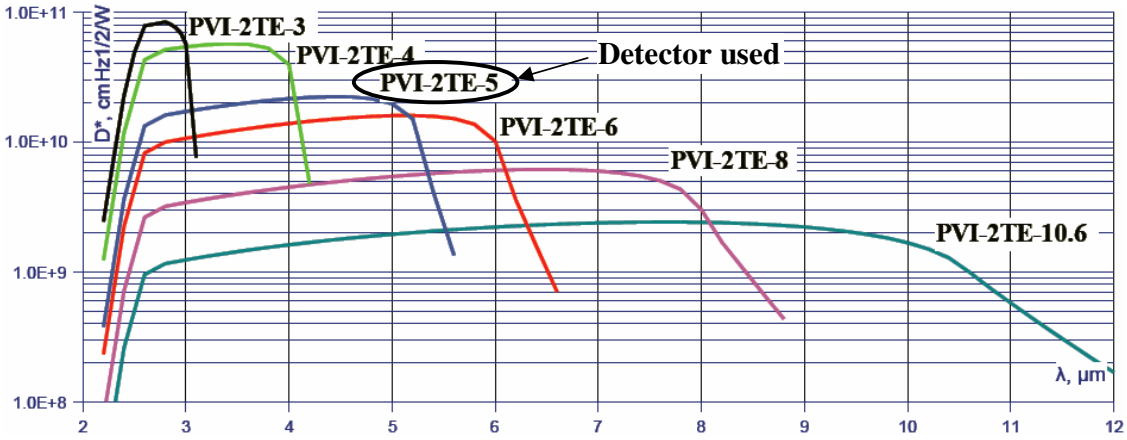


Figure 2.17: Spectral Response of various Vigo system detectors available in infrared region [41]

2.2.7 SR 830 lock-in amplifier

A lock-in amplifier is used in filter wheel based mid-infrared spectrometer to enhance detection sensitivity using harmonic detection. A picture of the Stanford Research SR 830 Lock-in amplifier is shown in Figure 2.18. A HP 54600B oscilloscope shown at top and it was used for signal diagnosing and debugging. An HP 8165A frequency generator, shown in the middle, was used to generate a standard frequency for modulating the pumping laser. The SR 830 lock-in amplifier is located on the bottom [42].

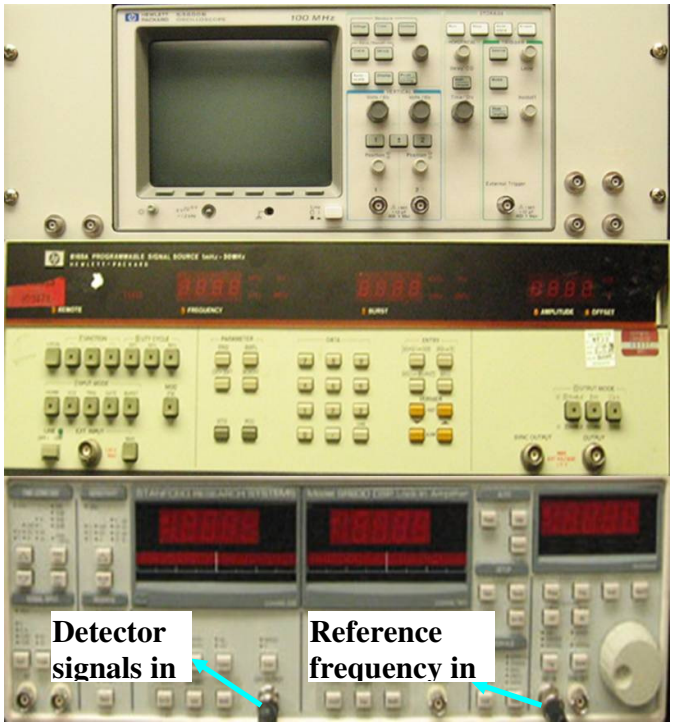


Figure 2.18: Picture of a HP oscilloscope, a frequency generator and SR 830 Lock-in amplifier

The lock-in amplifier utilizes "phase sensitive detection". First, the input signal is amplified by the lock-in reference signal, which has the same frequency as the former signal. Then, the resultant AC signal is filtered out by a low pass filter, and the DC signal will be kept since only the DC signal is proportional to the amplitude of the input signal. For example, if there is a signal voltage Vs and a signal phase angle φs, and a reference voltage Vr and a phase angle φr, the output voltage after SR 830 lock-in amplifier will be

$$V_2 = 1/2\ V_s\ V_r \sin(\varphi_s - \varphi_r)$$

The output of the lock-in amplifier (V_2) will be input into the Labview program for displaying the detector signals.

By using the SR 830 lock-in amplifier, noise can be reduced significantly by low pass filtering. So, besides the circular variable filter wheel, the lock-in amplifier SR 830 is

another essential and critical component in the filter wheel based mid-infrared spectrometer.

2.2.8 GPIB card and Labview program

A National Instruments GPIB card was used for acquiring the lock-in amplifier data. The original Labview coding was modified to process voltage-angle data and plot the corresponding voltage-wavenumber curve in a popup window.

By acquiring data from both the lock-in amplifier (photon intensity information) and stepper motor controller (angle information), the Labview program can display voltage vs. wavenumber data (i.e. PL emission spectrum). Figures 2.19 and 2.20 respectively, show both user interface and coding architecture of the Labview program. Instruction procedures for using the Labview program are attached in appendix B.

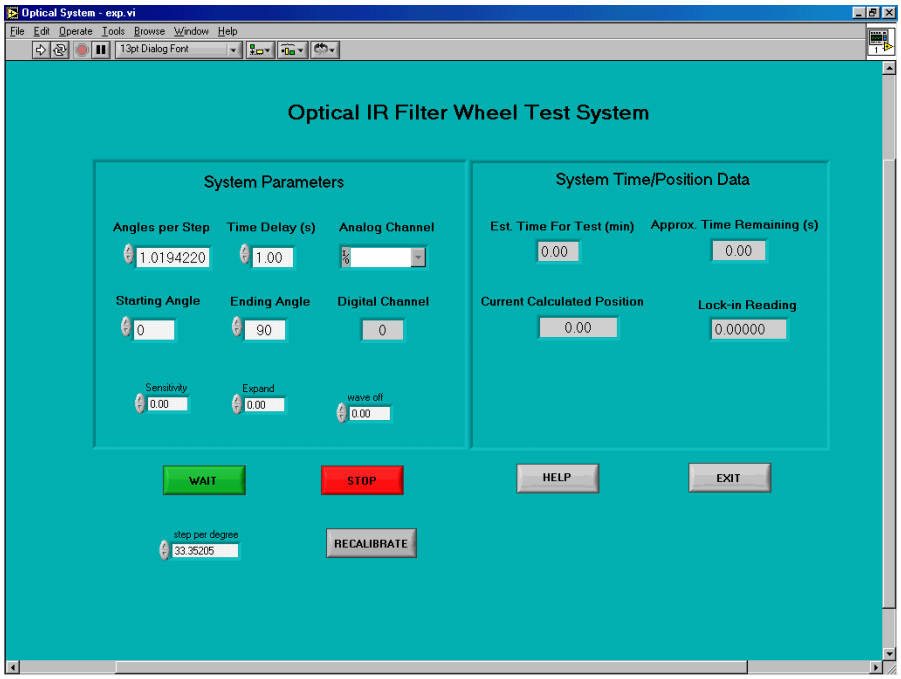


Figure 2.19: Screen shot of the labview program graphical user interface (GUI) for spectrometer

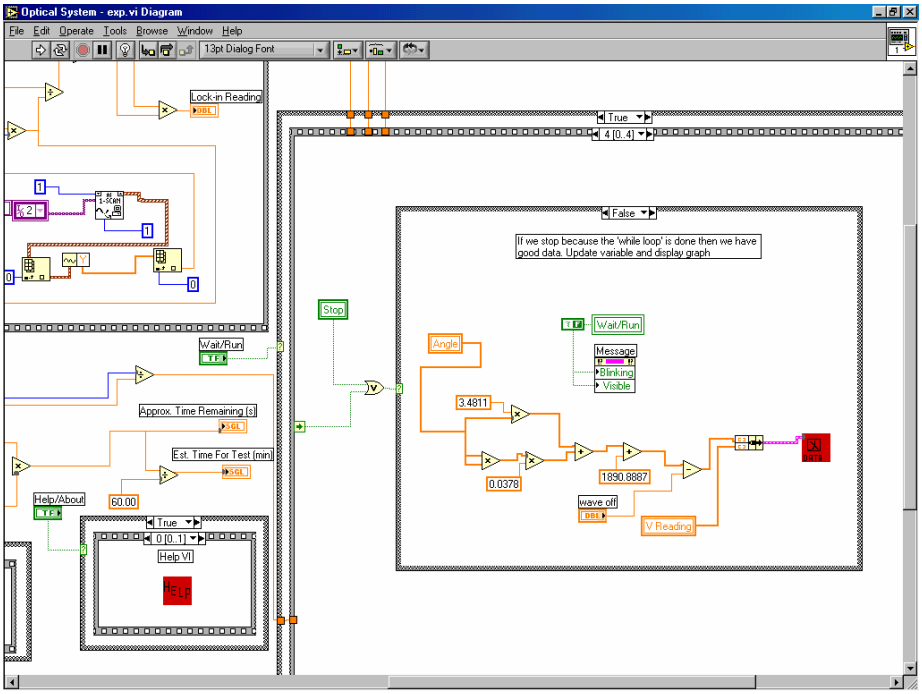


Figure 2.20: Screen shot of the coding architecture in the labview program

The result of analyzing a IV-VI quantum well sample W336 is shown in Figure 2.21. The IV-VI MQW structures W336 was grown by molecular beam epitaxy (MBE) on Si (111) substrates. The layer structure consisted of a 24 nm CaF_2 layer, a 500 nm BaF_2 buffer layer, an undoped 3 μm $Pb_{0.97}Sr_{0.03}Se$ buffer layer, a 40 period MQW structure with 20 nm wells (PbSe), 40 nm barriers ($Pb_{0.97}Sr_{0.03}Se$), and a 10 nm PbSe capping layer to protect strontium against oxidation. The emission wavelength in Figure 2.21 is determined by interband transition energies between quantum wells, and the number of emission modes is limited by the designed Fabry-Perot cavity.

The near-IR diode laser was pumped with 1514 mA, and “Sensivity” and “Ext” in lock-in amplifier is set to “20” and “10”. However, the data saved in txt format will be

more important, since it can be plotted in Sigmaplot and analyzed for emission power estimation.

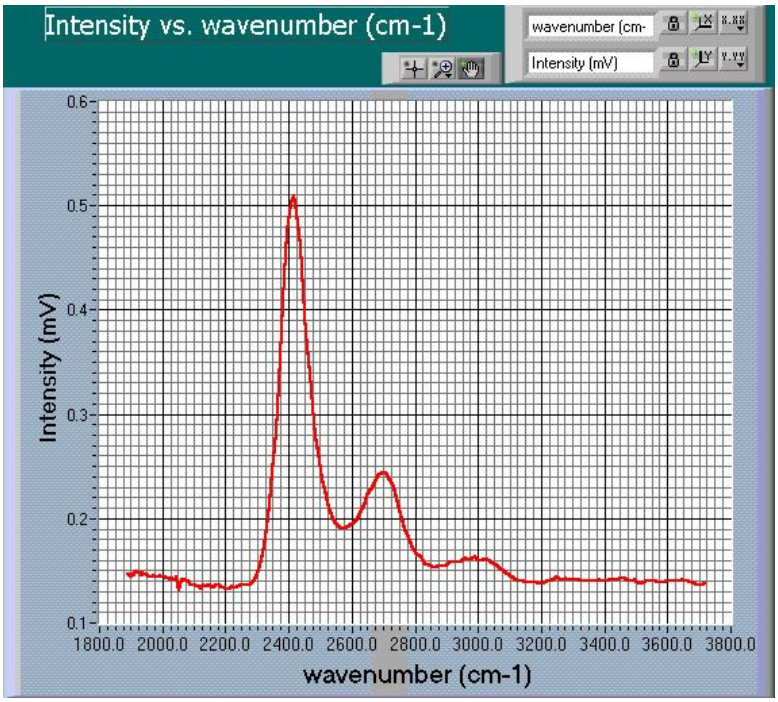


Figure 2.21: Windows displaying the picture of the data saved during the experiment

2.2.9 Infrared blackbody IR-12

An IR-12 infrared blackbody sold by Boston Electronics was used as a standard infrared emitter to help estimate PL emission powers measured by the spectrameter.

Figure 2.22 shows the Infrared blackbody IR-12 size. A Tenma laboratory DC power supply was used as the power source for this blackbody, and blackbody temperature was adjusted by varying voltage or current of DC power supply.

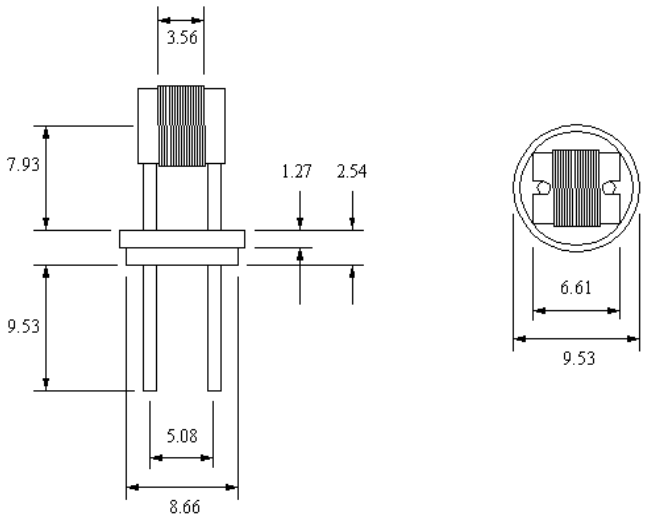


Figure 2.22: Schematic picture of HawkEye Technologies IR-12 series infrared emitter (All the numbers are in mm.) [43]

2.2.9.1 Emissivity of infrared blackbody IR-12

Emissivity is the term which evaluates radiation from any object relative to that of a perfect blackbody. It is an important factor for blackbody emission power calculation. From the data in Figure 2.23, emissvity for infrared blackbody IR-12 is around 0.8.

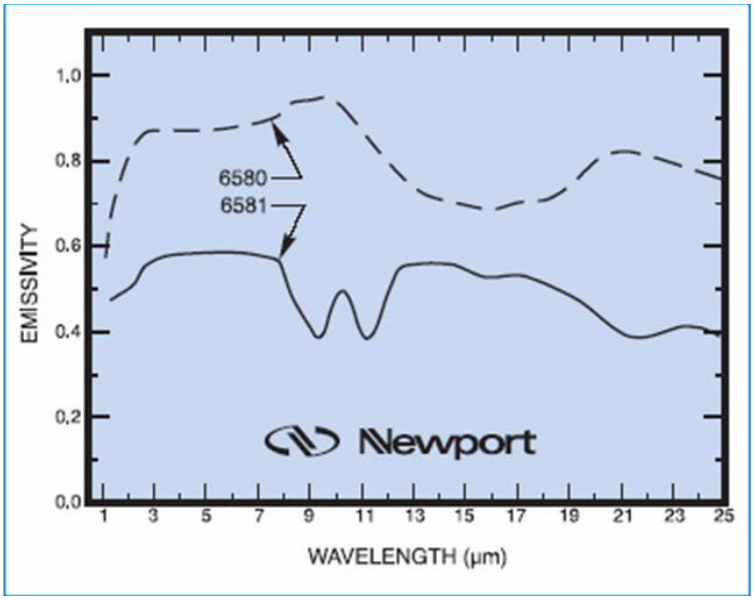


Figure 2.23: Emissvity of HawkEye technologies IR-12 series infrared emitter [43]

2.2.9.2 Temperature of infrared blackbody IR-12

As shown in Figure 2.24, IR-12 surface temperature can also be estimated from curves given in the product manual. There are two different plots in the manual for temperature estimation: “current versus temperature” and “voltage versus temperature”. In this spectrometer, the “current versus temperature” plot was chosen for temperature estimation. The reason to disregard “voltage versus temperature” plot is that the voltage reading is from power supply, which includes the circuit voltage, not the voltage across the blackbody. So the voltage reading on the lab power supply is not the actual voltage applied on the blackbody, and it can not be used for blackbody temperature estimation.

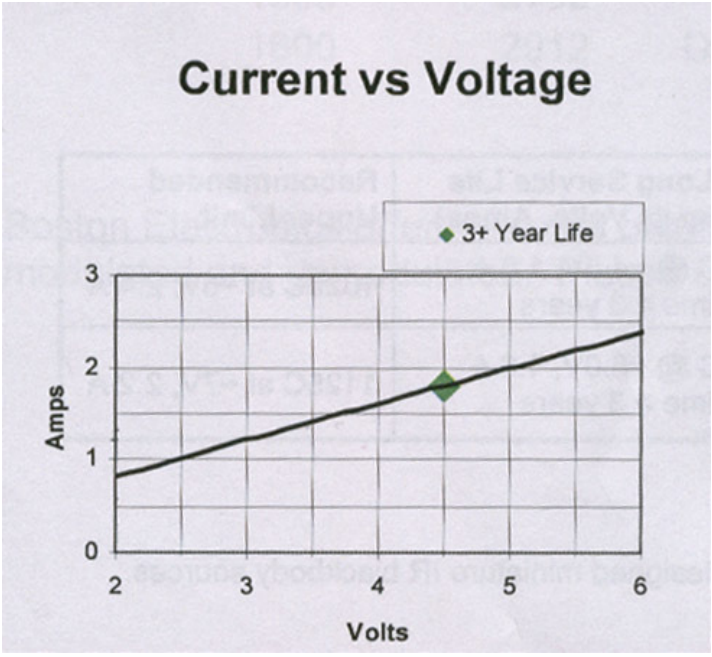


Figure 2.24: Temperature versus Current for HawkEye Technologies IR-12 series infrared emitter [43]

2.2.9.3 Special holder for infrared blackbody IR-12

When a blackbody (infrared emitter) is heated, it emits broadband electromagnetic radiation with many frequencies in all directions. A special mount is made to fix blackbody emission direction and emission area for the theoretical emission power calculation. The special mount is prepared to hold this IR-12 emitter blackbody. In Figure 2.25, the mount consists of an aluminum bar 5.5 cm long and 2.3 cm wide. One hole with 0.02 mm diameter was made in the center of the aluminum bar. An aluminum piece was attached on the post to fix the blackbody IR-12 close to the hole of the aluminum bar.

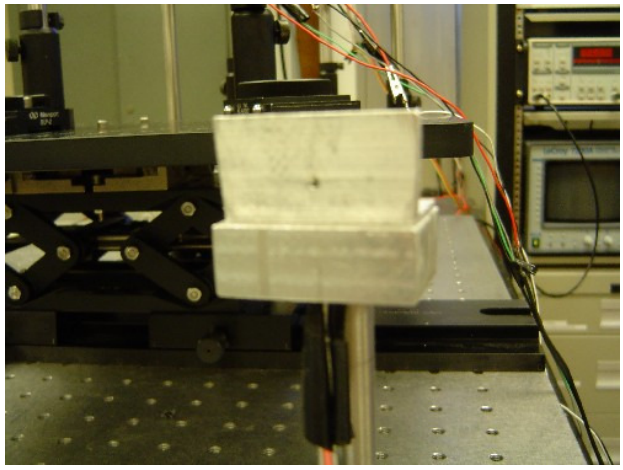


Figure 2.25: Special holder for Infrared blackbody IR-12

2.2.9.4 Solid angle of infrared blackbody IR-12

The solid angle of a blackbody is the maximum emission angle of the blackbody, and is used in the calculation for blackbody emission power. It can be obtained by measuring blackbody emission from the special aperture on the stand [44].

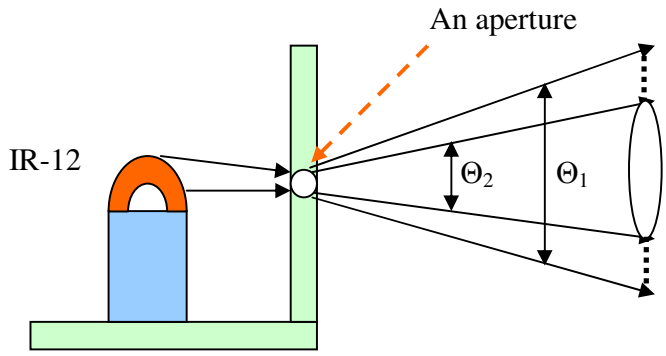


Figure 2.26: Special holder for Infrared blackbody IR-12

In Figure 2.26, there are two solid angles for the blackbody emission: Θ_1 and Θ_2. Θ_1 is the solid angle for which blackbody emission passed through the hole, and Θ_2 is the

solid angle for maximum angle which accept the part of emission from the aperture. So the effective blackbody emission possible detected by the infrared detector will be:

$$P = P_{blackbody} \times (\pi \sin(\theta_2 / 2) / \pi \sin(\theta_1 / 2))$$

2.3 Theoretical blackbody power estimation

Blackbody radiation or *cavity radiation:* an object or system absorbs all radiation incident on it and re-radiates energy which is characteristic of this radiating system only and is not dependent upon the type of radiation which is incident upon it. Figure 2.27 shows a perfect blackbody case, which will absorb all possible radiation and emit all possible radiation without any loss [44].

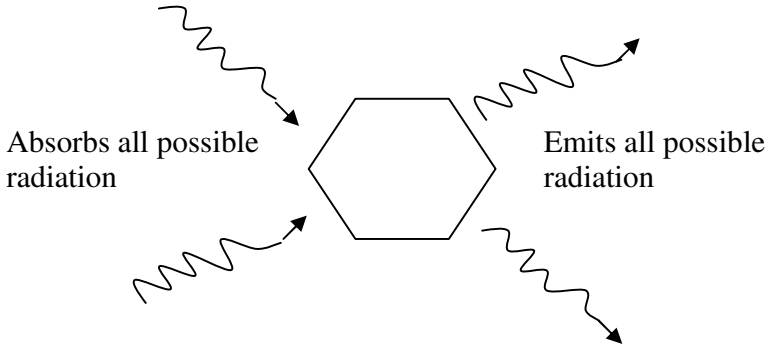


Figure 2.27: Schematic of an ideal blackbody

Theoretically, the spectral intensity of electromagnetic radiation from a blackbody at temperature T is given by Planck's law of blackbody radiation:

$$M_{e,\upsilon}(\upsilon, T) = \frac{2\pi h \upsilon^3}{c^2 \left(e^{h\upsilon/kT} - 1\right)} \qquad watt.s/cm^2$$

If we convert frequency υ into wavelength λ by λ= c / υ.

$$M_{e,\lambda}(\lambda,T) = \frac{2\pi hc^2.10^{16}}{\lambda^5\left(e^{hc.10000/k\lambda T}-1\right)} \quad watt/cm^2\mu$$

If we convert wavelength λ(m) to wavenumber γ(cm^{-1})

$$M_{e,\gamma}(\gamma,T) = \frac{2\pi hc^2\gamma^3}{\left(e^{hc\gamma/kT}-1\right)} \qquad watt.cm/cm^2$$

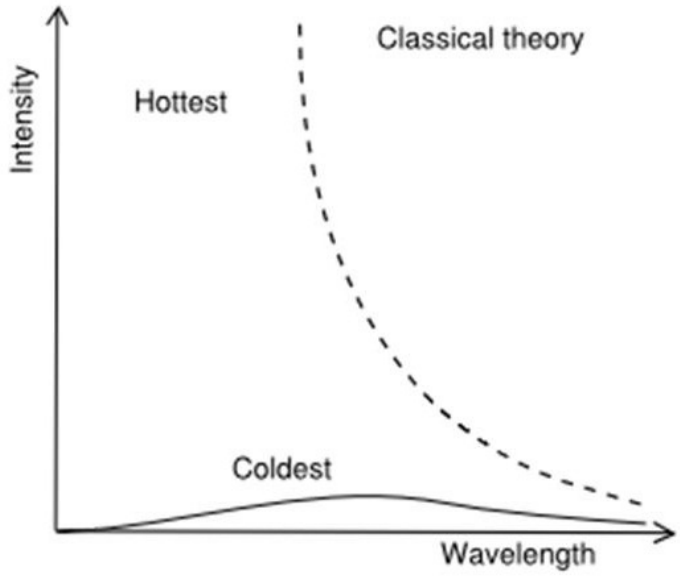


Figure 2.28: Schematic of wavelength versus intensity in cases of coldest, hottest and classical theory

Figure 2.28 shows the relation between emission wavelength and emission intensity for the ideal, coldest and hottest blackbodies. To calculate the total infrared (3μm - 5μm) emission from a blackbody, we must integrate the above equations over the whole wavelength (frequency and wavenumber respectively) range, which gives the Stephen Boltzmann equation below.

$$M_e(T) = \int_0^\infty \frac{2\pi hc^2.10^{16}}{\lambda^5\left(e^{hc.10000/k\lambda T}-1\right)}d\lambda \quad = \frac{2\pi^5k^4}{15c^2h^3}T^4 \qquad watt/cm^2$$

This equation will be the basic equation for the blackbody IR-12 emission power calculation below.

2.3.1 Blackbody IR-12 emission power calibration

Three steps are given to calculated the IR-12 emission power between 1873 cm^{-1} to 3658cm^{-1}

a. For a given temperature, calculate the emission power versus wavenumber relation of IR12 for a certain emission area

b. Based on the data, the blackbody curve is plotted, and the area under the curve is calculated to get IR-12 emission power for all wavenumbers

c. Between 1873 cm-^{1} to 3658 cm^{-1}, the area under the curve is calculated, which gives partial power from 1873 cm^{-1}—3751 cm^{-1}

(PA is Partial power from 1873cm^{-1}-3751 cm^{-1})

Table 2.1: Estimations of emission power between 1873 cm^{-1} and 3658 cm^{-1} (Aperture diameter = 0.02 mm)

Temperature (K)	Power calculated from SB law From 0 to ∞ cm^{-1} (W)	Power obtained from IR-12 curve From 0 to ∞ cm^{-1}(W)	Partial power from 1873cm^{-1}--3751cm^{-1} (W)
838	0.0904	0.0914	0.0425
923	0.1337	0.1346	0.0642
973	0.1654	0.1662	0.0803
1013	0.1945	0.1952	0.0933
1098	0.2691	0.2695	0.1254

Table 2.1 is calculated emission power results of blackbody IR-12. The formula used in calculation was: $M_e(T) = \int_0^\infty \frac{2\pi hc^2.10^{16}}{\lambda^5\left(e^{hc.10000/k\lambda T}-1\right)} d\lambda = \frac{2\pi^5 k^4}{15c^2h^3}T^4 \quad watt/cm^2$.

2.3.2 Solid angle calculation of blackbody emission

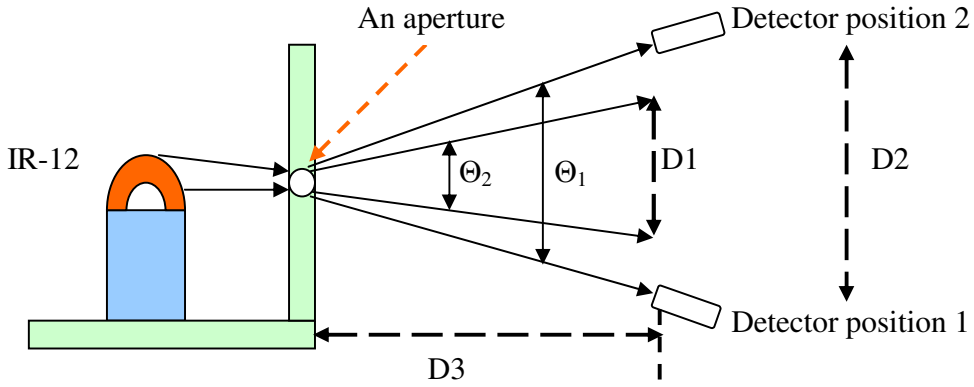


Figure 2.29: Schematic of solid angle calculation for IR-12

Though emission power results of blackbody IR-12 at different temperatures were calculated in Table 2.1, solid angle factors were not calculated yet.

As described in the components part, solid angle Θ_1 and Θ_2 are measured by a separate handle infrared detector. In Figure 2.29, D1 was the diameter size of CaF_2 lens, D2 was measured from the distance between two maximum detector angle positions, and D3 was the distance between the aperture and the CaF_2 lens position.

Θ_1 = arctan (D2/D3) = 32 degree Θ_2 = arctan (D1/D3) = 28.06 degree

Solid angle of CaF_2 lens = $\pi\sin^2(\Theta_1/2)$ = 0.1847 Sr

Solid angle of emission from the aperture

= $\pi\sin^2(\Theta_2/2)$ = 0.2386 Sr

Effective IR-12 emission power will be given by the formula:

$$P = P_{blackbody} * \{\pi \sin^2(\Theta_2/2) / \pi \sin^2(\Theta_1/2)\}$$

$$= P_{blackbody} * \{0.1847 \text{ Sr} / 0.2386 \text{ Sr}\}$$

$$= P_{blackbody} * 0.73$$

2.3.3 Solid angle of blackbody emission

The effective IR-12 emission power will be given by the formula

$$P = P_{blackbody} * 0.73$$

For all the estimations of emission power between 1873cm^{-1} and 3658cm^{-1} in table 1, a correction that emission blackbody power should be multiplied by a solid angle factor 0.73.

So the new effective emission power data of blackbody IR-12 at different temperatures were given in Table 2.2.

Table 2.2: Temperature estimations of infrared blackbody IR-12

Temperature (K)	838	923	973	1013	1098
Emission power 1873 cm^{-1}--3751cm^{-1} (W)	0.0425	0.0642	0.0803	0.0933	0.1254
Effective emission power for the infrared detector 1873cm^{-1}--3751cm^{-1} (W)	0.0310	0.0469	0.0586	0.0680	0.0913

2.4 Estimation of IR-12 emission power between 1873 cm^{-1} to 3658cm^{-1}

2.4.1 Experimental setup

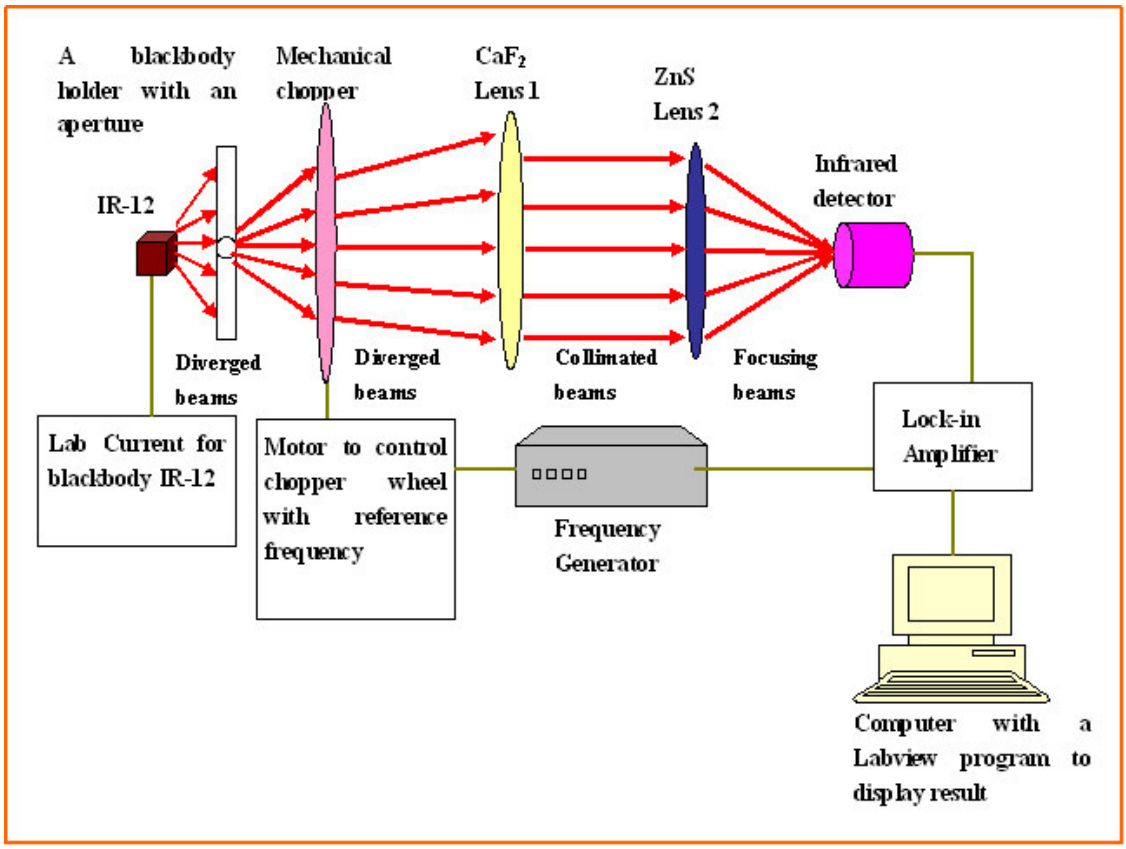


Figure 2.30: Schematic of experimental setup for IR-12 emission power estimation

In Figure 2.30, main components are:

1. Infrared blackbody IR-12: Emission source for power estimation
2. Mechanic chopper: A kind of device to chop continuous Infrared light emission, and produce a square wave signal
3. CaF_2 lens 1: Collecting and converging infrared light into parallel infrared lights

4. ZnS lens 2: Focusing parallel infrared lights into a very small area into the infrared detector
5. Infrared detector: Detecting infrared lights, converting into electrical signal
6. Frequency generator: Generating reference frequency for motor and oscilloscope
7. Motor: controlling the chopper with the reference frequency
8. Lock-in Amplifier: Amplifying signals and reduce noise level by many fold
9. Computer with corresponding Labview program: Displaying the final detector signal with reference signal

Infrared emission from IR-12 was chopped by the mechanic chopper, which was driven by a motor with the frequency generated from the HP frequency generator. CaF_2 lens 1 collected the diverged beams and converted into collimated beams. ZnS lens 2 focused the collimated infrared light onto a small detection area inside the infrared detector. The infrared detector converted the incident beams into electrical signal. The lock-in amplifier amplified the detected signal and reduced the noise. A Labview program on the computer acquired the signal from the lock-in amplifier and displayed the result on the computer screen.

Blackbody IR-12 emissions at different temperatures (838 K, 923 K, 973 K. 1013 K and 1098 K) were measured by the experimental setup mentioned above. And “voltage versus wavenumber” curves were plotted under its corresponding blackbody temperature. These five curves are used as references for photoluminescence power estimation of the IV-VI quantum well sample W336.

2.5 Photoluminescence power estimation of IV-VI quantum well W336

2.5.1 Experimental setup

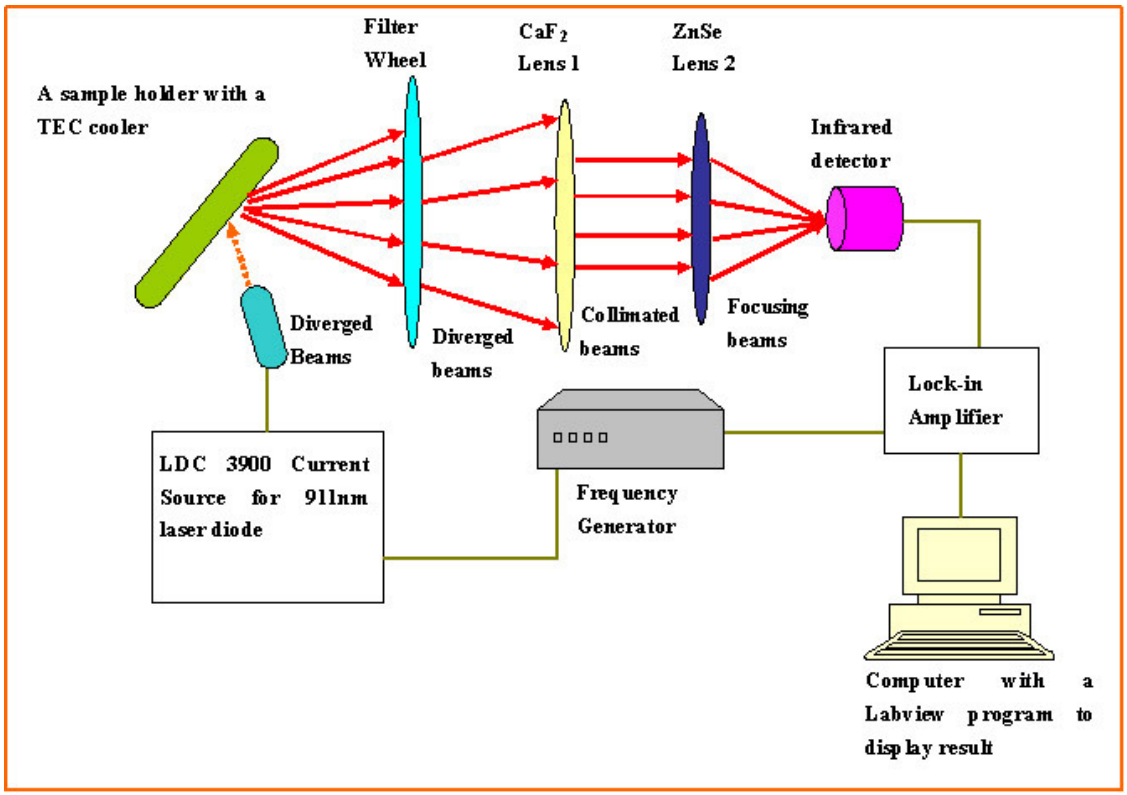


Figure 2.31: Schematic of experimental setup for IR-12 emission power estimation

In Figure 2.31, the main components are:

1. A special sample holder with a TEC cooler for IV-VI quantum well sample W336: photoluminescence sample
2. LDC 3900 current source and 911nm laser diode: pumping source to produce photoluminescence
3. Circular variable wheel: Allow a specific band of infrared light to pass through

4. CaF_2 lens 1: collecting and converging infrared light into parallel infrared lights
5. ZnS lens 2: Focusing parallel infrared lights into a very small area into the infrared detector
6. Infrared detector: Detecting infrared lights, converting into electrical signal
7. Frequency generator: Generating reference frequency for motor and oscilloscope
8. Motor: Controlling the chopper with the reference frequency
9. Lock-in Amplifier: Amplifying signals and reduce noise level by many folds
10. Computer with corresponding labview program: Displaying the final detector signal with reference signal

A LDC 3900 drive 911nm diode laser was coupled with a reference frequency generated by HP frequency generator. Diverse photoluminescence was excited by a 911nm laser beam and passed through the circular filter wheel. CaF_2 lens 1 collected the diverged beams to collimate the beams. The ZnS lens 2 focused the collimated beams onto a small detection area inside the infrared detector. The infrared detector converted the incident beams into electrical signal. The lock-in amplifier amplified the detected signal and reduced the noise. The Labview program on the computer acquired the signal from the lock-in amplifier and displayed the result on the computer screen.

Photoluminescence emission of IV-VI quantum well sample W336 was measured by this experimental setup successfully. And the “voltage versus wavenumber” curve of quantum well sample W336 was plotted for photoluminescence power estimation.

2.5.2 Photoluminescence power estimation

Basic idea for photoluminescence is that, using calculated blackbody power at different temperatures as references, based on following relation

$P_{pl} / P_{blackbody}$ = Area (pl) / Area (blackbody)

(P_{pl} is the photoluminescence power, P blackbody is the blackbody emission power from 3 -5 μm, Area (pl) is the photoluminescence area under the curve detected by filter wheel based system and Area (blackbody) is the photoluminescence area under the curve detected by filter wheel based system.)

Calculated photoluminescence power:

P_{pl} = Area (pl) / Area (blackbody)*) P blackbody

Based on this relation, seven different blackbody temperatures (838 K, 923 K, 973 K. 1013 K and 1098 K) were used as references for the same IV-VI quantum well sample W336 photoluminescence power emission.

A plot of the blackbody spectrum and the CW PL emission of sample W336 at a pump laser current of 1500 mA measured with a FTIR are shown in Figure 2.32. The area under the graph of the blackbody spectra (A_{pl}, FTIR) is a direct measure of the input power for a given temperature.

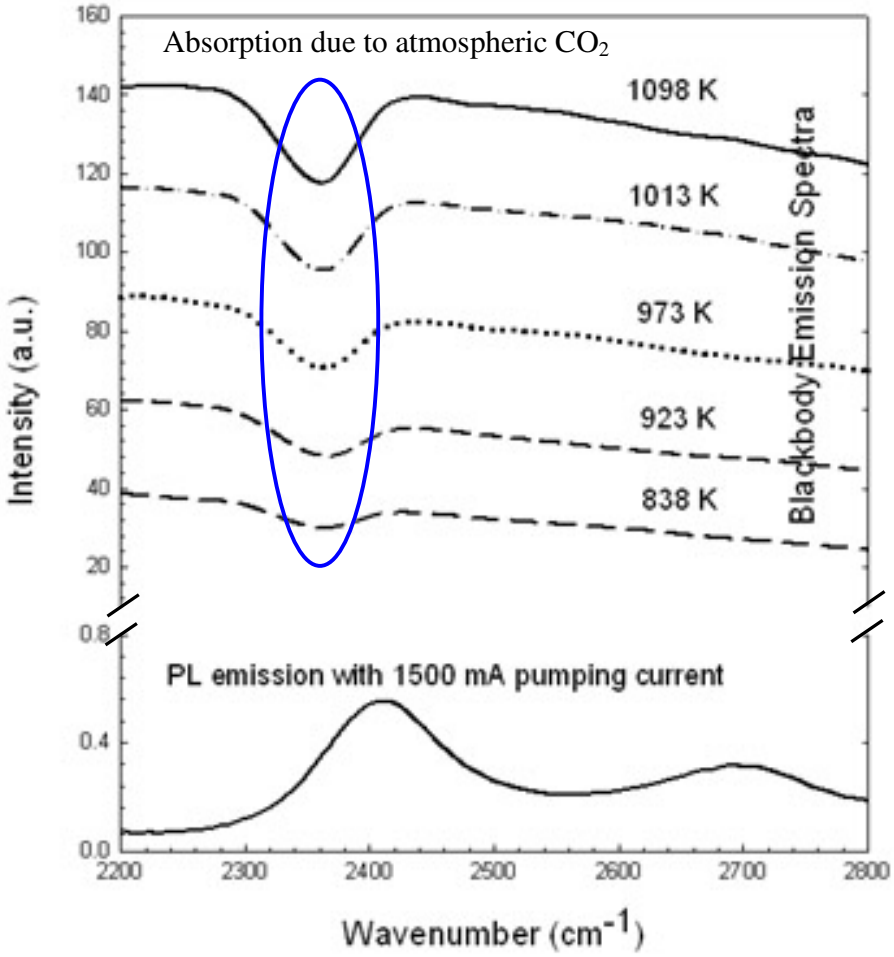


Figure 2.32: Blackbody IR-12 spectrum at different temperatures and PL of W336 at 1500 mA of pumping current on the spectrometer

These values were calculated and are summarized in Table 2.3 along with the area under the graph of the PL from sample W336 (P_{W336}, FTIR).

Table 2.3: Summary of the power estimation of W336 photoluminescence versus different IR-12 temperatures

IR-12 temperature (K)	Area ratio A (W336)/ A (IR-12)	Input power PM (mW)	Estimated PL power (mW)
838	0.00777	0.0310	0.241
923	0.00448	0.0469	0.210
973	0.00291	0.0586	0.171
1013	0.00208	0.0680	0.141
1098	0.00167	0.0913	0.153

Table 2.3 shows different photoluminescence power estimations based on different blackbody temperature curves. W336 photoluminescence power varies from 0.141 to 0.241 mW. The average is about 0.183 mW.

Since we got IR-12 temperatures according to voltage—temperature curve, there are some deviation between measured values and actual values. However, the deviation should be less 100 K.

Since blackbody temperature 825 ℃ (1098 K) at 4.5 V 1.8 A is given on the IR-12 manual, 1098 K blackbody temperature is more accurate than other blackbody temperature checked from curve. So another estimation data of W336 photoluminescence power could be around 0.153 mW.

2.6 Summary and future work

The filter wheel based mid-infrared spectrometer provides an alternative way to measure photoluminescence and laser emission of optoelectronic devices. Different than Fourier Transform Infrared Spectroscopy (FTIR), this spectrometer offers:

- A better sensitivity than the standard FTIR spectrometer because the lock-in amplifier in the spectrometer can reduce the impact of detector noise
- Simple and easy to align
- Capability to measure time-resolved light emission and thus extract excited state electron lifetimes

However there are some disadvantages for this spectrometer:

- Time consuming compared with FTIR measurement. Each measurement will take about 3-5 minutes in optical wheel based system
- Detector limitation: Due to 3 -5 μm detectivity, the measuring range is relatively narrow compared with Fourier Transform Infrared spectrometer (FTIR)

Based on this spectrometer, infrared blackbody IR-12 emission power at different temperatures (838 K, 923 K, 973 K. 1013 K and 1098 K) were calculated. When considering infrared blackbody emission factors, solid angles and emissvity, further correction was made to get more accurate emission power estimations of blackbody IR-12 at different temperatures.

Photoluminescence test of IV-VI quantum well sample #W336 was also taken by filter wheel based mid-infrared spectrometer. By calculating the ratio of area under #W336 curve and area under different blackbody temperatures curves, IV-VI quantum well sample

W336 photoluminescence power was estimated to be 0.183 mW when illuminated with a near-IR (911 nm) pump laser having a power of 970 mW.

Since IR-12 temperatures were obtained from the vendar's voltage - temperature curve, there may be some deviation between measured values and actual values. However, the deviation should be less than 10% thus making the PL power estimate accurate to within about 10%.

Since blackbody temperature 1098 K at 4.5 V and 1.8 A was given on the IR-12 manual, 1098 K blackbody temperature is more accurate than other blackbody temperature checked from curve. Therefore the estimation data of W336 photoluminescence power is around 0.153 mW.

In a word, the filter wheel based mid-infrared spectrometer is an alternative way for mid-infrared emission testing. Based on tested results and standard blackbody calculated power data, emission power and external quantum efficiency can be estimated. In future, combining with further data acquiring technique and a quantum detector with a higher detectivity, excited state electron lifetimes can be extracted.

Chapter 3

Quantum Cascade Laser Packaging

3.1 Introduction

In structure growth and device processing, thermal management is one of the most important factors for high-temperature, high-power continuous wave operation of quantum cascade lasers.

The first level of thermal management for quantum cascade lasers is how to package the laser onto its heat sink. The traditional way to mount quantum cascade lasers is called epi-side up method, which attaches the substrate of the laser onto its heat sink. This method introduces a layer of low thermal conductivity material between the active region and the heat sink thus increasing the thermal resistance. Consequently, the epi-side up method results in a poor heat dissipation of the packaged lasers. Another way to mount quantum cascade lasers is called epi-side down, which attaches the active region side of the laser onto its heat sink by metal bonding. The thermal advantages of epi-side down mounting of the semiconductor lasers have been extensively exploited in the near-IR region [45].

A desirable packaging technique could achieve better heat dissipation and low laser threshold currents for optoelectronic devices. Both epi-side down and epi-side up methods for interband quantum cascade lasers from NASA's Jet Propulsion Laboratory are studied in this chapter. The first packaged laser is based on the epi-side down method, which uses a

boron nitride bar as its heat sink with Au-In metal binding. A second packaged laser is based on the epi-side down method, which uses a boron nitride bar as its heat sink with a special mechanical design. The last packaged laser is based on epi-side up method, which uses a copper bar as its heat sink with a tiny high conductivity wire soldered to the active region stripe contact.

Primary equipment used in those packaging techniques are as follows:

- **Ozone generator for organic chemical cleaning**

The Ozone generator (Model GL-1, PCI OZONE CORP) is used to clean the organic impurities on the surface of laser mount base assemblies [46]. Ozone along with ultraviolet light (UV) is used for removing organic contamination on a substrate surface. It is based on the formation of free radicals by the breaking down of ozone (O_3):

O_3 (ozone) = O_2 (oxygen gas) + O (highly reactive oxygen atom)

These decomposed highly reactive oxygen atoms will not re-form ozone as it is not the preferred state. The free oxygen atoms can bond together to form oxygen gas (which accounts for some of the reaction), or they can react with something else to form CO_2 or H_2O.



Figure 3.1: Picture of Ozone generator (Model GL-1, PCI OZONE CORP)

Figure 3.1 is a picture of an ozone generator in the lab for laser mount assembly cleaning.

The laser mount base assembly is placed in a top glass tube, and the ozone percent on the voltage controller panel is normally set from 75% to 100%. A constant flow of oxygen gas lasts about one hour. The oxygen radical reacts with organic compounds and causes them to cleave and break down. These reactions continue in the presence of oxygen radicals until the organics impurities break down by oxidation and forming other gasses such as CO_2 [47].

- **Hummer 10.2 sputtering system (Anatech Ltd.) for removing surface impurity particles**

Argon (Ar+) ion sputtering of the polished and cleaned Cu bar assembly was performed in a sputtering system (Hummer 10.2) before Au and In depositions by a

thermal evaporator.

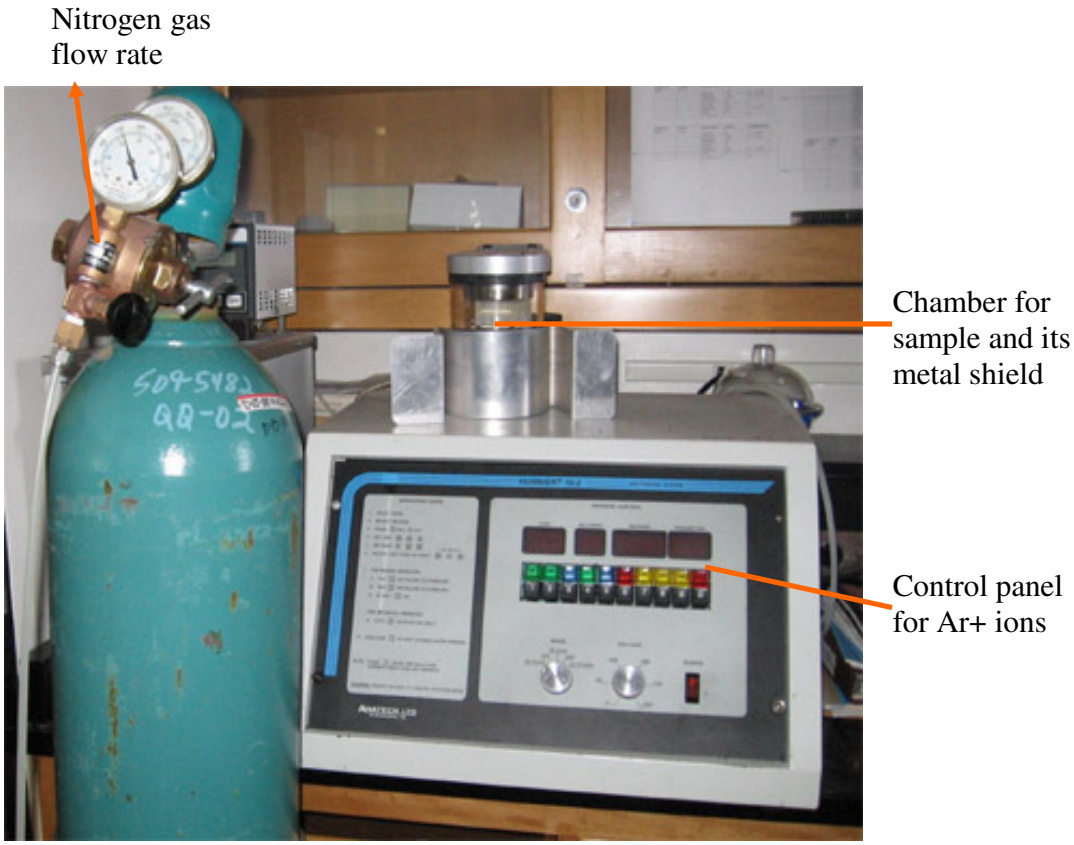


Figure 3.2: Picture of Hummer 10.2 sputtering system (Anatech Ltd.)

Figure 3.2 is a picture of Humer 10.2 sputtering system.

The basic purpose of argon ion sputtering is to clean the laser mount base assembly surface of remaining non-organic contamination after ozone cleaning. The argon ion sputtering process was performed for 600 seconds, and the sputtering current is set to 200 mA and a voltage is set to -1200 V with the inside chamber pressure maintained at 20 mTorr by a mechanical pump.

• **Thermal evaporator Denton vacuum DV-502A system for metal deposition**

Thermal evaporator was used for the thermal depositions of various metallic layers on the laser mount base assemblies. Thermal depositions could be performed in a vacuum of about 1 x 10^{-6} torr for various periods of time, temperatures, and rates of deposition, depending on the type of metal that was deposited.

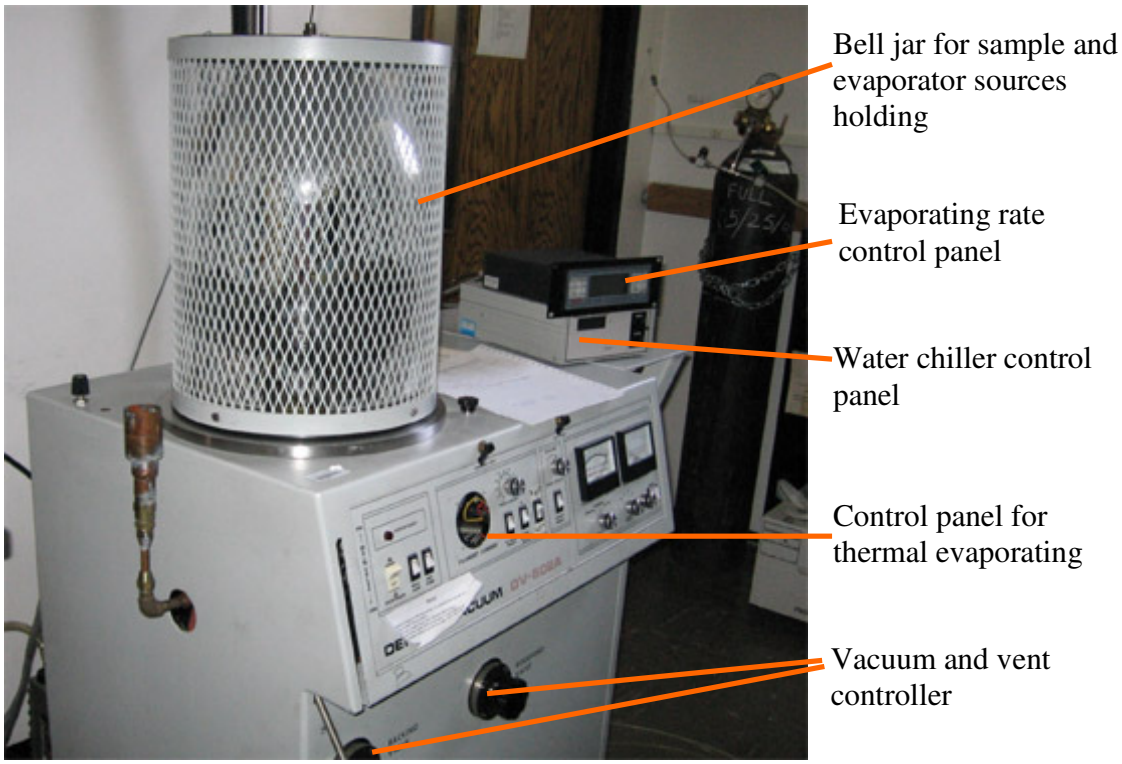


Figure 3.3: Picture of Denton vacuum DV-502A for thermal metallic deposition

Denton Vacuum DV-502A as shown in Figure 3.3 is a system used for depositing thin films onto substrates. The source material is heated to evaporation and then travels through the chamber and deposits onto the samples [48].

Specifications:

Electrical supply: 120VAC, 60 Hz

Vacuum pressure range: 5 x 10^{-4} to 10^{-7} torr

Filament supply: 1 kV

Rod carbon evaporation source

Laser mount base assemblies were loaded together in the bell jar shown in Figure 3.3 for Au and In metallic depositions. The layer of indium is used because indium can form a solid intermetallic compounds with gold. The rate of deposition of the indium layer could reach around 3-4 Å/s because indium has a relatively small atomic mass (compared with gold atoms), a high electrical conductivity $0.116 \times 10^6\ \Omega^{-1}\ cm^{-1}$ and a high thermal conductivity ($0.816\ W\ cm^{-1}\ K^{-1}$).

The layer of gold is used because indium is easily oxidized, and a deposited gold layer will prevent this oxidation. The rate of gold deposition can reach about 1.5 Å/s because gold has a high electrical conductivity ($4.55 \times 10^7\ \Omega^{-1}\ cm^{-1}$) and a high thermal conductivity ($3.17\ W\ cm^{-1}\ K^{-1}$). These properties are desirable for diode laser packaging. Gold deposition is immediately followed by the deposition of indium under the same vacuum in order to prevent the indium layer from oxidizing.

• HP 4061A current-voltage characterization system

Current versus voltage characterization is an effective method to check electrical contacts of electrically pumped optoelectronic devices. Connected with the ground and positive side of optoelectronic devices, current-voltage (I-V) will be obtained with the

setup scanning range.

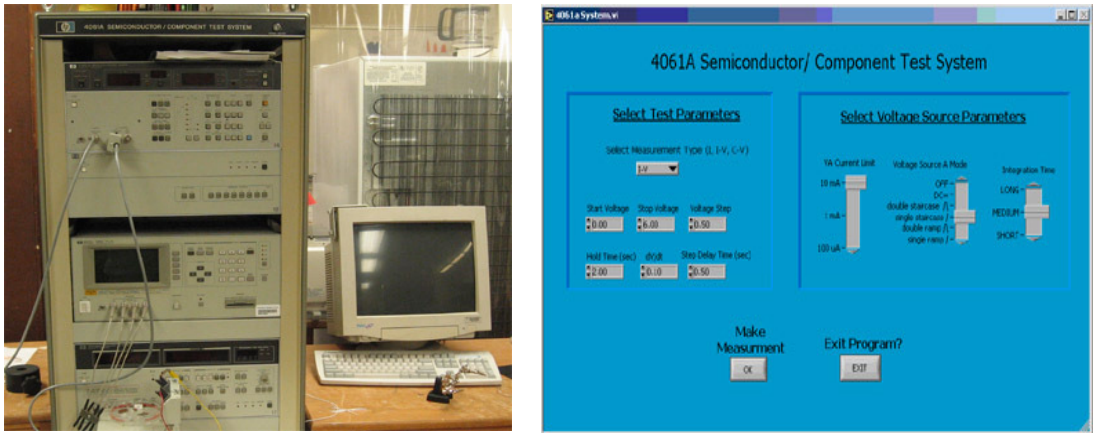


Figure 3.4: HP 4061A I-V characterization equipment (left) and its labview interface (right)

Figure 3.4 is a picture of a HP 4061A I-V characterization system and its LabView interface. Left side is the HP 4061A equipment, its control box and computer for testing data processing. And right side is the LabView interface for the testing setup and the results display. The LabView program was coded to acquire data from the HP 4061A and displayed on the computer screen.

- **K&S model 4124 ball bonder**

The K&S Model 4124 Ball Bonder is a thermosonic unit. The bonding is done at a lower temperature with additional ultrasonic energy. The unit has a 1-mil gold wire installed, and the bonding area is a 152 mm x 152 mm. Wire bonding is a method to make the connection between the die and the package, when a die chip is attached to a package.

Why use gold wire bonding? Gold wire is a conductor, a heat conductor, and resists oxidation and corrosion under room temperature. K&S Model 4124 Ball Bonder operates in two modes, a semi-automatic and manual movement. Basically, the gold wire is fed

through a capillary. An electrical spark melts the tip to form a ball, and the capillary moves downward to touch the bonding pad. After pressure, the capillary moves upward to release some wire and positioned to make the second bond [49].

- **Tencor P-1 long scan profiler**

Tencor P-1 Long Scan Profiler is ideal for measuring and verifying the thickness of vapor deposited films. Film thickness from 100 – 10000 Å can be measured as long as the step height is well defined. Film roughness can also be obtained.

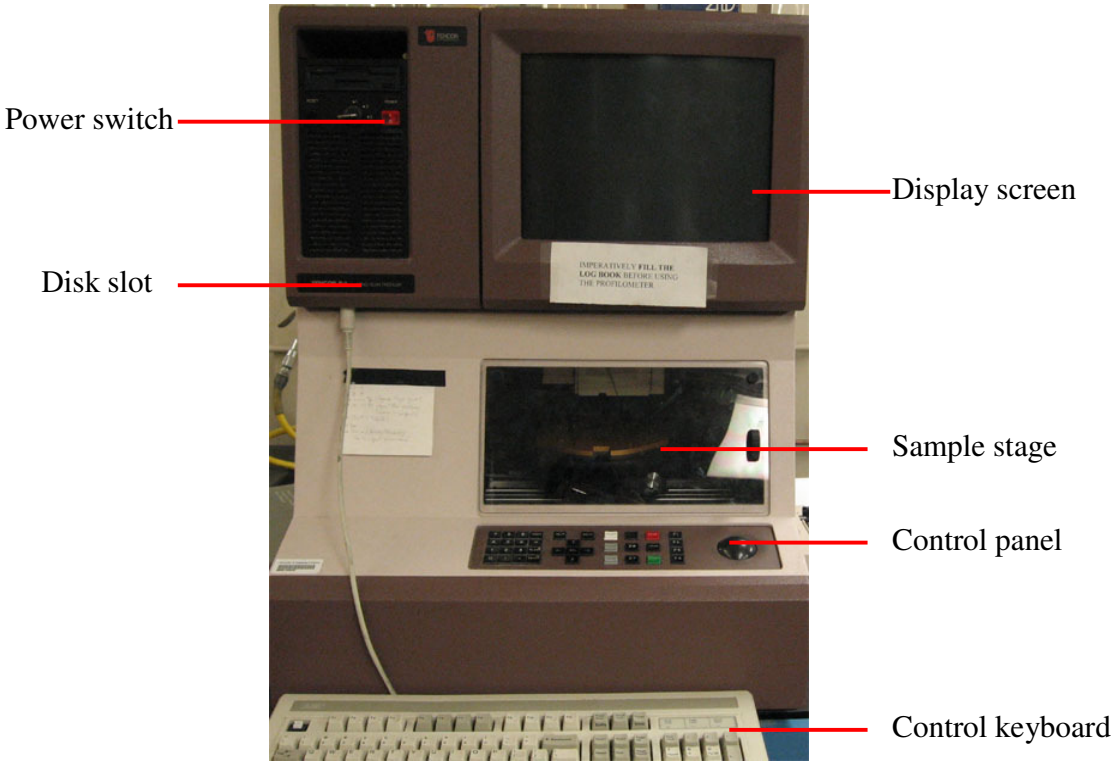


Figure 3.5: Picture of Tencor P-1 Long Scan Profiler

Figure 3.5 is a picture of Tencor P-1 Long Scan Profiler.

Figure 3.6 shows the scanning process from left to right by the Tencor P-1 Long Scan Profiler, where:

- A is calibrating proper determination of the step height distance;
- B is required to establish a baseline. Again, the distance required is subjective and depends on the sample;
- C is such that the stylus does not fall off the edge of the substrate. The same considerations apply when measuring a step down [50].

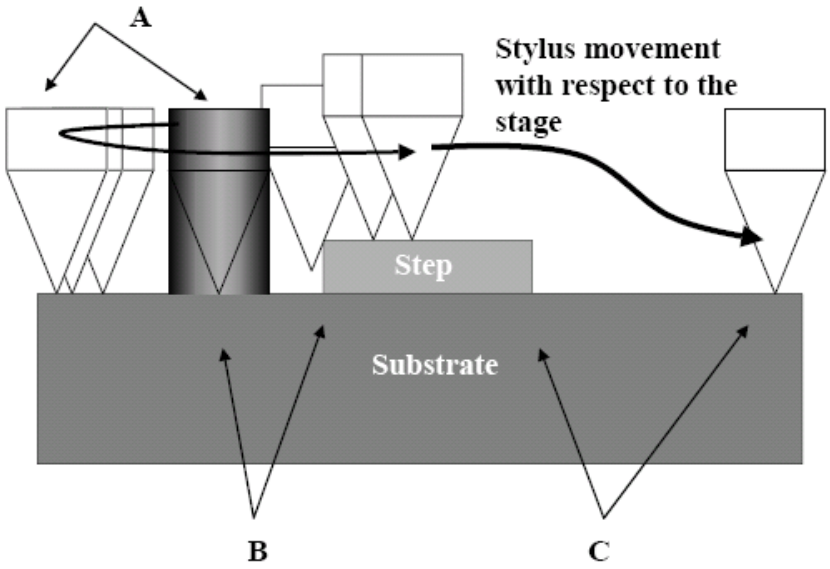


Figure 3.6: Schematic of a scanning process performed by Tencor P-1 Profiler [50]

3.2 First packaged laser with boron nitride heat sink and Au-In metal bonding by epi-side down method

This procedure used a boron nitride bar as the heat sink with Au-In metal bonding. The Jet Propulsion Lab quantum cascade laser top contact has a gold layer with thickness around 300-500 nm. Details of the laser structure are given in Figure 3.7. Au metal contact for laser is about 100μm wide and gap between lasers is about 500 μm.

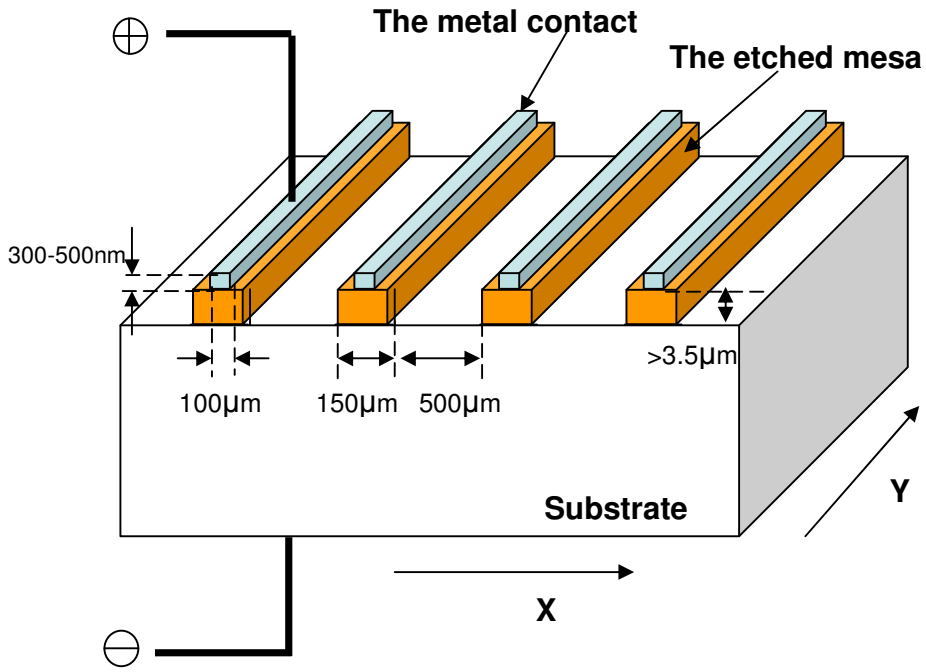


Figure 3.7: Schematic of the Jet Propulsion Lab quantum cascade laser #J435 structure

3.2.1 Basic idea for packaging with metal bonding

Au-In bonding was used for the laser epi-side down method. From the phase diagram in Figure 3.8, there are 5 intermetallic compounds that can be formed: $AuIn_2$ (33.3 at. % Au), AuIn (50 at. % Au), Au_9In_4 (δ)-(69.2% Au), Au_3In (γ)-(75 at. % Au) and Au_4In (β)-(80 at. % Au). $AuIn_2$ is the major intermetallic compound formed by the interdiffusion process. There is very little solid solubility of Au in In, while the solid solubility of In in Au at 700 ^oC and at 406 ^oC are, respectively, 12.64 and 10.36 atomic percent. So the atomic ratio for Au:In should be over 1:2.

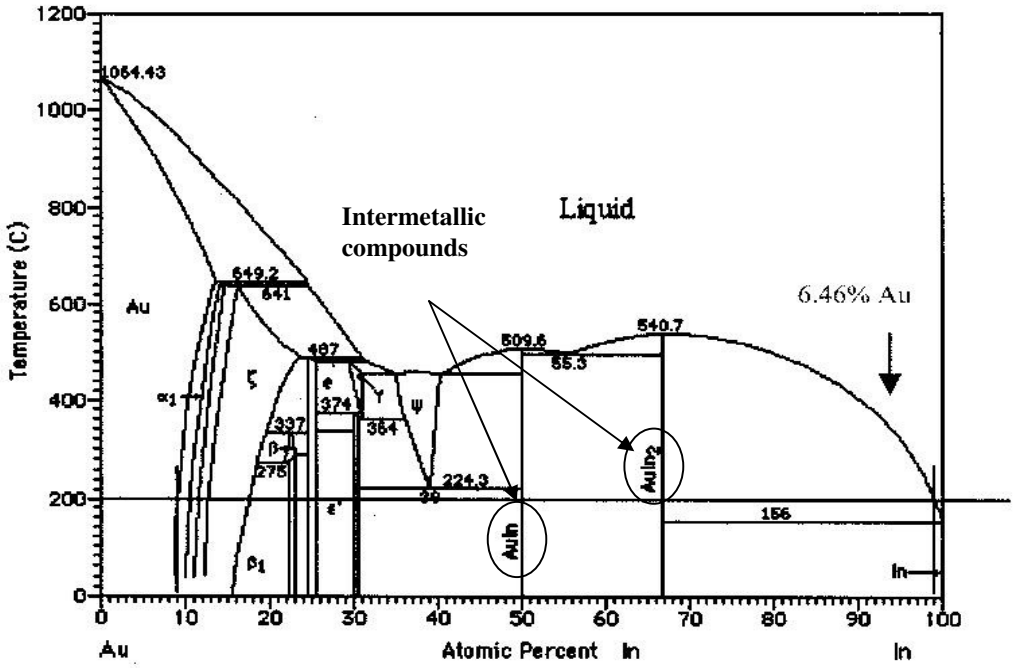


Figure 3.8: Au-In phase diagram [51]

In this packaging technique, the laser was reversed on the top of the boron nitride assembly. Since the top layer on quantum cascade lasers is the gold contact, an Au-In bonding was designed to bind the laser contact stripes with the copper bars on the boron nitride base heat sink.

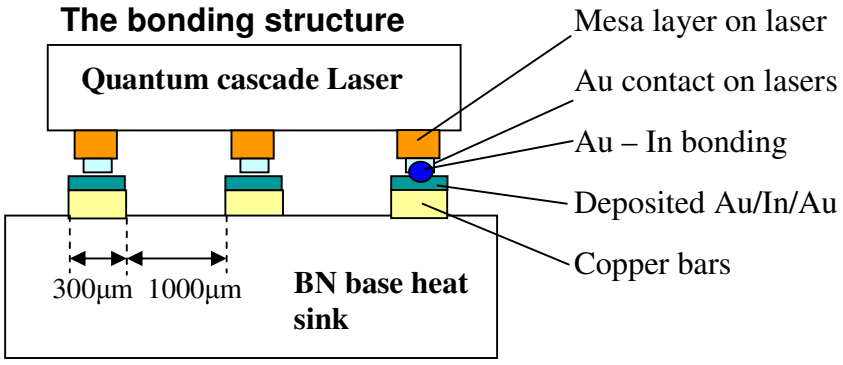


Figure 3.9: Schematic of metal bonding design

From the 500 μm gap between lasers stripes in Figure 3.9, a boron nitride heat sink was made first, and copper bars were attached on the boron nitride base by epoxy with 1000 μm gap between them. So every two laser stripes, one copper bar will match one laser stripe.

For the metal deposition on laser mount assemblies, a layer of gold was deposited on laser mount copper bars first since indium can not adhere very well on copper. A layer of indium was deposited on the deposited gold layer, followed by a layer of gold for anti-oxidation.

3.2.1 Packaging procedure

Despite its high dielectric breakdown strength and good chemical inertness, hexagonal boron nitride is used for substrates for mounting high density and high power electronic components where the high thermal conductivity achieved allows efficient heat dissipation.

In this chapter, Boron nitride slices (95% Hexagonal BN + 5% B_2O_3 Binder) were used as a heat sink material for packaging quantum cascade lasers.

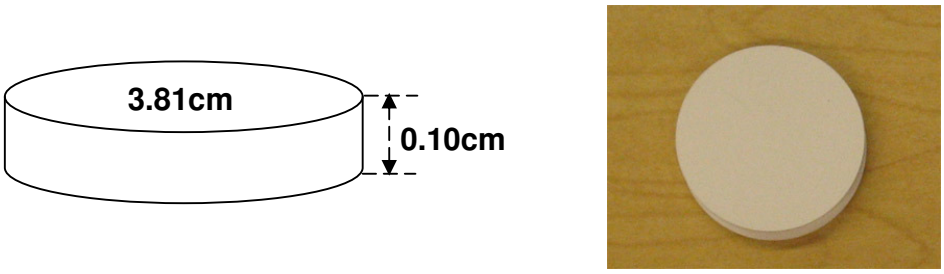


Figure 3.10: Schematic of BN plate and picture of a stack of BN plates

The details of the boron nitride slice size are shown in Figure 3.10 (a). Figure 3.10 (b) is a picture of several stacked boron nitride slices where the diameter is 3.81 cm and thickness is 0.10 cm.

- **Size designing, cutting, drilling and thinning**

Since the laser stripe is tiny, cutting of each boron nitride slice into pieces is necessary. Before cutting, the size design of boron nitride pieces was planned. The size information is given in Figure 3.11. From Figure 3.11, it can be found that each boron nitride plate can be cut into three pieces.

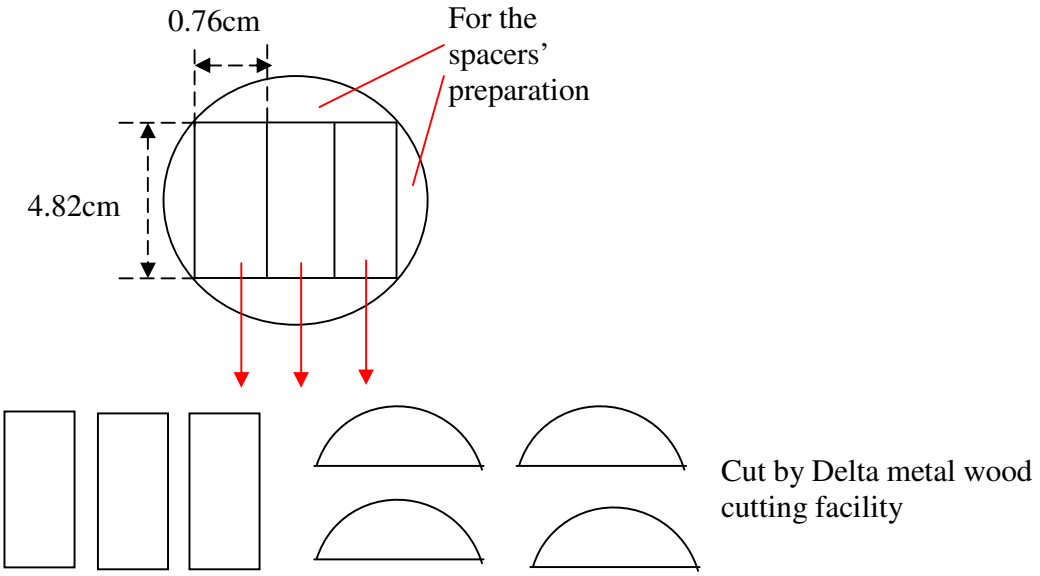


Figure 3.11: Schematic of the BN plate and the BN slices

After cutting, a hole was also drilled on each boron nitride piece for screw fixing in Figure 3.12.

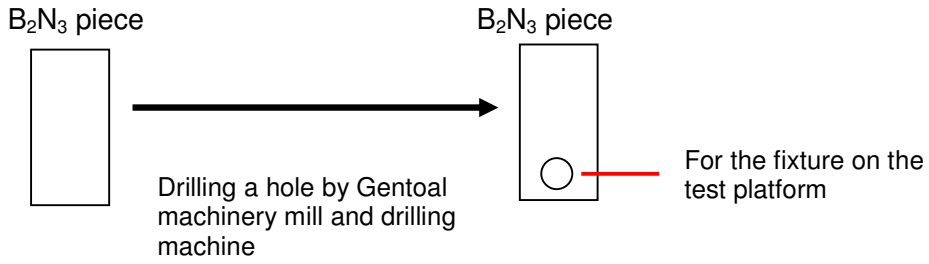


Figure 3.12: Schematic of holes' drilling on B_2N_3 pieces

In order to obtain a better contacting with the cold finger of the cryostat and desirable thickness, boron nitride pieces were polished using sanderpaper.

In Figure 3.13, the BN pieces' edges were polished using silicon carbide sandpaper (1500 grit mirror fine 9"x11" sheets). The spacers were prepared using the same sandpaper, and the spacer's thickness was about 0.07cm.

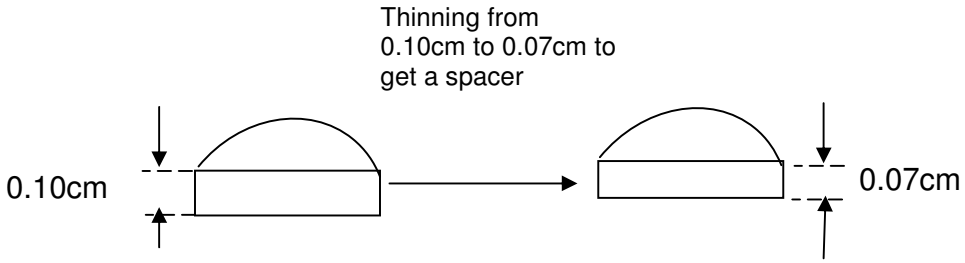


Figure 3.13: Schematic for spacer's preparation

- **Binding the copper bars on the BN pieces**

Binding materials: Quick set Epoxy (Resin + Harder), sets in 4-6 mins

Copper bar size: 0.03x0.03x1.6 (cm)

A special method is used to bind the parallel copper bars with a 1000 μm gap. In this method, a 1000 μm wide boron nitride spacer was used, which was prepared using the above steps.

The binding procedure is shown in Figure 3.14.

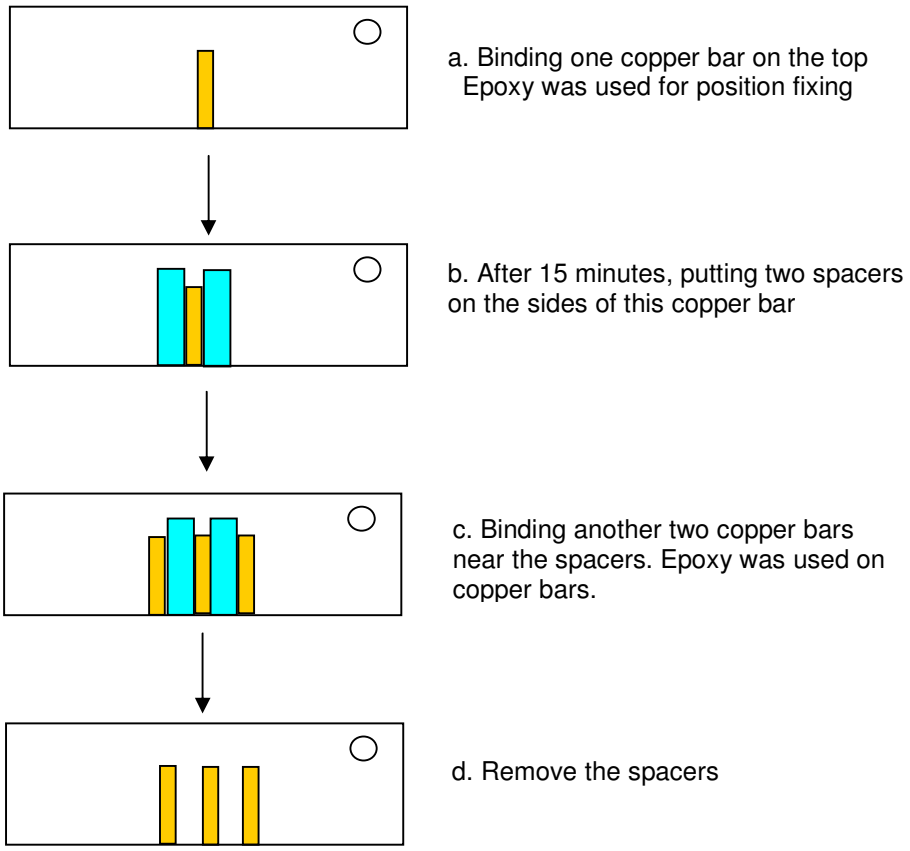


Figure 3.14: Schematic of the copper bars binding

- **Soldering the wires on the copper bars**

As shown in Figure 3.15, nickel wires were soldered on the copper bars using PbSn soldering.

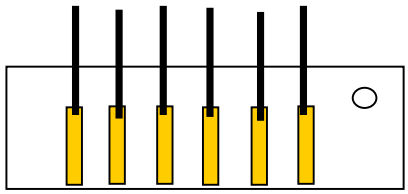


Figure 3.15: Schematic of wire soldering

- **Mount base cleaning (Ozone cleaning and plasma cleaning)**

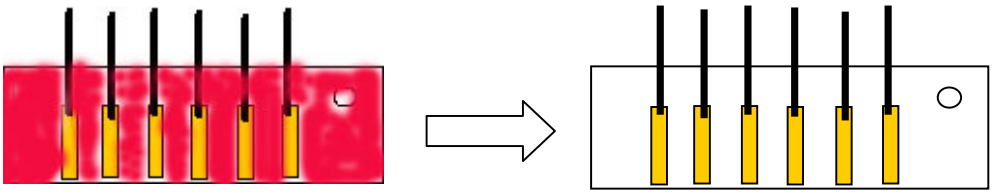
After soldering, the base heat sink for laser mounting is ready for metal depositions. Ozone cleaning and plasma cleaning were applied before metal depositions.

Ozone cleaning was applied before plasma cleaning to remove surface organic chemicals. The mount assembly was disposed in a glass tube of Ozone Generator (PCI OZONE CORP) with a constant flow of ozone percent ranging from 75% to 100% for an hour.

Ar-ion plasma cleaning was applied on the mount assembly to further clean non-organic surface chemicals. The cleaning process was performed for 600 seconds with a current of 200 mA and a voltage of -1200 V with the pressure inside the jar chamber of a Hummer 10.2 sputtering system (Anatech Ltd) maintained at 20 mTorr during cleaning.

- **Metal deposition (Au and Ni layer deposition)**

To obtain a good metal deposition, two masking methods were tested on the same mount assembly. One method is to use a positive photoresist for masking as shown in Figure 3.16. A positive photoresist (Shipley, Microposit AZ 1350 J) will be painted on the surface area which is not supposed to be deposited. After the deposition, the photoresist was removed using an acetone solution.



The area which does not need metal deposition were painted by the photoresist

After metal deposition, the photoresist were removed by the acetone solution

Figure 3.16: Schematic to paint the photoresist

Another method is to place a copper mask on the top of the whole stack. Both methods were tested, and the results indicate that an improved deposition can be achieved by the photoresist masking method.

Following the designed deposition structure shown in Figure 3.17, a gold layer was deposited on the copper bars of the laser mount base assembly with a thickness around 1200 Å using a 1.5 ~ 2.0 Å/s deposition rate next, a 32000 Å thick indium layer was deposited using a 3.0 ~ 4.0 Å/s deposition rate in the same bell jar, and finally a 2200 Å thick gold layer was deposited using a 1.5 ~ 2.0 Å/s deposition rate which served as the anti-oxidation layer. Layers and sizes of the final stack are shown in Figure 3.17.

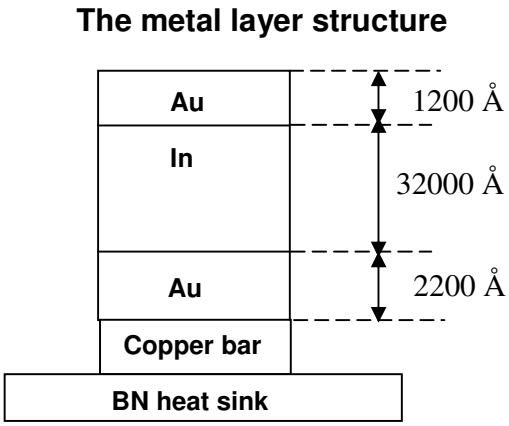


Figure 3.17: Schematic of wire soldering

- **Bonding the laser mount assembly and the quantum cascade laser stripe**

The laser stack was put on the copper bars of the laser mount assembly with the matched position between the copper bars and the laser stripes. After the laser stripe was placed on top of boron nitride heat sink, 120 - 150 ℃ heating using a hot plate was applied to accelerate the Au-In bonding and form a new alloy layer. At this point, the whole packaging procedure was completed and was ready for testing the current-voltage curve.

3.2.3 Results of the first packaged laser stack

Both the current – voltage (I-V) curve and Fourier Transform Infrared Spectroscopy (FTIR) were tested on the packaged quantum cascade laser stack by epi-side down method.

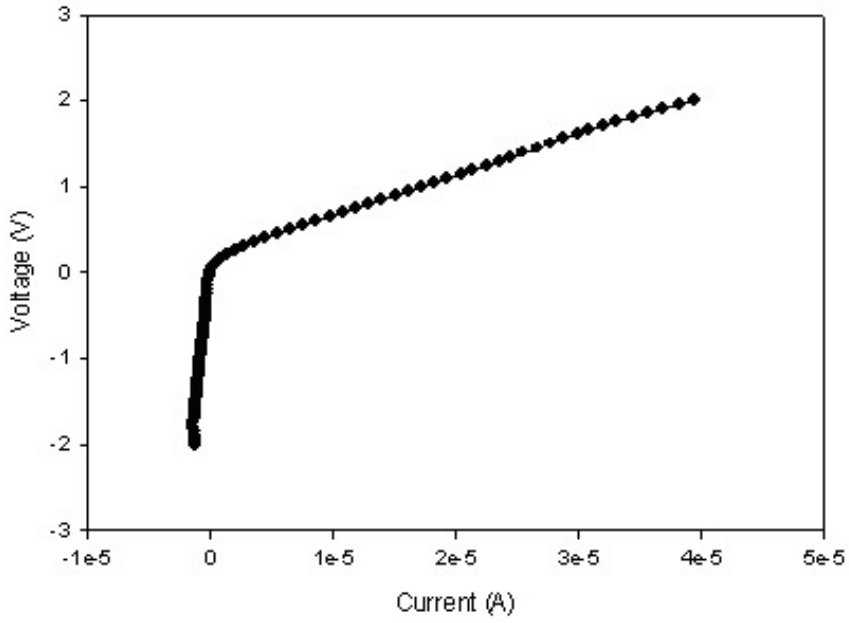


Figure 3.18: Current versus voltage for an epi-side down packaged quantum cascade laser

The current-voltage curve in Figure 3.18 shows the packaged laser has a good electrical contact. The exponential relation of the applied current and the measured voltage indicates the properties of the electron transition among quantum well in the quantum cascade laser.

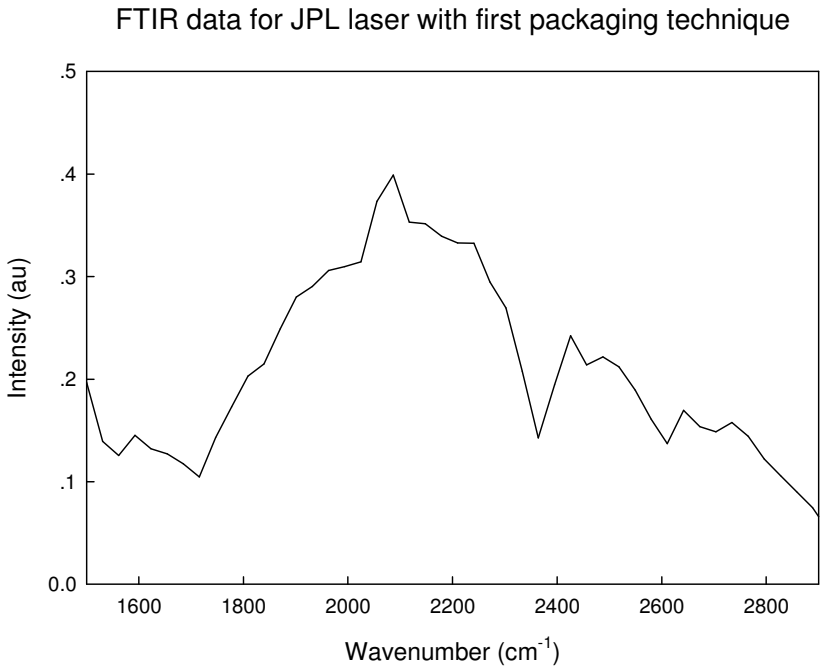


Figure 3.19: FTIR data for a packaged quantum cascade laser

FTIR data in Figure 3.19 shows the whole packaged quantum cascade laser #J435 has a broad emission peak, and the emission peak wavelength is not as intense as would be expected from a mid-IR laser. The designed emission wavelength is in the range of 2700 - 3333 cm^{-1} instead of 2100 cm^{-1}. It is possibly due to damaged laser facets or damaged quantum cascade structures prior to packaging.

3.3 Second packaged laser with the boron nitride heat sink and a special mechanical part design by epi-side down method

The second packaging technique used a boron nitride bar as the heat sink combined with a special mechanical design. In this packaging technique, the laser was placed on the top of a boron nitride based assembly by a boron nitride wall and screwed into place with a spring.

3.3.1 Packaging procedure

The Boron nitride base heat sink was prepared using the same procedure as that in first packaging method.

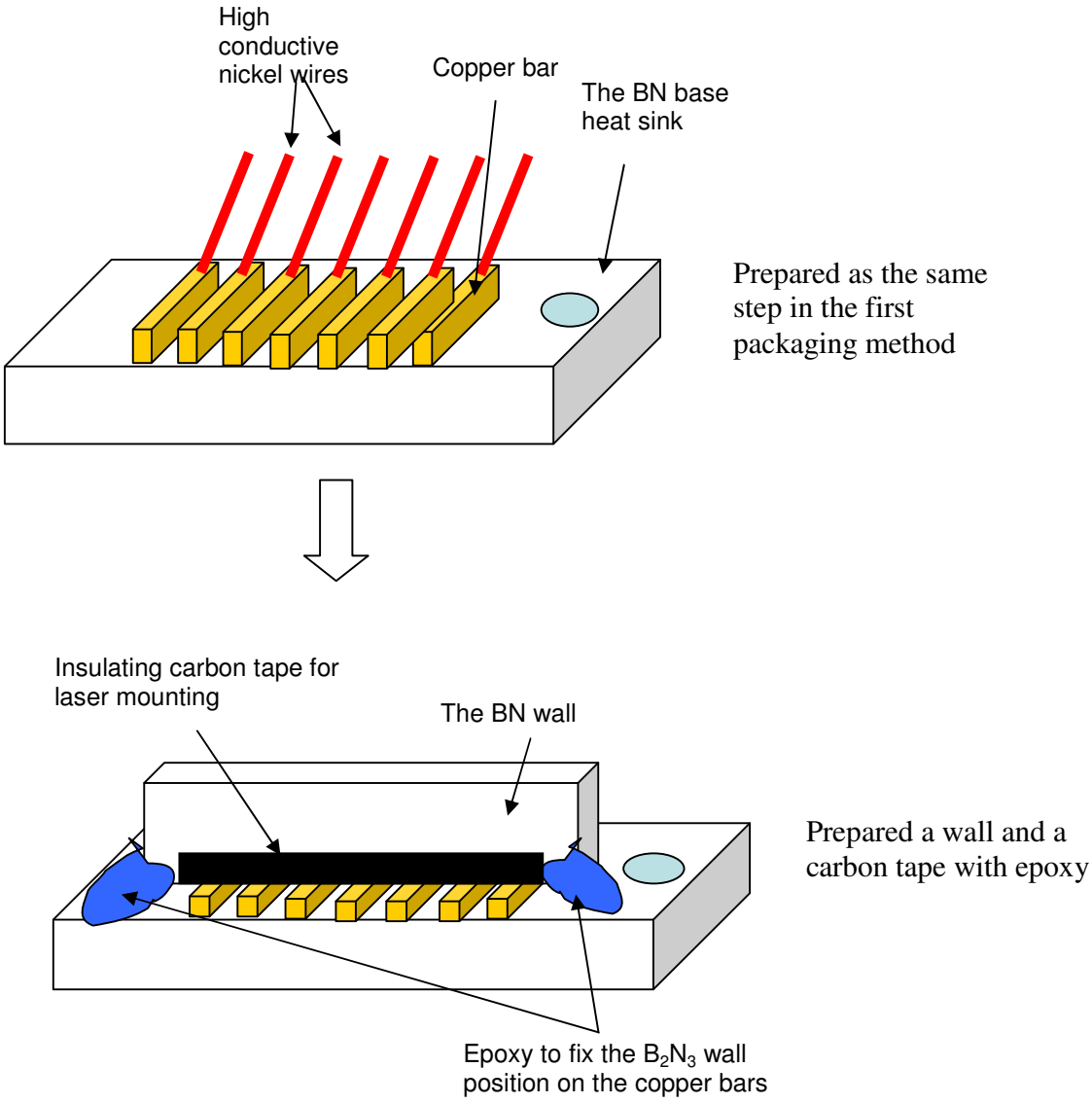


Figure 3.20: Schematic of a special mechanical wall design for second packaging method

A boron nitride wall and a carbon tape were used on the boron nitride heat sink as

shown in Figure 3.20.

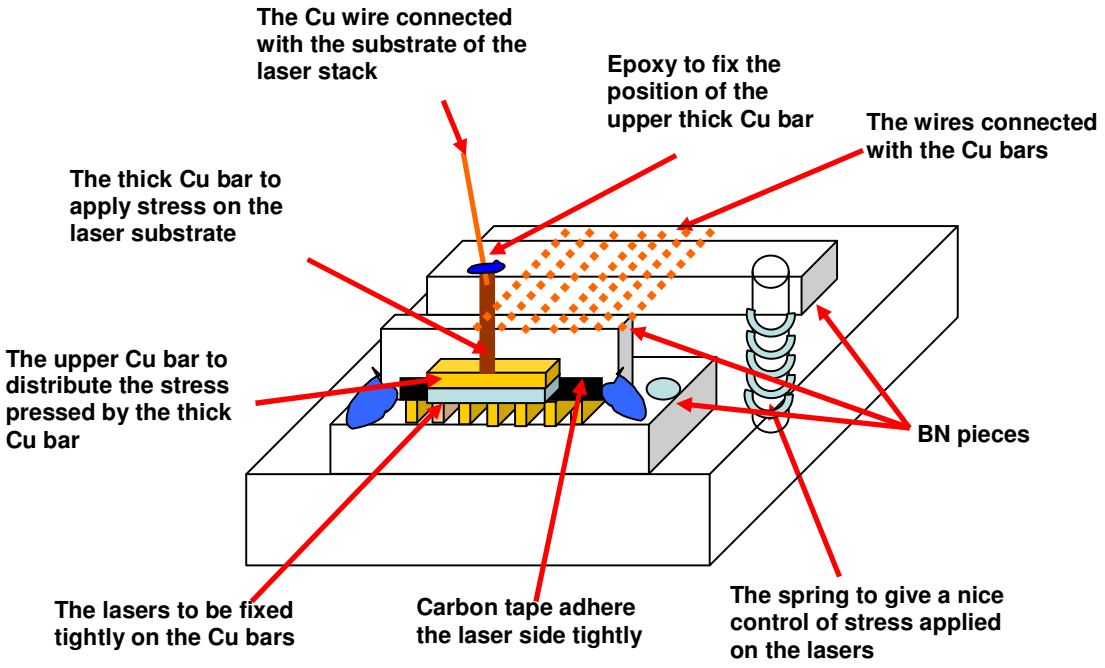


Figure 3.21: Final stack of a special mechanic wall design for second packaging method

The final package is shown in Figure 3.21. The quantum laser stack was fixed in the center of the boron nitride heat sink, which was screwed on the cryostat copper cold finger. A thick copper bar attached on the upper copper bar which was placed on laser stripe surface (See Figure 3.21). Both the quantum cascade laser stack and the upper copper bar were adhered on carbon tape which was placed on a BN wall. BN wall was fixed on the heat sink by epoxy.

3.3.2 Results discussion of second packaging method

Since both the thick copper bar and the upper copper bar were just contacted by touching, conducting currents can improve contacting between Cu-Au and Cu-Cu

materials. The basic idea is to check the resistance is: the bonding between Au-Cu and Cu-Cu contacts improves after each time current is applied using a DC power supply. So the resistance decreases after each resistance check as verified using a multi-meter. However the measured resistance value will be saturated and no longer decrease.

Figure 3.22 shows the testing procedure and results.

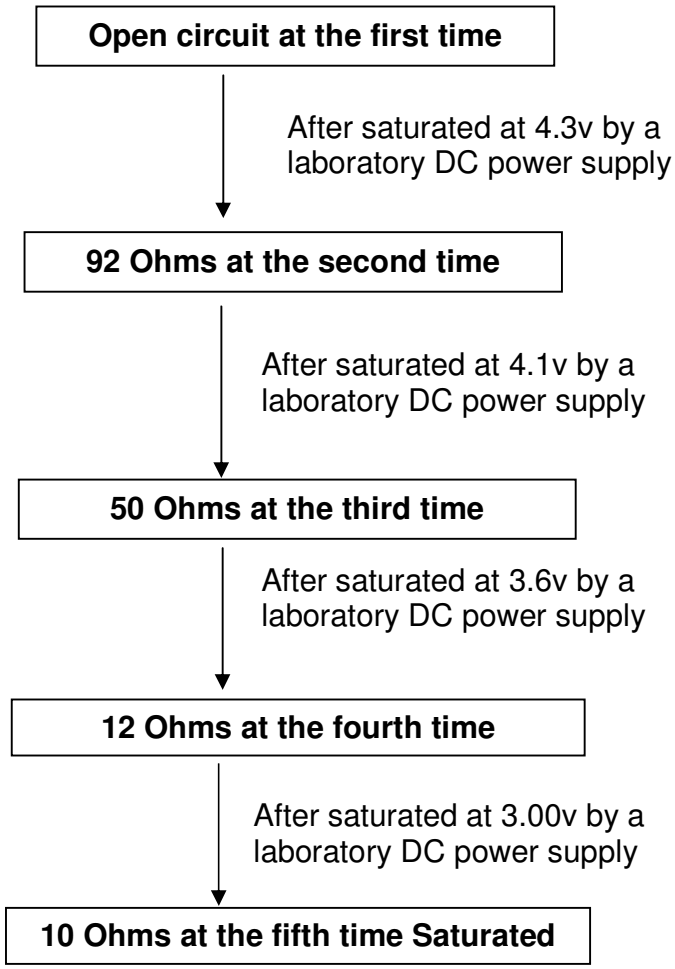


Figure 3.22: Each applied current on packaged laser stack caused decreased resistance and finally saturated to a certain value

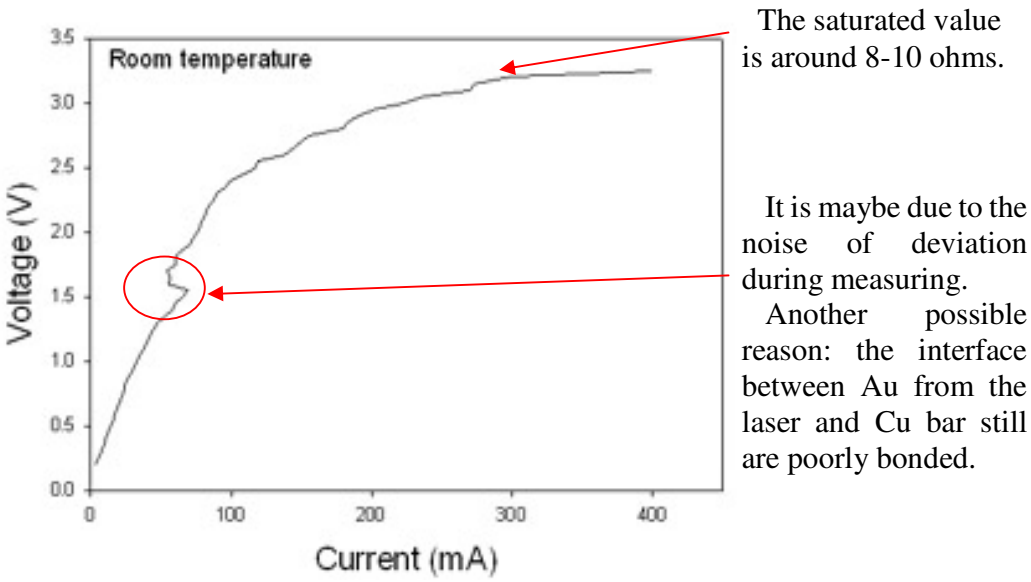


Figure 3.23: I-V curve for second packaging method

The current-voltage (I-V) curve of this packaging technique is shown in Figure 3.23. The twist in Figure 3.23 is probably due to the deviations in measurement noise or a poor bonded contact interface between the Au contact and Cu bar.

Compared with the I-V curve from the first packaged laser, the curve in Figure 3.23 is a little rough. It is probably due to poor contact quality between copper bars which is not as good as the Au-In alloy bonding. However, this method is less time consuming and easy to replace laser stacks.

3.4 Third packaged laser with the copper heat sink and gold wire bonding by epi-side up method

The third packaging technique is to use a copper bar as the heat sink with the gold wire bonding technique. Yang and coworkers also used a similar packaging method. Figure 3.24 is a picture of the laser packaging from Yang's group.

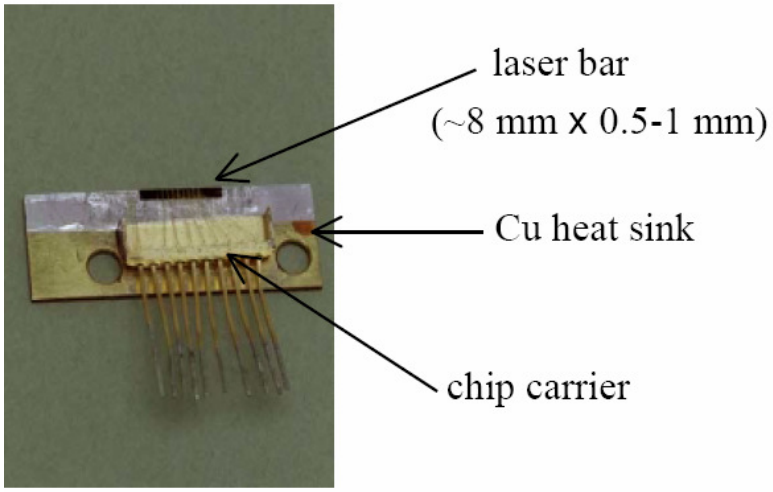


Figure 3.24: Picture of the laser packaging from Dr. Rui Yang's at JPL [58]

A one cent coin was placed near the laser stack as a reference for size. The laser was packaged on the top of the copper heat sink with silver paint. A special carrier was designed to support the laser positive connection wires.

A similar packaging method was designed in our lab. In this packaging method, a copper heat sink was prepared first, and screw holes were drilled on the copper heat sink. Next, the laser was attached on the edge of the copper heat sink by silver paint. High conductive nickel wires were soldered on the copper bars for the positive connection, which were adhered on the thermal interface adhesive pad (ADI-ALO-119-135) and the other side of thermal interface adhesive pad was attached on copper heat sink base.

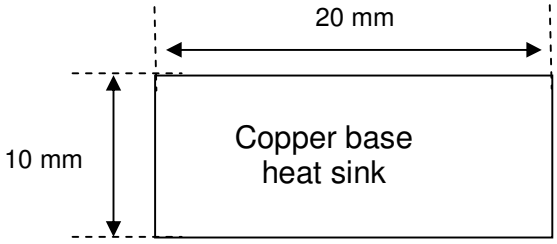


Figure 3.25: Schematic of copper base heat sink size

Schematic of this packaging assembly is shown in Figure 3.25. A copper base heat sink was cut according to the designed size, and the surface and edges were polished. Nickel wires were soldered on the copper bars as the way shown in Figure 3.26.

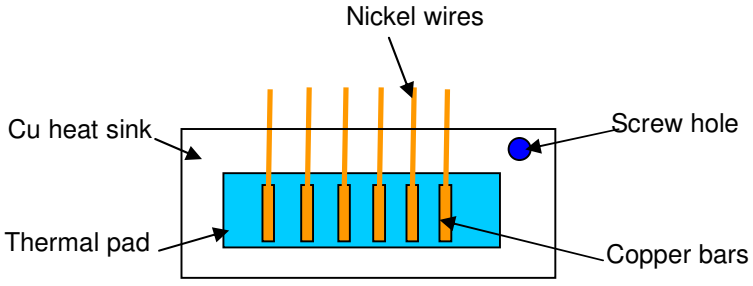


Figure 3.26: Schematic of nickel wire soldering

Silver paint was placed on the edge of the copper heat sink as shown in Figure 3.27.

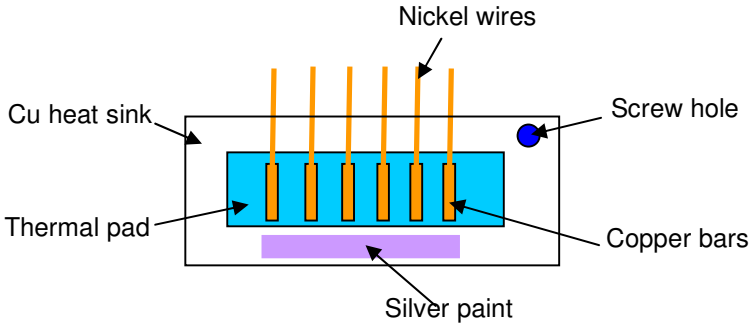


Figure 3.27: Schematic to put silver paint on the edge of Cu heat sink

In Figure 3.28, gold wire bonding between the gold contacts of laser stripe and copper bars was completed using a K&S Model 4124 ball bonder.

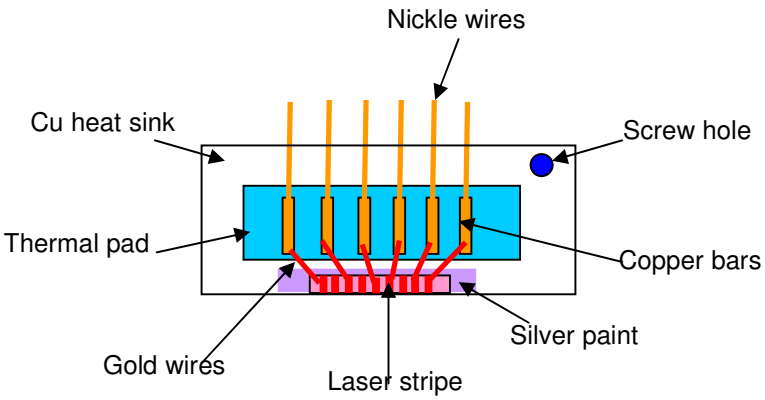


Figure 3.28: Schematic of gold wire bonding

Figure 3.29 is a picture of the laser stack with a copper heat sink by an epi-side up method. It is hard to solder gold wires onto copper bars, so silver paint was used to connect the gold wires onto copper bar surface, also shown in Figure 3.29.

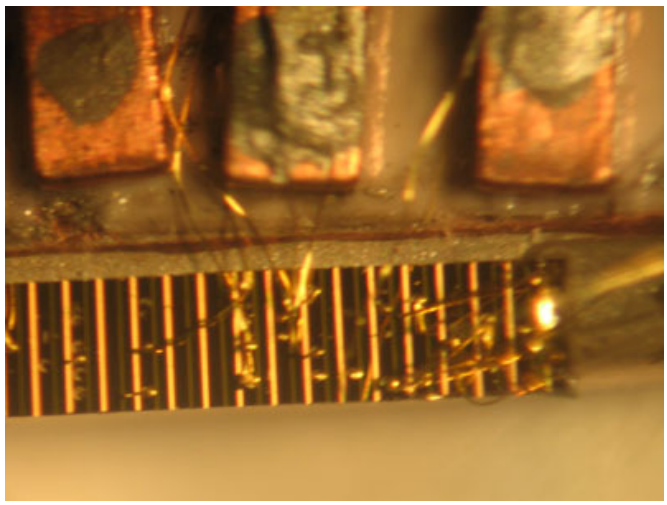


Figure 3.29: Picture of a packaged laser stack with a copper heat sink

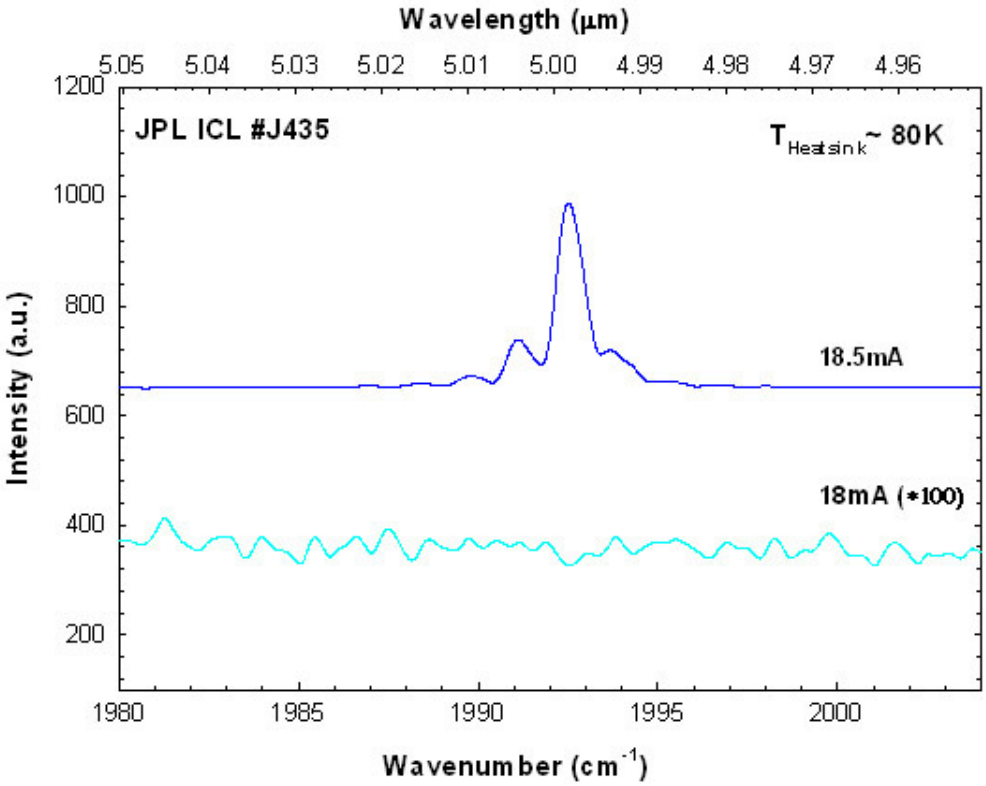


Figure 3.30: Threshold emission at low currents for a quantum cascade laser

Figure 3.30 indicates the threshold current for the quantum cascade laser is around 18.5 mA. Multi mode emissions were observed from the JPL ICL #J435 as shown in Figure 3.31. The intensity is relatively high for a desirable mounted quantum cascade laser. The number of emission modes is increasing with increasing injection current.

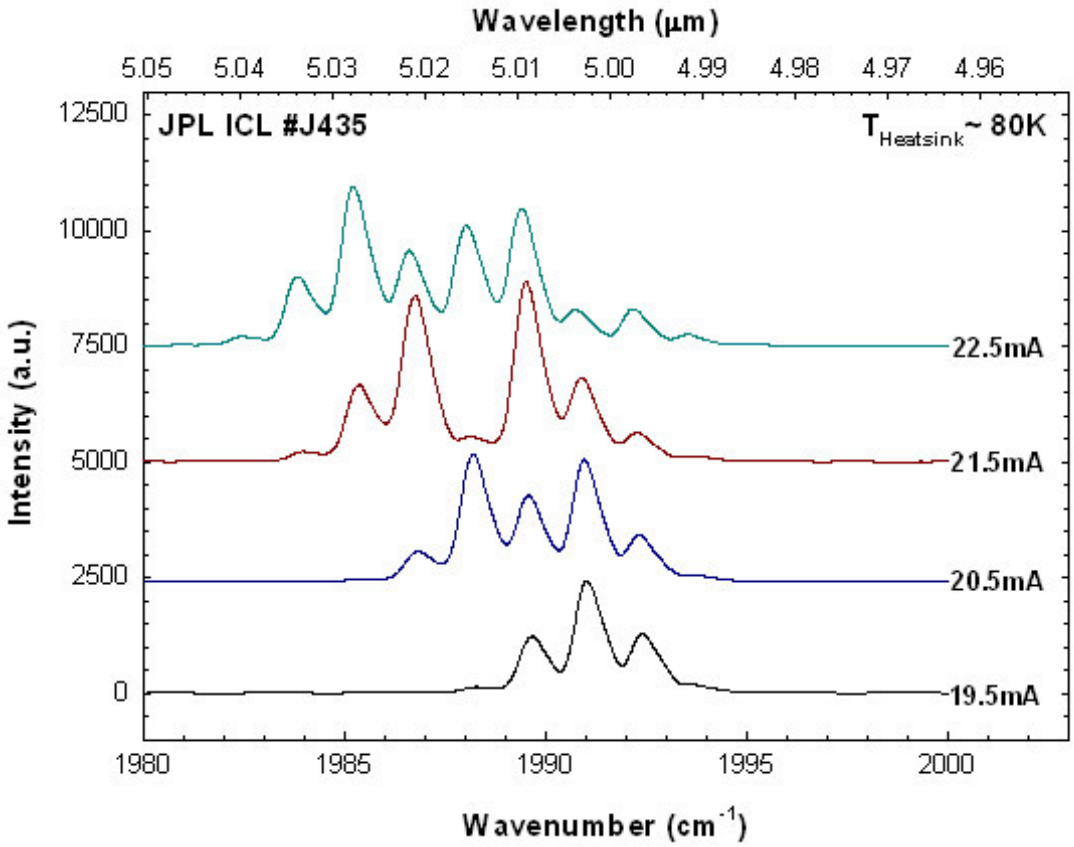


Figure 3.31: Multi mode emission from a quantum cascade laser

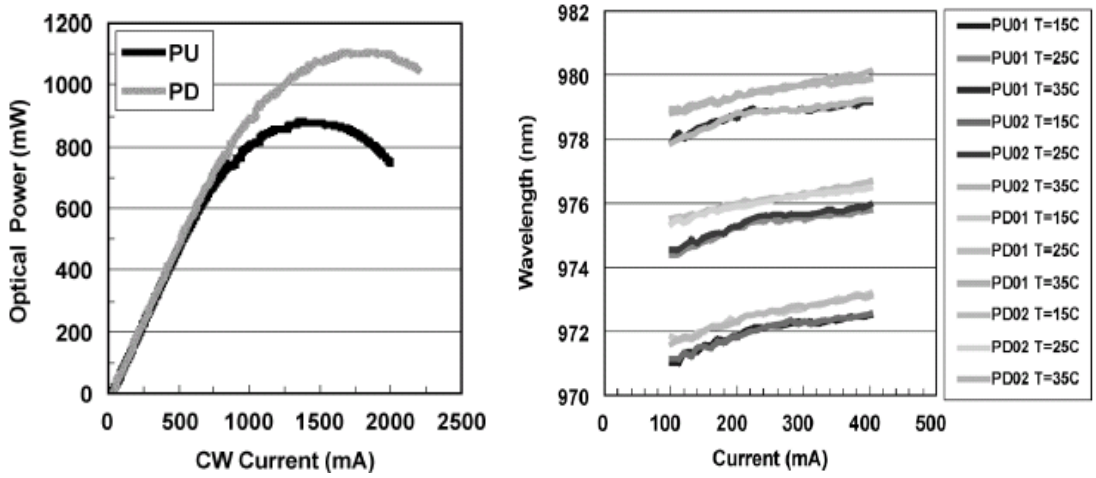
3.5 Comparison of different packaging techniques

Table 3.1 presents a comparison of current versus voltage and FTIR testing results of different packaging techniques.

Table 3 1: Comparison of different packaging techniques

	Features of packaged techniques	I-V curve	FTIR results
First packaged laser with boron nitride heat sink and Au-In metal bonding by epi-side down method	Attached the active region of the laser onto its BN heat sink by some metal bonding to obtain a better heat dissipation	Desirable current versus voltage curve with quantum effects	Poor emission and improper emission wavelength as designed due to some damage in quantum cascade laser before packaging.
Second packaged laser with the boron nitride heat sink and a special mechanical part design by epi-side down method	Using a BN heat sink Easy to package the laser and low cost	Contact condition between Au-Cu and Cu-Cu improved after each turn of applied current	No emission observed
Third packaged laser with the copper heat sink and gold wire bonding by epi-side up method	Use gold wire bonding and silver paint to packaged the laser onto the copper heat sink	Desirable current versus voltage curve with quantum effects	Desirable emission and proper emission wavelength as designed

Due to the limited availability of lasers for packaging experiments, FTIR data were obtained only from the epi-side down packaging method with limited improvement in heat dissipation. However, some groups did get desirable improvements in heat dissipation and higher emission power using the epi-down method [52].



(a) Optical power versus current (b) Wavelength versus current

Figure 3.32: Comparison for epi-up and epi-down bonded laser submounts [53]

Figure 32 (a) is a comparison of "optical power versus current" for epi-up (PU) and epi-down (PD) bonded 980-nm single-mode lasers. After 1000 mA, due to better heat dissipation, the laser based on an epi-side down method had 20% more emission power than the laser based on an epi-side up method does. Figure 32 (b) shows that the epi-side down packaged laser had a longer emission wavelength than epi-side up packaged laser.

In summary, epi-side down is a new design for laser packaging. Since the epitaxial active region is connected directly to the heat sink, the packaged laser will have better heat dissipation, and will lower the laser emission threshold while improving operating reliability. Therefore, the epi-side down packaging is a promising way to improve laser performance in comparison to other laser packaging techniques.

Chapter 4

Interband cascade lasers and its application in gas detection

4.1 Introduction

The recent progress in developing distributed feedback (DFB) interband cascade lasers (ICLs), which are also called type II quantum cascade lasers, has made possible single mode emission with wavelengths between 3.0 μm and 4.5 μm, a spectral region which covers many gas absorption lines of interest. [53,54 ,55]

Similar to diode lasers, interband quantum cascade lasers have transitions between the conduction band and the valence band. However, instead of losing electrons from the conduction band to the valence band gap as is the case for diode lasers, the electrons tunnel into the conduction band of the next cascade stage. Since the conduction and valence bands have opposite dispersion curvatures, auger recombination is severely suppressed in interband cascade lasers and this results in a low threshold current for lasing. Continuous wave (CW) operation of interband cascade lasers is presently achieved at cryogenic temperatures. From theoretical analysis by R.Yang and coworkers [53], there are no theoretical limitations preventing near-room temperature operation for interband cascade lasers. Pulsed operation of an interband quantum cascade laser has been demonstrated at a wavelength of 3.51 μm at room temperature. For continuous wave operation, a threshold

current density of 13.2 A/cm^2 and power efficiency of 17% have been measured from the same interband cascade laser at 80 K [56].

Infrared laser spectroscopy is a customized system to measure accurately narrow absorption lines in the near-infrared (1.3 μm - 1.8 μm) or mid-infrared spectral region (3.0 μm – 5.0 μm). Gas molecules absorb energy at specific wavelengths, providing a unique characteristic for that species. The process is highly selective such that there is no absorption if the lasing wavelength is off center from the absorption lines. By tuning the laser's beam wavelength to the desired gas absorption line and by the precise measurement of the absorption level of that beam, it is possible to determine the concentration of the gas. Figure 4.1 depicts a laser beam passing through a gas cell and a portion of the laser power absorbed by molecular species in the gas cell.

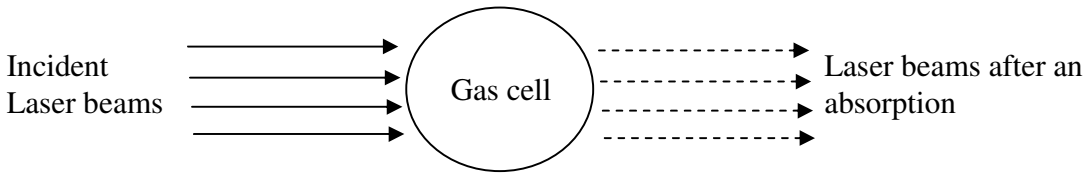


Figure 4.1: Schematic of laser beam absorption by a gas cell

Absorption spectroscopy is based on the Beer-Lambert law, which states that transmission will decay exponentially as exp(-S*g(f)*N*L) where S is the absorption line strength, g(f) is the line shape function, N is the concentration of absorbing gas molecules, and L is the optical path length. For sufficiently low pressures (a few bar), many gases have distinct absorption lines. In the gas detection application area, most gases of industrial interest have fundamental absorption is in the mid-infrared region (MIR).

The absorbed power can be calculated by multiplying the constant K, number of molecules, the cross section and the optical path length. By measuring the amount of power absorbed at a characteristic wavelength, molecular concentrations can be determined based on the absorption cross section and the optical path length. Normally the cross section in the mid-infrared is much larger than that in the near-infrared, so mid-infrared lasers offer better sensitivity for gas detection. By a specially designed optical cell technique called "cavity ring down", an optical path length of more than 10 km can be achieved in a physical space at less than one meter. Due to high emission power, very low operating current and good wavelength tunability in mid-infrared region, quantum-cascade (QC) semiconductor lasers can provide future applications in optical diagnostics and spectroscopy.

4.2 Testing equipment

Equipment used in the experiments described in this chapter are: vacuum pumps, a temperature controller, cryostats and Fourier Transform Infrared (FTIR) Spectrometer.

4.2.1 Pumps for vacuum cryostats

Pumps used in the experiments include a mechanical pump and a liquid nitrogen sorption pump.

A small and economical mechanical pumping station is desirable for evacuating small and medium sized volumes to pressures of approximately 1 mTorr. A 0.5 horsepower Franklin Electric mechanic pump is used for evacuating cryostats. The whole mechanic pumping station is supplied with a five foot flexible stainless steel pumping line,

an isolation valve, a vent valve and a compound pressure/vacuum gauge.

An oil free working environment is suggested for some optoelectronic devices in a cryostat. In this case, a homemade sorption pump equipped with Huntington EV-150 valves is used. The pumping station consists of two stages: a roughing pumping (1 torr to 0.01 torr or better) and high vacuum pumping (0.001 torr or higher). Both of the roughing pump and the high vacuum pump use liquid nitrogen for the oil free cryopumping.

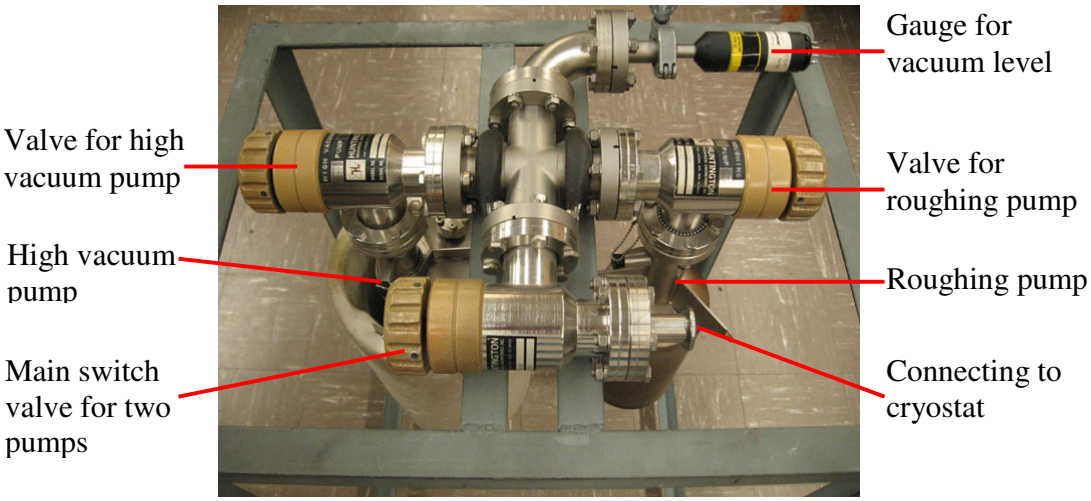


Figure 4.2: Top view of a Huntington EV-150 pumping station

Figure 4.2 is a top view of the valve assembly for the sorption pumping station.

4.2.2 Temperature controller

The Lakeshore 330 temperature controller is a microprocessor based instrument with digital control of a variable current output. It can obtain a stable cryostat temperature from 81 K to 120 K by controlling the operating current of a thermal tape in the liquid nitrogen cooled cryostat. A silicon diode temperature sensor is with the Lakeshore 330 temperature controller.



Figure 4.3: Front view of a Lakeshore 330 temperature controller

Figure 4.3 is the front view of a Lakeshore 330 temperature controller. The key part for this controller is the thermal resistor or tape in the cryostat.

4.2.3 Cryostats used in experiments

Two types of liquid nitrogen cryostats were used in electrical and optical characterization of quantum cascade lasers.

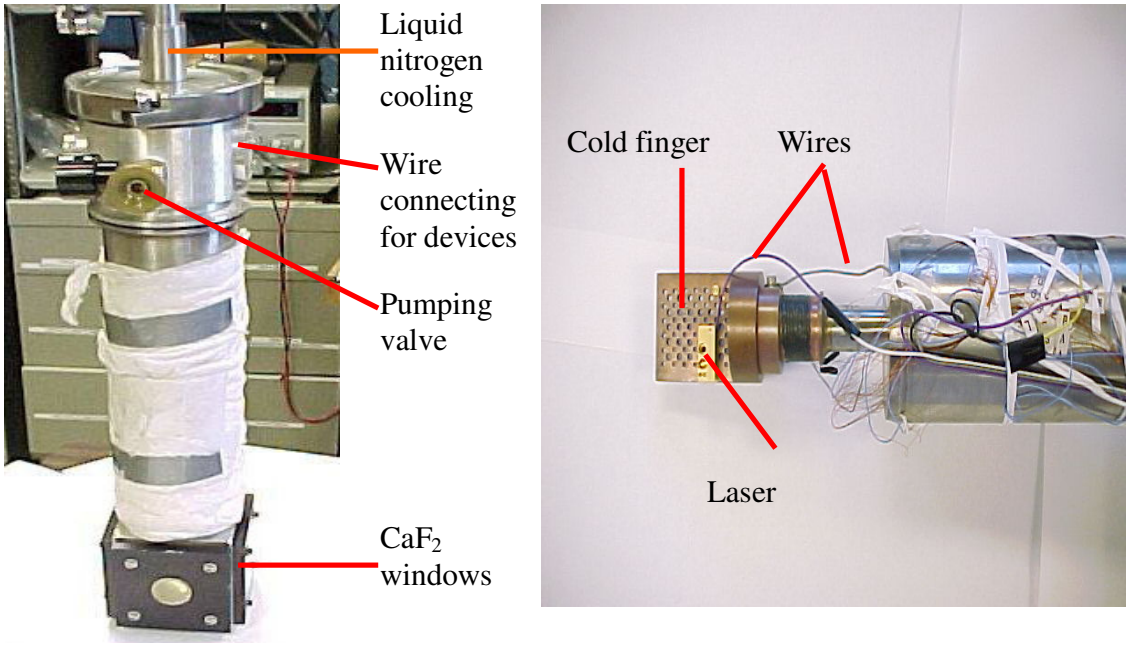


Figure 4.4: Pictures of a Janis cryostat:
(a) outside view of the cryostat (b) cold finger inside the cryostat

Figure 4.4(a) is a picture of a cryostat from Janis company, and Figure 4.4(b) is the inside view of this cryostat. A pressure of 10^{-3} torr can be obtained by a mechanical or liquid nitrogen sorption pump. A temperature sensor and the laser is mounted on the cold finger of the cryostat. Despite a liquid nitrogen boiling temperature of 77 K, the lowest temperature achievable with this cryostat is around 82 K. Limited by the heat resistor power, the highest programmable temperature will be around 90 K. When a metal rod is dipped in liquid nitrogen to control its evaporation, 90 K up to 110 K programmable temperature could be achieved.

Another cryostat (Laser Photonics) was used for characterizing the interband

quantum cascade laser #J435 see Figure 4.5. It can tune the cold finger in a wider temperature range, compared with Janis cryostat. From the testing results, the highest programmable temperature could reach 120 K under liquid nitrogen cooling, while the lowest programmable temperature was 81 K. It was equipped with an IR transparent window (CaF_2) behind which the laser was mounted.

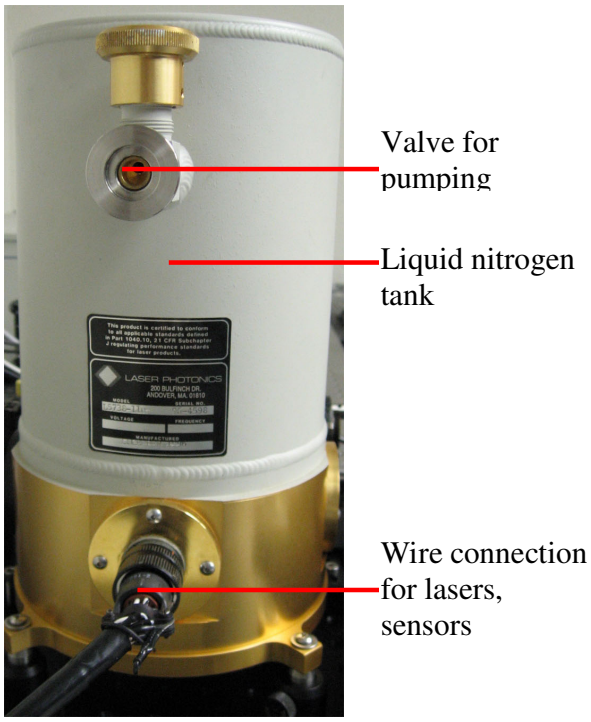


Figure 4.5: Picture of Laser Photonics cryostat

4.2.4 Fourier Transform Infrared (FTIR) Spectrometer

A Fourier Transform Infrared (FTIR) spectrometer is a measurement technique to obtain infrared spectra by collecting an interferogram of a sample signal with an interferometer to measure all infrared frequencies simultaneously. The introduction of computers allows digitizing the data, performs the Fourier Transform function, and outputs the spectrum in the frequency domain.

There are several methods to measure the temporal coherence of the light, including the continuous wave Fourier transform spectrometer and the step scan Fourier transform spectrograph. Oriel instruments MIR 8000 FTIR is used in the experiments described here. Components of a complete MIR 8000™ Spectrometer are listed as follows: [57]

- Source or sample
- MIR 8000™ Scanner
- Beam Splitter and Windows
- Detection System
- Data Acquisition package

Different than traditional FTIR instrument, by interchanging or adding components as needed, the system can be customized to satisfy some specific applications.

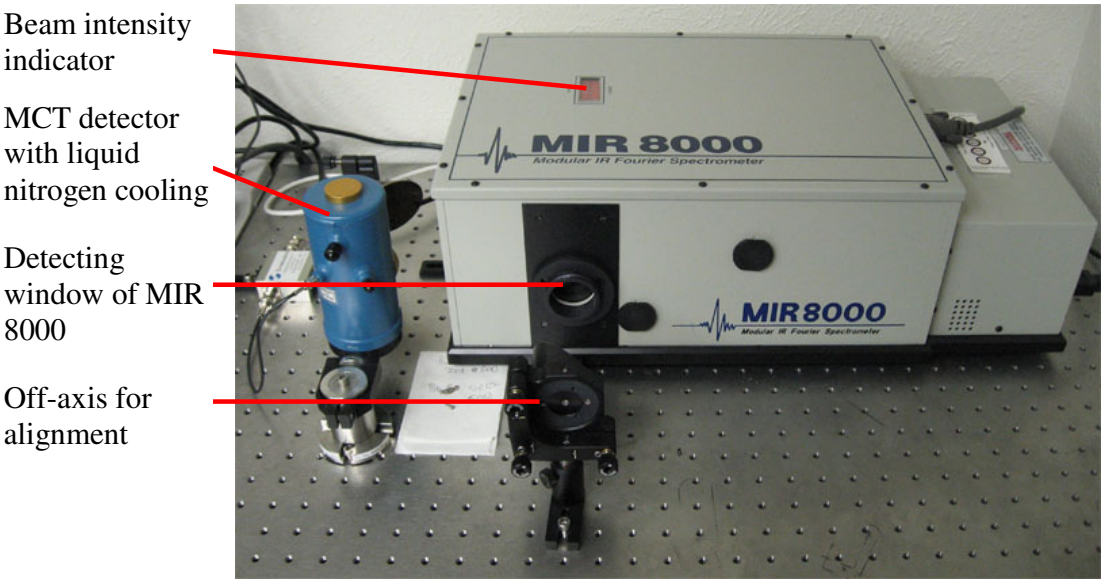


Figure 4.6: Picture of a MIR 8000 FTIR system

Figure 4.6 is a side view of a MIR 8000 FTIR system. Major features of MIR 8000 FTIR system are listed as follows:

- Wide spectral coverage: 14,000 to 909 cm^{-1} (700 nm to 11 μm)
- High resolution: up to 0.5 cm^{-1} (0.02 nm at 700 nm and 0.04 μm at 11 μm)
- Liquid nitrogen cooled photovoltaic HgCdTe detector (11 μm wavelength cut off, Fermionics #PV-11-1) and its preamplifier (Fermionics #PVA-500-5)
- Two OAPMs are used in the system. One is used to focus the incident beam, and the other is used to transmit the beam from FTIR to the HgCdTe detector

4.3 Electrical behavior of quantum cascade lasers

Typically, interband cascade quantum cascade lasers exhibit current-voltage (I-V) curves that have diode like characteristics for emission wavelengths around 5μm. A desirable quantum cascade laser should have the exponential relation between the applied

current and measured voltage due to the electron transitions in the quantum well.

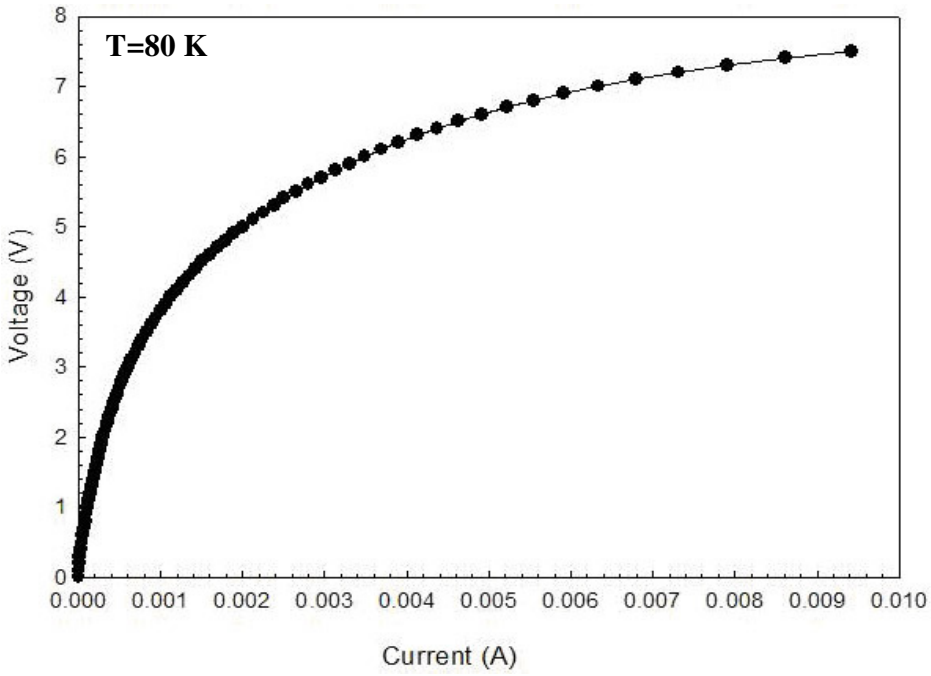


Figure 4.7: Current versus voltage for JPL interband cascade laser

In Figure 4.7, it is clearly shown that the current increases exponentially with the increasing voltage. The estimated differential resistance will decreases to the several ohms level when the applied current reaches the threshold condition of the laser. Since the maximum pumping current of Agilent 4156A is 10 mA, the testing current is just from 0 mA to 10 mA.

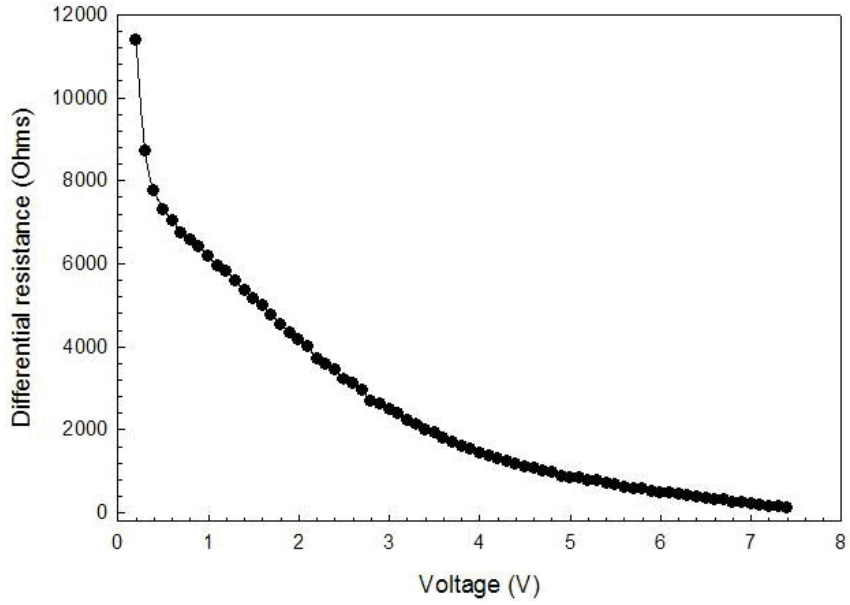


Figure 4.8: Differential resistance versus voltage for a JPL interband cascade laser

Figure 4.8 is differential resistance value versus voltage curve, which is derived from the current-voltage curve obtained at a laser operating temperature of 80 K in Figure 4.7. It can be noticed that with increasing applied voltage, the differential resistance of the laser drops from 12,000 ohms to several hundred ohms. The exponential relation is commonly observed in other quantum cascade lasers as well, and it is due to increased electron tunneling current through the quantum well structure. If the applied current of Agilent 4156A can go beyond 10 mA in testing, the measured differential resistance should reach several ohms level.

4.4 Optical behavior of quantum cascade lasers

Figure 4.9 depicts a two stage quantum cascade structure in which lasing happens between level 4 and level 3, and non-radiative transitions (electron tunneling) occur among other states.

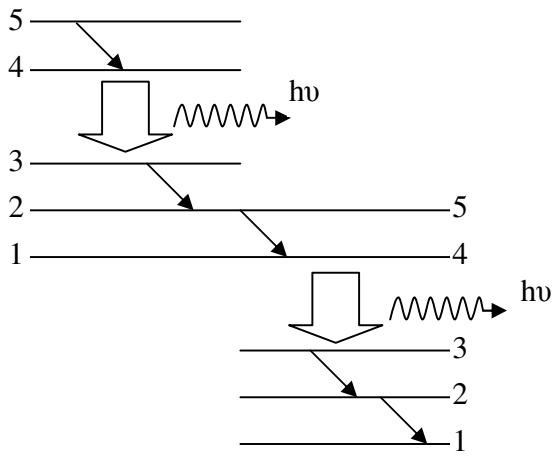


Figure 4.9: Schematic of electron transition in a two stage cascade laser

In actual cases an interband or intraband quantum cascade laser is composed of twenty or thirty such stages. The main characteristic for an interband quantum cascade laser is low threshold current and high emission intensity.

4.4.1 Threshold current and emission modes of interband cascade lasers

The threshold current of the interband cascade laser #J435 from Jet Propulsion Laboratory was tested by a MIR 8000 FTIR system with the electrical pumping method.

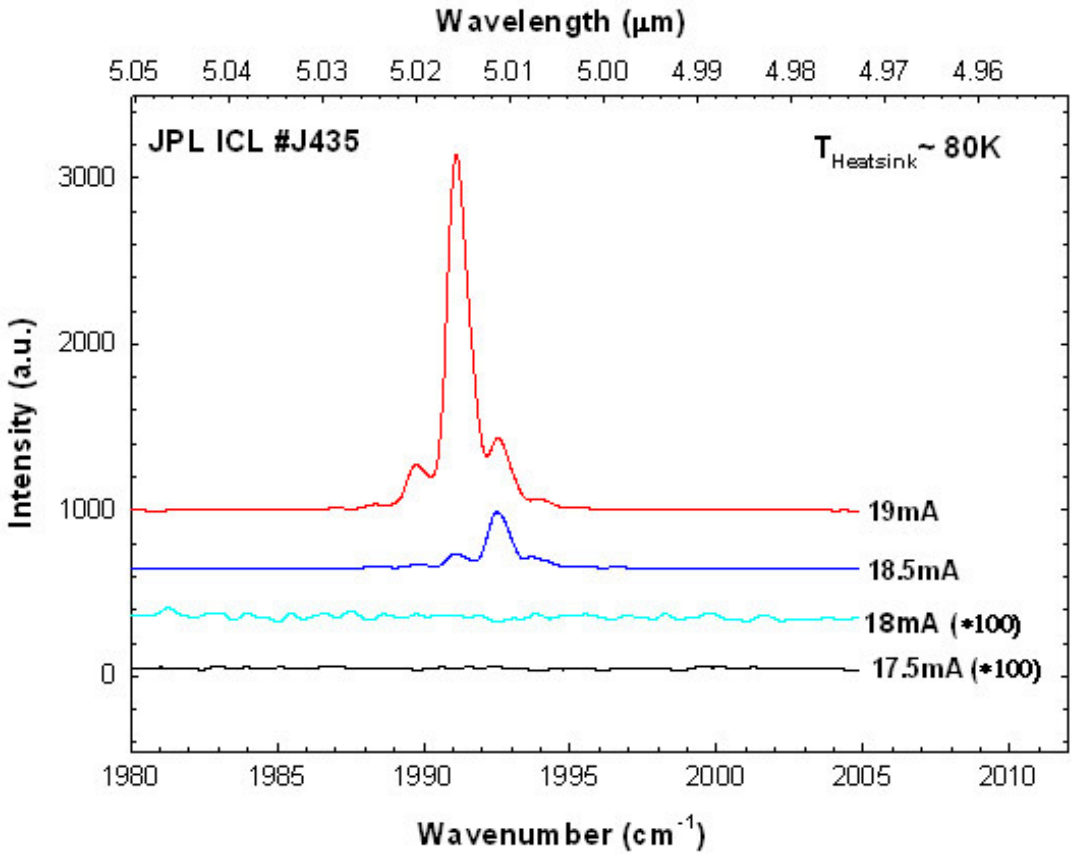


Figure 4.10: Threshold current check for JPL interband cascade laser #J435

Figure 4.10 is the tested FTIR curve for the threshold current checking of the interband cascade laser #J435. It is clear that the threshold current of interband cascade laser #J435 is 18.5 mA at 80 K. With the cryostat temperature higher than 80K, the threshold current will be higher than 18.5 mA due in part to more phonon scatterings occurred at higher temperature.

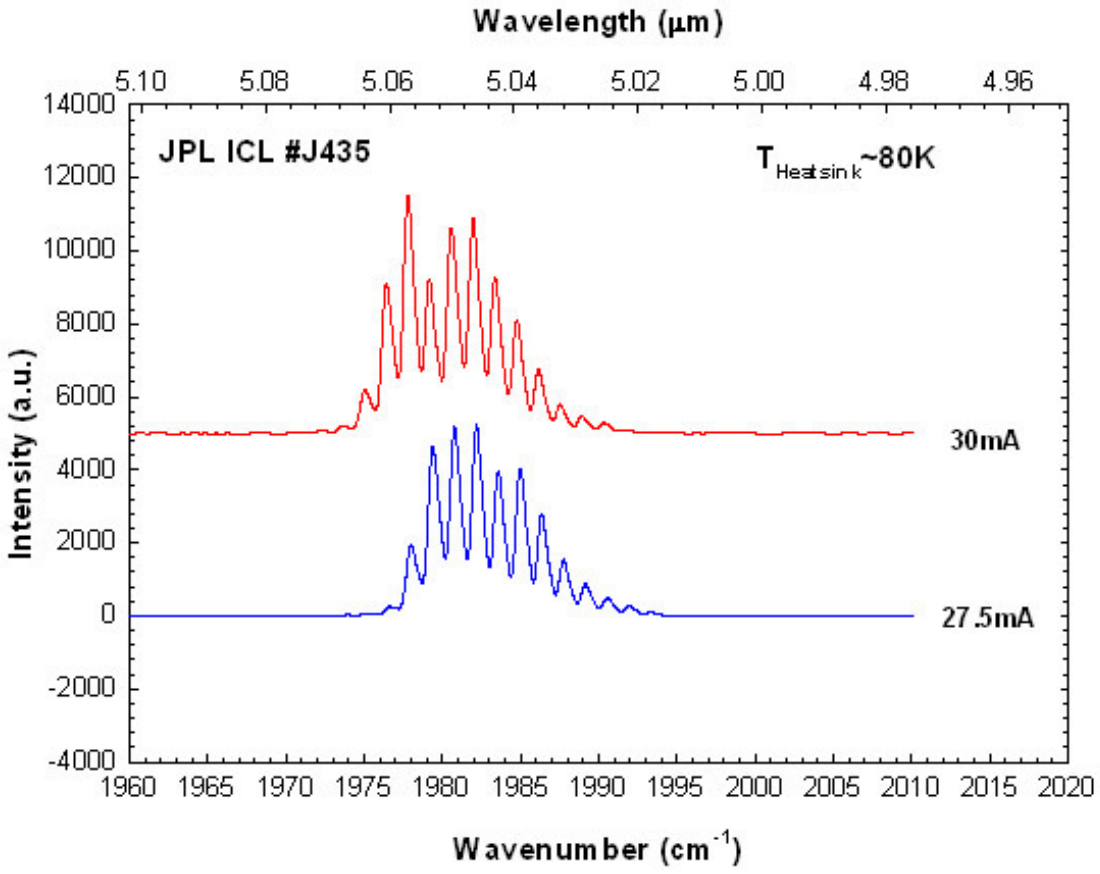


Figure 4.11: Multi mode emission for JPL interband cascade laser #J435

Multimode emission is observed for the JPL interband cascade laser #J435. Figure 4.11 shows FTIR spectra for the interband cascade laser at different pumping currents. The number of emission modes of the laser is 11 at 27.5 mA and 12 at 28 mA. Since #J435 is Fabry-Perot cavity laser, multi mode emission is observed. A DFB structure would make it single mode.

4.4.2 Tuning techniques for interband cascade lasers

For some JPL interband quantum cascade lasers with 3 μm emission wavelength, the capability of current tuning is much less than that of temperature tuning.

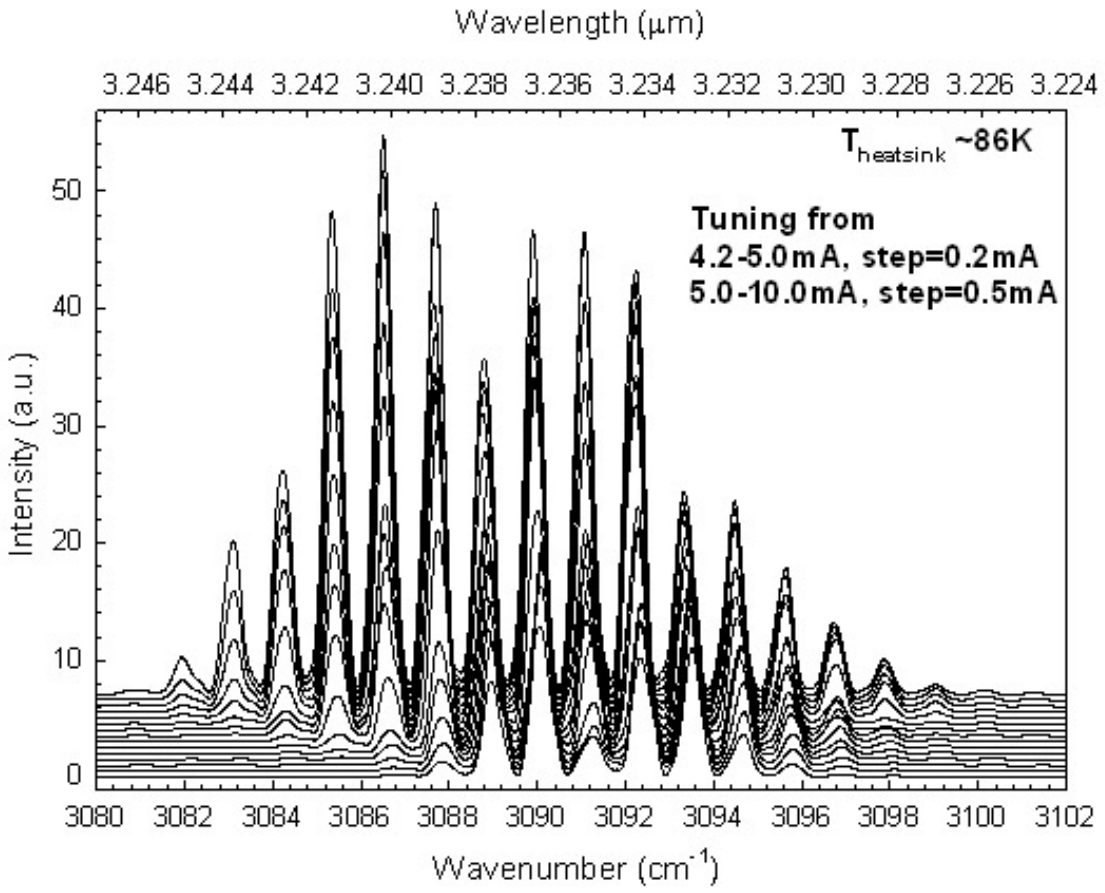


Figure 4.12: Current tuning profile for JPL interband cascade laser #J653

Figure 4.12 is the current tuning profile of interband quantum cascade laser #J653 at 86K. The current tuning rate of the laser is less than 0.1 cm^{-1}/ mA. Compared with the intensity of laser #J435, the intensity of laser #J653 emission is low because of the gain factor in FTIR was set at "1" and injection current is below 10 mA. For FTIR testing of laser #J435 emission, the gain factor in FTIR is set at "64" and injection current is at above 27 mA.

In contrast to poor current tuning, capability of temperature tuning is much higher. Figure 4.13 is the temperature tuning profile of interband cascade laser #J653. The

temperature tunable rate for JPL #J653 is around 0.94 cm^{-1}/ K, and the laser operating temperature is from 91K to 107K. However, for JPL quantum cascade lasers with 5μm emission wavelength, the current tuning capability is higher.

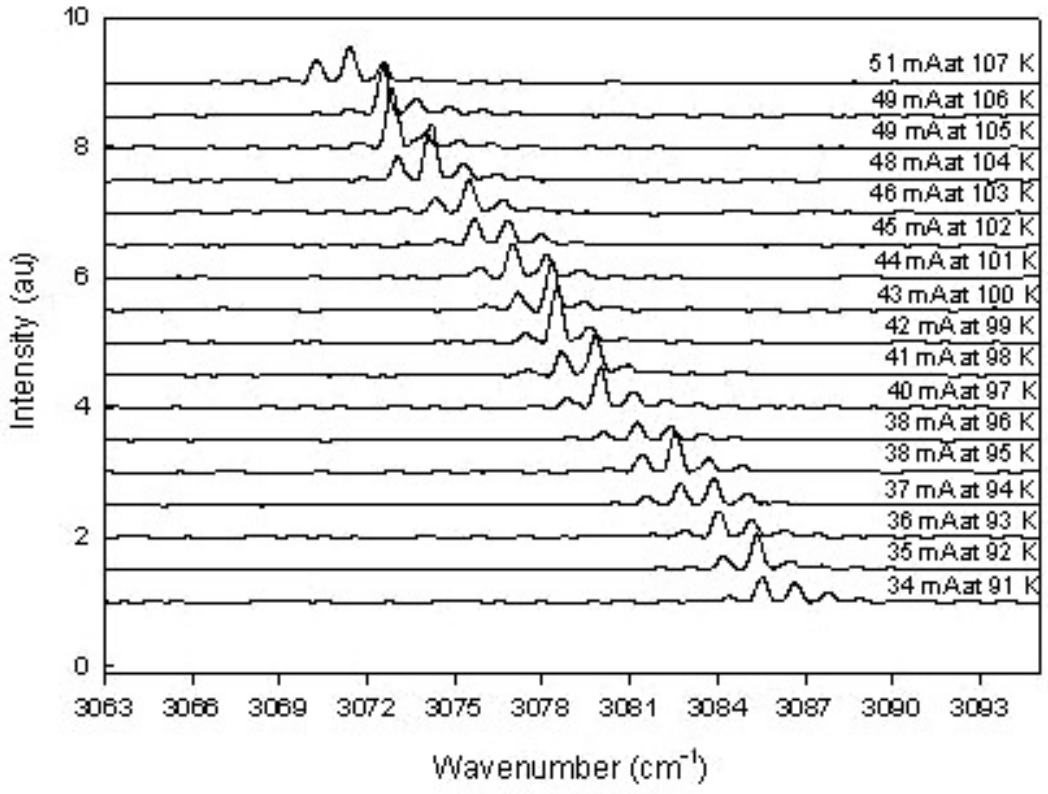


Figure 4.13: Temperature tuning profile for JPL interband cascade laser #J653

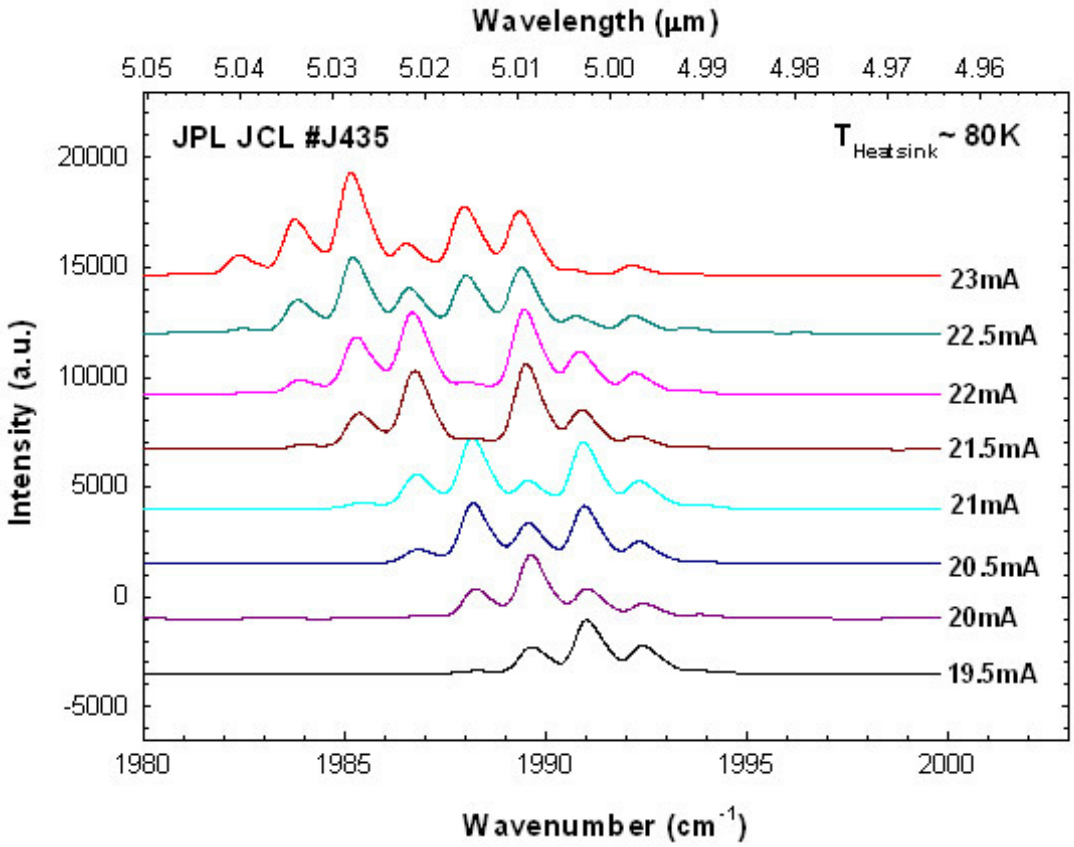


Figure 4.14: Current tuning profile (19.5 to 23mA) for JPL interband cascade laser #J435

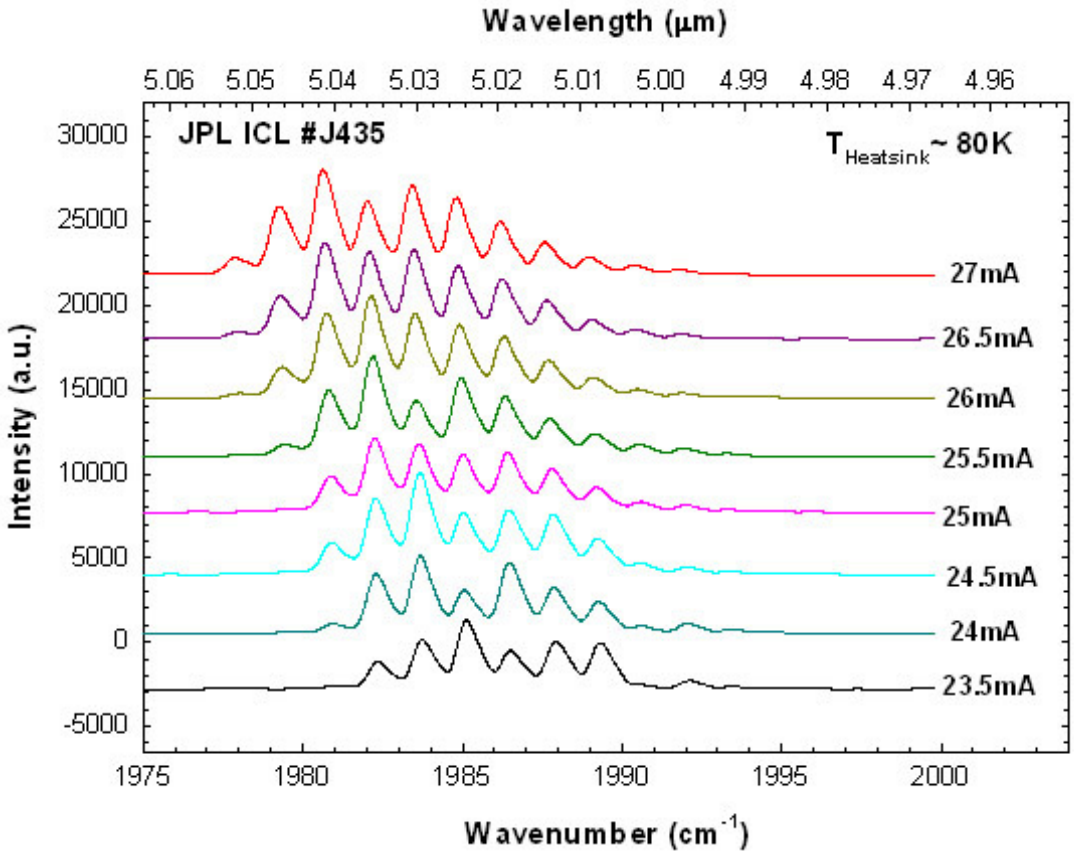


Figure 4.15: Current tuning profile (23.5 to 27mA) for JPL interband cascade laser #J435

Figure 4.14 (19.5 to 23mA) and Figure 4.15 (23.5 to 27mA) show measured emission spectra at different currents for interband cascade laser #J435. In Figure 4.14 and Figure 4.15, it can be seen that the current tuning rate for the JPL #J435 laser is around 1.2 cm^{-1}/ mA for a laser operating temperature of 80K.

All the tuning results of JPL interband cascade lasers are summarized in Table 4.1. Both #J435 and #J653 are mid-infrared quantum cascade lasers. Their tuning capability differs in current tuning profile. Laser #J435 with 5 μm emission wavelength has a current tuning capability with 1.20 cm^{-1}/K rate, whereas laser #J653 with 3 μm emission

wavelength has a relatively poor current tuning rate 0.1 cm^{-1}/ mA. For temperature tuning capability, both of lasers has a desirable tuning rate which is about 1.0 cm^{-1}/K.

Table 4.1: Comparison of tuning capability of JPL ICL #J435 and #J653

Laser ID	Wavelength	Current tuning rate	Temperature tuning rate
#J435	5μm	1.20 cm^{-1}/mA	1.05 cm^{-1}/K Calculated From [58]
#J653	3μm	less than 0.1 cm^{-1}/ mA	0.94 cm^{-1}/K

Injection current tuning for ICL #J653 at 86 K was observed to be 0.10 cm^{-1}/ mA, while the tuning rate for ICL #J435 at 80 K was 1.2 cm^{-1}/ mA. This difference may be caused by different sized mesa stripes. ICL #J653 has a mesa width of 15 μm and a cavity length of 1.5 mm, while ICL #J435 has a mesa width of 150 μm and a cavity length of 1 mm. A smaller current tuning rate is consistent with less active region heating, and ICL #J653 with its thinner mesa width will have more effective active region heat dissipation due to better lateral heat flow normal to the laser cavity. By contrast, ICL #J435 with its much larger mesa area will experience more heating with increasing current thus giving a larger current tuning rate.

4.5 Theoretical analysis of gas detection by JPL #J653

Tunable, single frequency, mid-IR diode lasers are potentially suitable for highly sensitive trace gas detection for applications in pollution, toxic gas, disease diagnosis and industrial process monitoring. These mid-IR lasers operate in the fingerprint region of molecular absorption. For example, the detection sensitivity of methane at 3.26 μm is 1.7 parts-per-billion (ppb), whereas the shorter wavelength of 1.65 μm is 600 ppb.

In this section, a new detection mechanism will be introduced to take advantage of JPL laser #J653. Instead of single wavelength laser, a multimode laser is proposed for gas detection. Similar to finding emission wavelengths that are matched with a specific absorption peak of methane, one, two, three wavelengths simultaneously matched with three absorption peaks of methane and is studied here.

Gas transmission spectra for these matching peaks study are obtained from the publicly available HITRAN database (http://www.hitran.com).

4.5.1 Methane detection by JPL #J653

From methane absorption data in HITRAN database, it is observed that there are six methane absorption peaks between 3060 cm^{-1} and 3120 cm^{-1}. Figure 4.16 shows the six absorption peaks with their corresponding wavenumber.

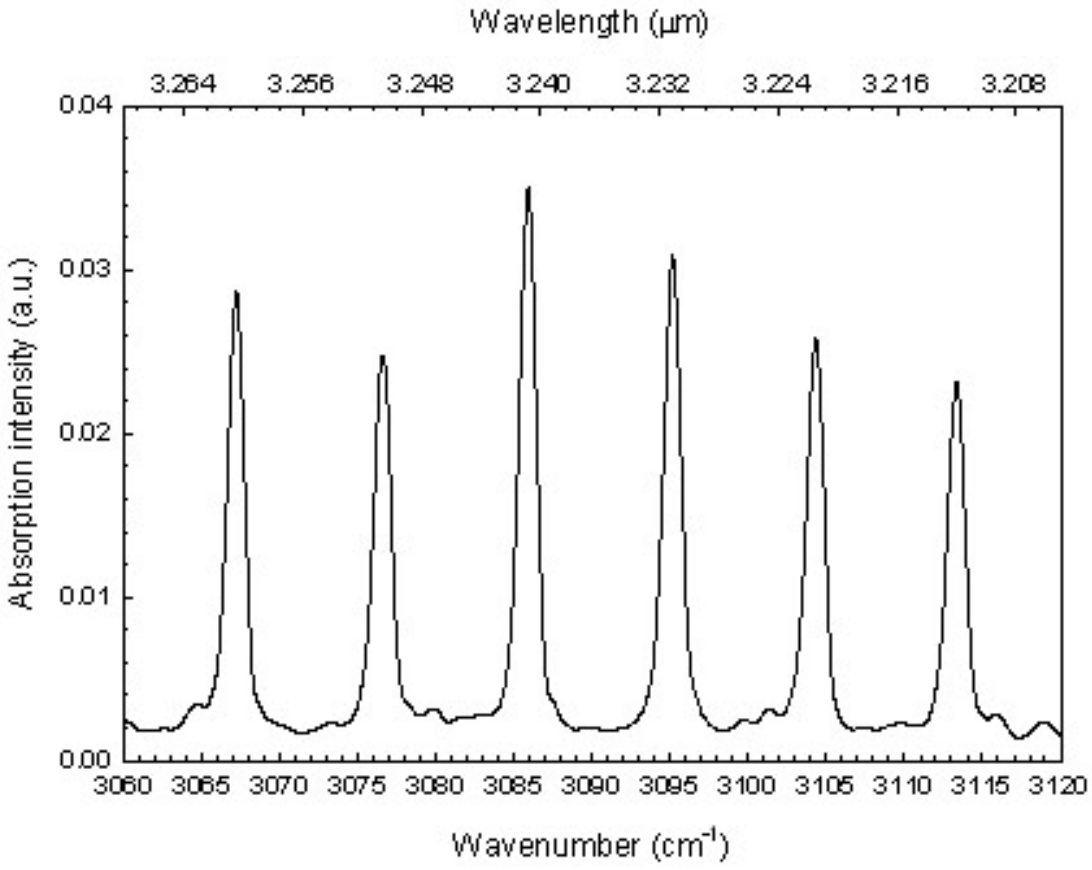


Figure 4.16: Methane absorption peaks from 3060cm^{-1} to 3120cm^{-1} (From HITRAN)

Combined with an emission range from 3080 cm^{-1} to 3120 cm^{-1} for JPL #J653, three matching absorption peaks are confirmed in Figure 4.17. The JPL #J653 condition for matched case is 34 mA at 91 K, 46 mA at 101 K and 60 mA at 112 K. So when operating temperature of JPL #J653 scan from 91K to 112K, three absorption phenomena should be observed. Since continuous scanning could offer absorption peak matching three times, the spectrometer based on JPL ICL #J653 should improve measurement accuracy compared with traditional single characteristic absorption peak match.

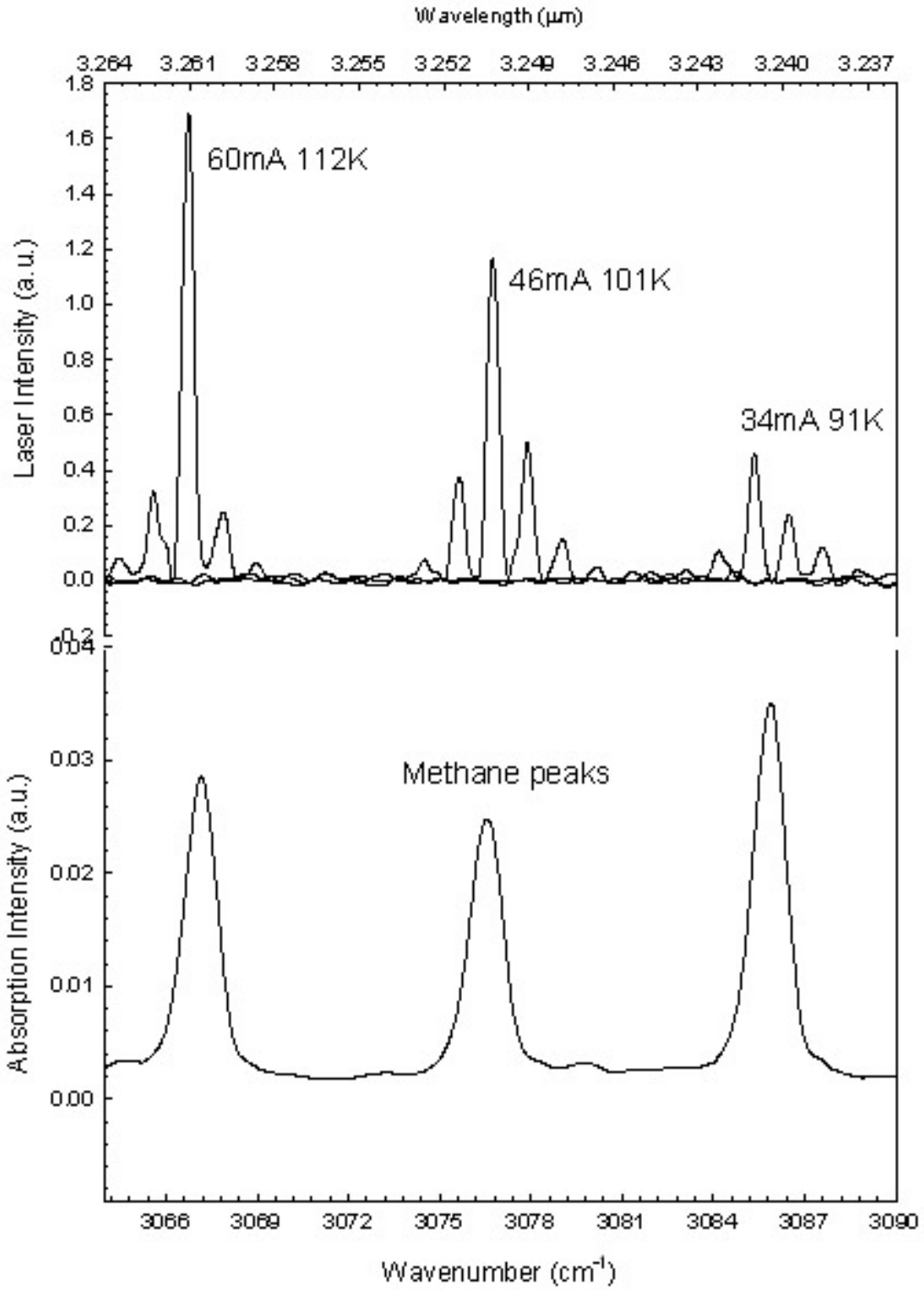


Figure 4.17: Three matched methane absorption peaks with JPL ICL #J653

4.5.2 Toluene detection by JPL #J653

Using JPL #J653 to detect toluene will be based on another methods. Since multimode emissions have quite a number of emission peaks, if the integral intensity of some emission peaks can match a broad molecular absorption band, the spectrometer will be able to detect this specific molecule. The detection mechanism is designed for complex organic molecules since these kinds of molecules will have a relatively broad absorption bands, such as benzene, toluene, or ethylbenzene.

Figure 4.18 is the matched case for toluene molecule, the integral of two emission peaks between 3072 cm^{-1} to 3075 cm^{-1} range will match the absorption peak of toluene around 3073 cm^{-1}.

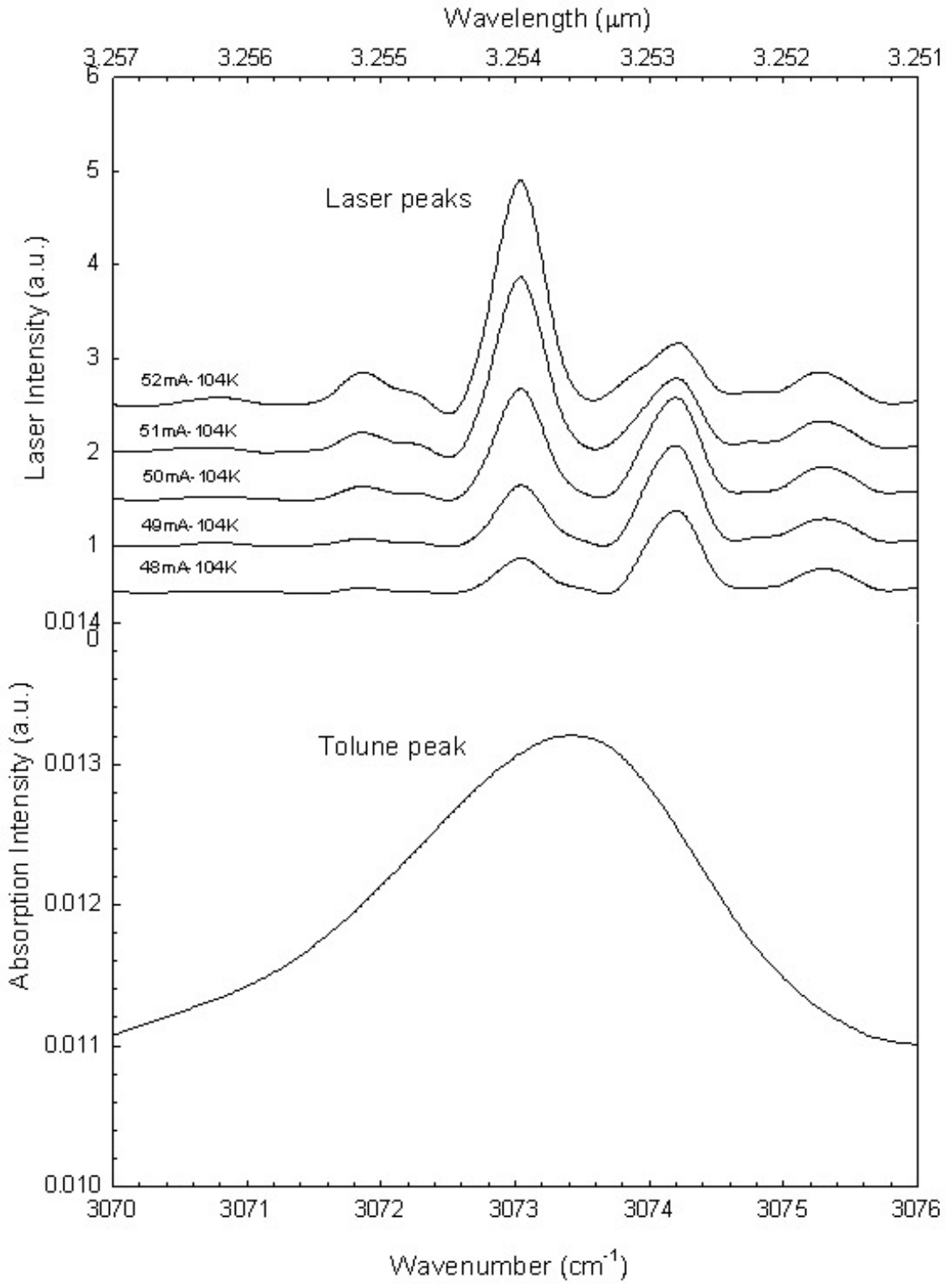


Figure 4.18: Two emission peaks of JPL ICL #J653 with its matched toluene absorption

4.5.3 Conclusion for JPL ICL #J653 applications in gas detection

Even though JPL ICL #J653 is a multimode emission laser, potential application in gas detection still can be studied. Multi absorption peak matching is possible for a multimode laser to scan in some specific temperature range. For complex organic molecules, narrow absorption peak is impossible and a broad absorption peak will be the case for use of the multimode laser in the spectrometer. The results are summarized in Table 4.2.

Table 4.2: Summary of possible detection mechanism for JPL ICL #J653

Gas types	possible detection mechanism	Molecule Example
Low mass gas molecules	Sequence matching during temperature scanning	Methane: possible three times matching from 91K to 112K
High mass organic molecules	Integral matching for a broad absorption peak	Toluene: a broad absorption peak matching around 3073cm^{-1}

4.6 Conclusion

Differential resistance value versus voltage, derived from the current-voltage curve, shows that, with increasing applied voltage, the differential resistance of the laser drops from 12000 ohms to several hundred ohms. The exponential change is commonly observed in other quantum cascade lasers as well and is due to the quantum transitions of electrons among quantum well in the laser.

It can be concluded that the number of laser emission modes increase with increasing pumping current. These modes will be the result of all quantum transitions between states at a certain operating temperature and pumping current.

Poor current tuning profile of interband cascade laser #J653 at 86K is observed. The current tuning rate of the laser is less than 0.1 cm^{-1}/ mA. It is relatively undesirable, compared with 0.94 cm^{-1}/ K temperature tuning for the same laser. So the main tuning technique for this type of quantum cascade laser will be realized by temperature tuning or external cavity tuning. In contrast to poor current tuning capability of laser #J653, the current tuning rate of JPL #J435 is around 1.2 cm^{-1}/ mA, at a laser operating temperature of 80 K. Calculated from the laser data sheet provided by JPL, temperature tuning capability of #J435 is also comparable to its current tuning capability, which is about 1.05 cm^{-1}/ K. This difference may be caused by different sized mesa stripes. ICL #J653 has a mesa width of 15 μm and a cavity length of 1.5 mm, while ICL #J435 has a mesa width of 150 μm and a cavity length of 1 mm. A smaller current tuning rate is consistent with less active region heating, and ICL #J653 with its thinner mesa width will have more effective active region heat dissipation due to better lateral heat flow normal to the laser cavity. By contrast, ICL

#J435 with its much larger mesa area will experience more heating with increasing current thus giving a larger current tuning rate.

Due to Fabry-Perot cavity effects, bare JPL interband cascade laser #J435 and #J653 have multimode emission. However potential applications in gas detection still can be developed. Multi absorption peak matching is possible for a multimode laser to scan in some specific temperature range. For complex organic molecules, narrow absorption peak is impossible, and a broad absorption peak will be the case for use of multimode emission laser in the spectrometer.

Chapter 5

System setup for a interband cascade laser based hollow waveguide gas sensing system

5.1 Introduction

For a high sensitivity gas detecting spectroscopy, multi-path absorption cells have been widely used to obtain a long optical path length to enhance sensitivities. For example, a specially designed optical cell technique, which is called cavity ring down, can achieve an optical path length of more than 10 km in a physical space less than one meter. However, beam alignment for multi reflection cells is always a challenge.

To alleviate this problem, a new technique for gas monitoring has been in which a hollow-core waveguide of <1 mm diameter is used as an absorption cell [59]. Compared with cavity ring down technique, hollow waveguides are much like fiber optics in that it transports mid-infrared energy. Nowadays, various types of hollow-core waveguide have been developed to deliver high-power CO_2 laser beams for applications in the medical and industrial fields [60,61]. In this chapter, the use of the hollow-core waveguide is introduced as an absorption cell for a gas absorption spectroscopy system.

The main advantages in using hollow-core waveguides are as follows:

- Relatively ease in light-beam alignment (Once the laser radiation is coupled into the waveguide). Since the waveguide works as a power transmission

line, no further alignment is required when the initial alignment is accomplished.

- Possibility for gas detection. If a provision is made to flow gas through the waveguide.

- Light and compact. With the hollow waveguide based gas spectroscopy, handheld detection system may be realized when used with a room temperature operating light source.

5.2 Hollow waveguide structure

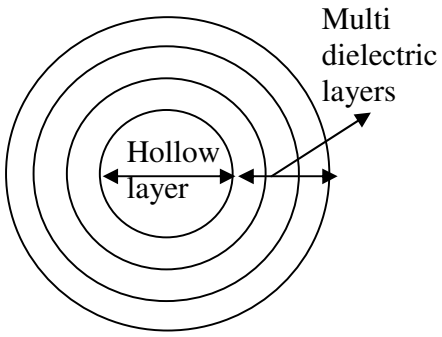


Figure 5.1: Structure design of hollow waveguides

As shown Figure 5.1, an OmniGuide waveguides has a hollow core surrounded by a multilayer mirror made of alternating layers with high and low indices of refraction. The mode structure in hollow dielectric waveguides were analyzed by Mihai Ibanescu, et al.[62]. Testing results show that OmniGuide waveguides and hollow metallic waveguides

have similar transmission modes. And TE01 mode is the lowest-loss mode in the dielectric waveguide and metal waveguide.

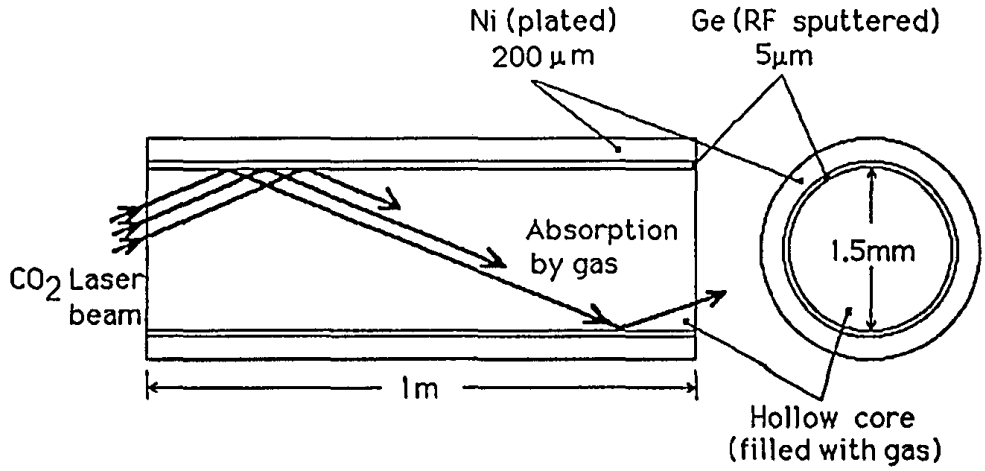


Figure 5.2: Beam paths in a hollow waveguide as an absorption cell [62]

Figure 5.2 depicts CO_2 laser transmission through a hollow-core waveguide as an absorption cell. It shows the laser beam with a specific wavelength fully reflected back into a hollow core. Usually, the laser beam will keep an incident angle close to zero degrees in order to get a full reflection from the boundary.

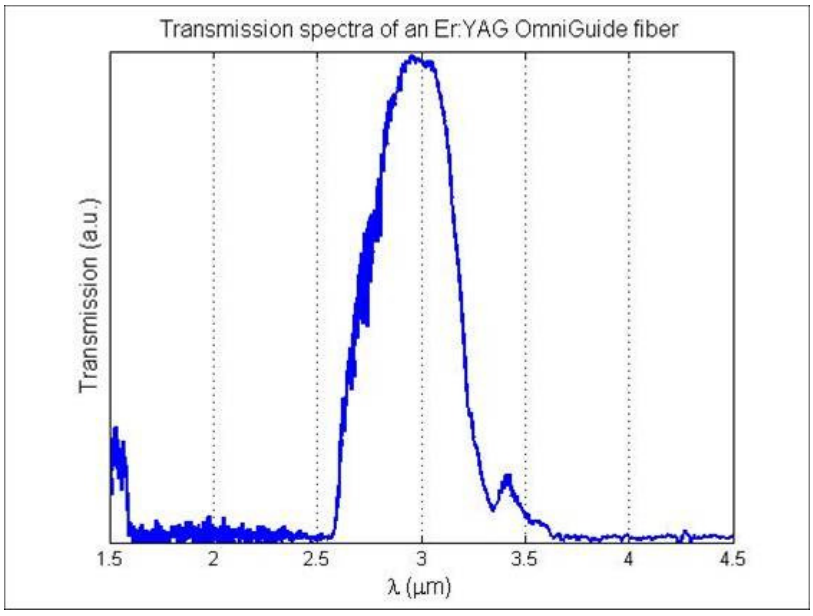


Figure 5.3: Transmission profile of the OmniGuide infrared waveguide [63]

In this chapter, two hollow waveguides are used to test the JPL ICL beam transmission. One is the Er:Yag infrared waveguide from OmniGuide company, which have a 0.22 mm core diameter and a 0.72 mm external diameter. The transmission spectrum of the waveguide is shown in Figure 5.3, which covers the 2.5 – 3.5 μm spectral range. Another is the hollow silica waveguide from Polymicro Technologies company, which has a 1 mm core diameter and 1.6 mm external diameter. The transmission spectrum of the waveguide is from 2.9 μm to 10.6 μm.

Since JPL ICL #J653 has an emission wavelength around 3.1 μm, both waveguides are well matched with this laser.

5.3 Experimental setup

The basic layout of the gas detecting spectroscopy system with the hollow-core waveguide is shown in Figure 5.4.

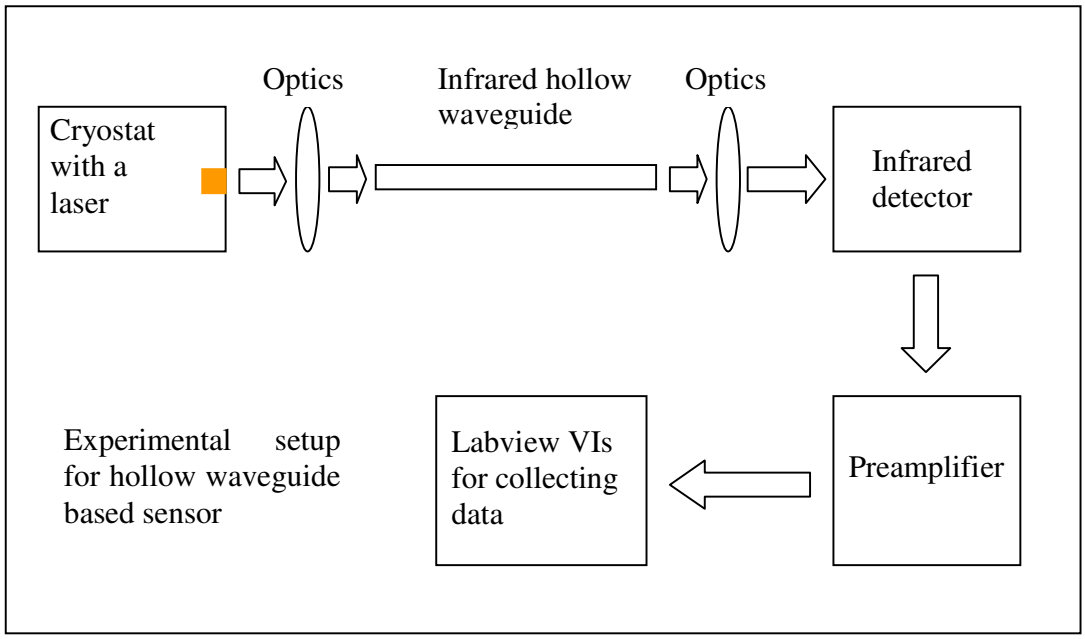


Figure 5.4: Experimental setup of an OmniGuide infrared waveguide based spectroscopy

JPL ICL #J653 beams are transmitted through the core by repeated reflections at the boundary between the hollow core (usually air) and the cladding. After the beams are focused into an inlet of the waveguide, no further alignment is needed.

If the hollow waveguide core is filled with gas which is ready to be measured, the laser beam will be transmitted through the gas core with an attenuation caused by

absorption of the gas molecules. The gas concentration in the core is determined by measuring the difference between the input peak intensity before the hollow waveguide and the output peak intensity after the hollow waveguide at specific laser wavelengths.

The main components of the hollow waveguide based gas spectroscopy are as follows:

- Optical lens (Bi-convex CaF_2 lens and Positive ZnSe meniscus): Focusing infrared light onto the infrared detector.
- ILX Lightwave current source
- Preamplifier: Amplifying photodetector signals
- Infrared Detector: Detecting infrared signals
- Stanford research SR380 Lock-in amplifier: Amplifying preamplified photodetector signals, reducing noise by many folds and increasing whole system sensitivity
- GPIB card and Labview program: Analyzing signals and displaying results

Most of them are introduced in previous chapters. The key consideration for a hollow waveguide based gas sensor design is the beam profile analysis in the optical setup and signal amplifying by a preamplifier.

5.4 Preamplifier circuit analysis

Signals obtained by infrared detectors are normally weak, for example, minimum current of a MCT detector is just at 30 – 50 pA. So a low noise amplifier or preamplifier will serve as a key part in an infrared detecting system.

Since there are plenty types of infrared detectors, it is not easy to find an impedance matched preamplifier for the infrared detector in the commercial market. Moreover, some preamplifiers designed in early 1990s are bulky and costly, and they are not suitable for some gas detecting systems which requires less space and flexibility.

Having a desirable preamplifier circuit diagram, which is designed for certain infrared detectors, is important to a hollow waveguide based gas spectroscopy.

Most preamplifier circuit diagrams are developed based on operational amplifiers. An operational amplifier (op-amp) is a DC-coupled high-gain electronic voltage amplifier with differential inputs. It is usually composed of differential pairs of NMOS and PMOS transistors.

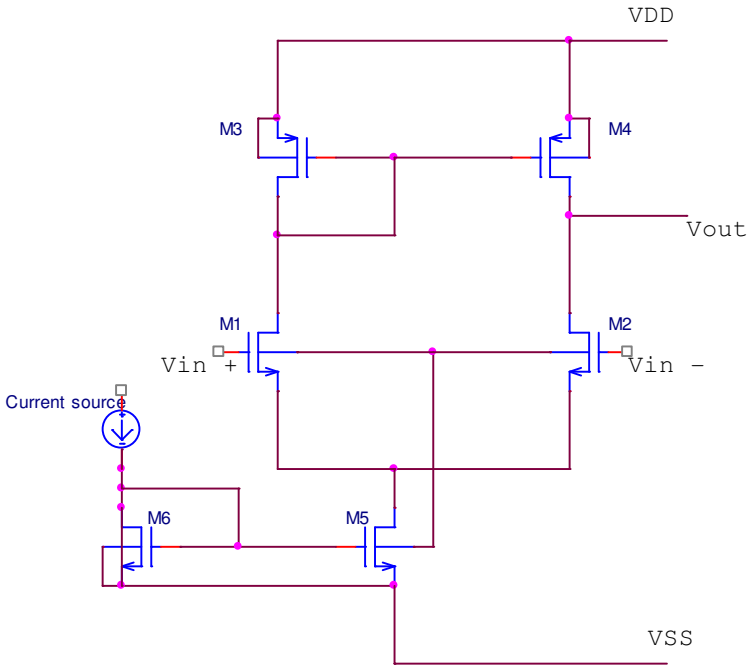


Figure 5.5: Circuit diagram of a one stage differential operational amplifier

Figure 5.5 is a one stage differential operational amplifier circuit. V_{in+} and V_{in-} are two input voltages, and V_{out} is the output voltage. If V_{in+} equals to V_{in-}, it is called common

mode (CM) input. Otherwise, it is called differential common (DM). One of the key parameters for op-amps is the open loop voltage gain, which is the output to input voltage ratio of the op-amp without external feedback. Another key parameter is common ratio rejection ratio (CMRR). CMRR can be calculated as follows:

$$CMRR = G_{cm} / G_{dm}$$

Where G_{cm} is common mode voltage gain, and G_{dm} is differential mode voltage gain.

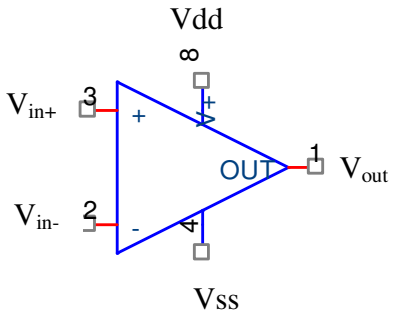


Figure 5.6: A simplified design for an operational amplifier

A simplified design for an operational amplifier is shown in Figure 5.6 with V_{in+}, V_{in-}, VDD, VSS and V_{out}.

$V_{out} = G \times (V_{in+} - V_{in-})$, where G is the gain of the operational amplifier, typically very large, in the range of 10,000 to 100,000.

One of basic applications for op-amps is a negative feedback amplifying circuit shown in Figure 5.7. In this case:

$$V_{in-} = \beta V_{out} \Rightarrow V_{out} = G \times (V_{in+} - \beta V_{out})$$

Since G is in the range of 10,000-100,000, usually $G\beta >> 1$

$$V_{out} / V_{in} = G/(1 + G\beta) \approx 1/\beta \Rightarrow V_{out} = V_{in} / \beta$$

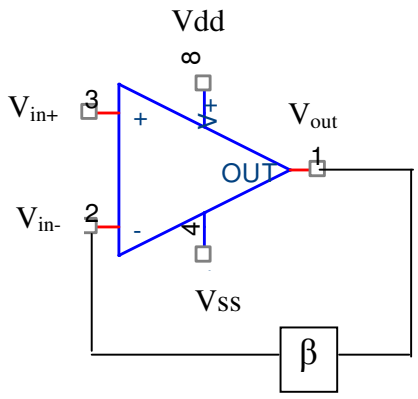


Figure 5.7: A simplified feedback design for an operational amplifier

A preamplifier circuit based on the negative feedback concept is shown in Figure 5.8, which is designed for infrared detectors.

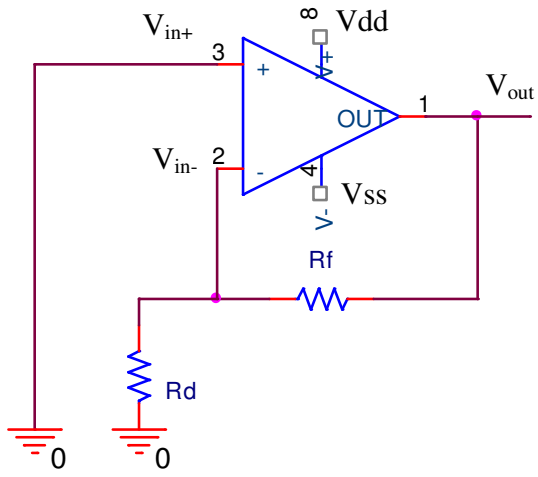


Figure 5.8: A simplified negative feedback preamplifier design

The infrared detector output is just a small voltage or current source with some impedance. So in this case, the feed back component will be a resistor to match the resistance of the infrared detector. The preamplifier system will be as follows:

$$\beta = R_d /(R_f + R_d) \Rightarrow V_{out} = V_{in} / \beta \Rightarrow V_{out} = (1 + R_f / R_d)V_{in} \approx (R_f / R_d)V_{in}$$

The Measured infrared detector resistance, R_d, is 110 ohms, so R_f will equal to 1100 ohms for a 10 times amplifying. In a real preamplifier design, two operational amplifiers will be used to get a better amplifying result. The first op-amp is used to increase the shunt resistance of infrared detector. The shunt resistance increase is necessary to achieve high signal gains and to obtain low output noise for the preamplifier. This method is called bootstrapping in a preamplifier design [64].

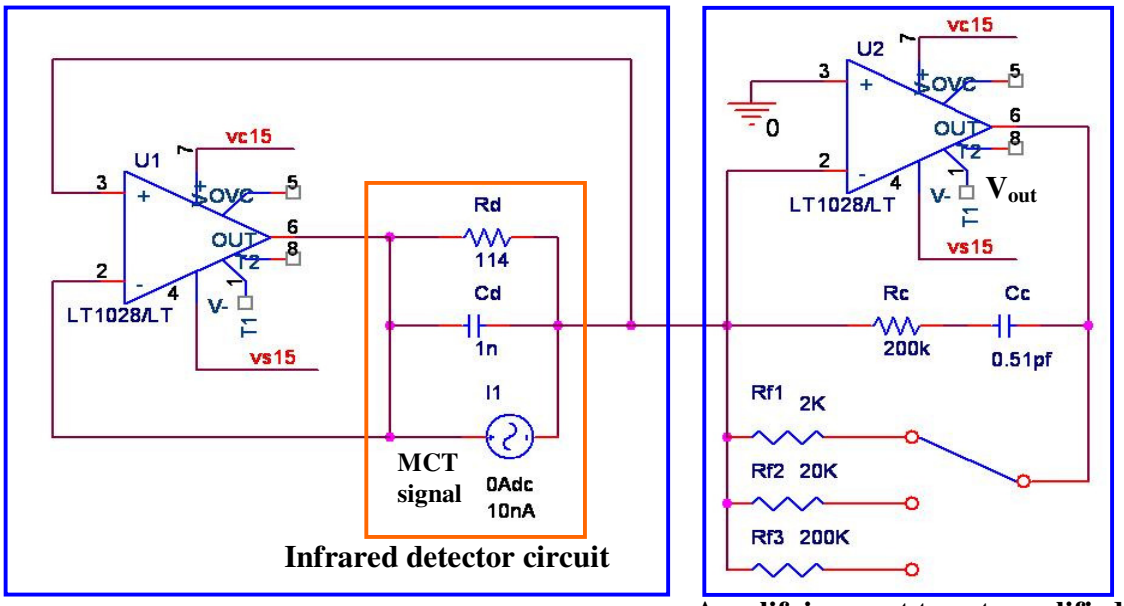


Figure 5.9: The designed preamplifier circuit diagram for MCT infrared detectors

Figure 5.9 is the complete circuit diagram for infrared detectors. The diagram is split into two parts. The first part is a bootstrapping circuit, and a LT1028 OP-AMP is used to increase input impedance for second amplifying part. The second part is an amplifying circuit. Three possible feedback resistors (2K, 20K and 200K) can be chosen by a switch.

Product of parallel resistor R_c and capacitor C_c provide a voltage gain compensation [65]. The equation for this circuit is:

$$V_{out} / i_1 = \frac{-R_f}{1 + sR_f C_c + (1 + sR_f C_c + (R_f / R_d + sR_f C_d)/(G_1 + 1))/G_2}$$

where V_{out} is the output voltage of preamplifier, i_1 is the infrared detector current, G_1 is the open loop gain of the bootstrap operational amplifier, G_2 is the open loop gain of the second operational amplifier, R_d is the equivalent resistance of the infrared detector, C_d is equivalent capacitance of the photodiode, R_f is the feedback resistance, and C_c is the capacitor for gain compensation.

When the infrared detector detects chopped infrared beams, obtained detector current will have a square-wave shape signal. Normally the current of the infrared detector will be at pA, nA and μA levels. Based on the preamplifier circuit in Figure 5.9, three input cases of square signal (100 pA at 250 Hz, 100 nA at 250 Hz and 100 μA at 250Hz) are analyzed.

If a 20K feedback resistor is connected, Figure 5.10 is the Orcad PSPICE simulated result of a square-wave shape detector current with a 100 pA at 250 Hz. The output voltage will be at mV level.

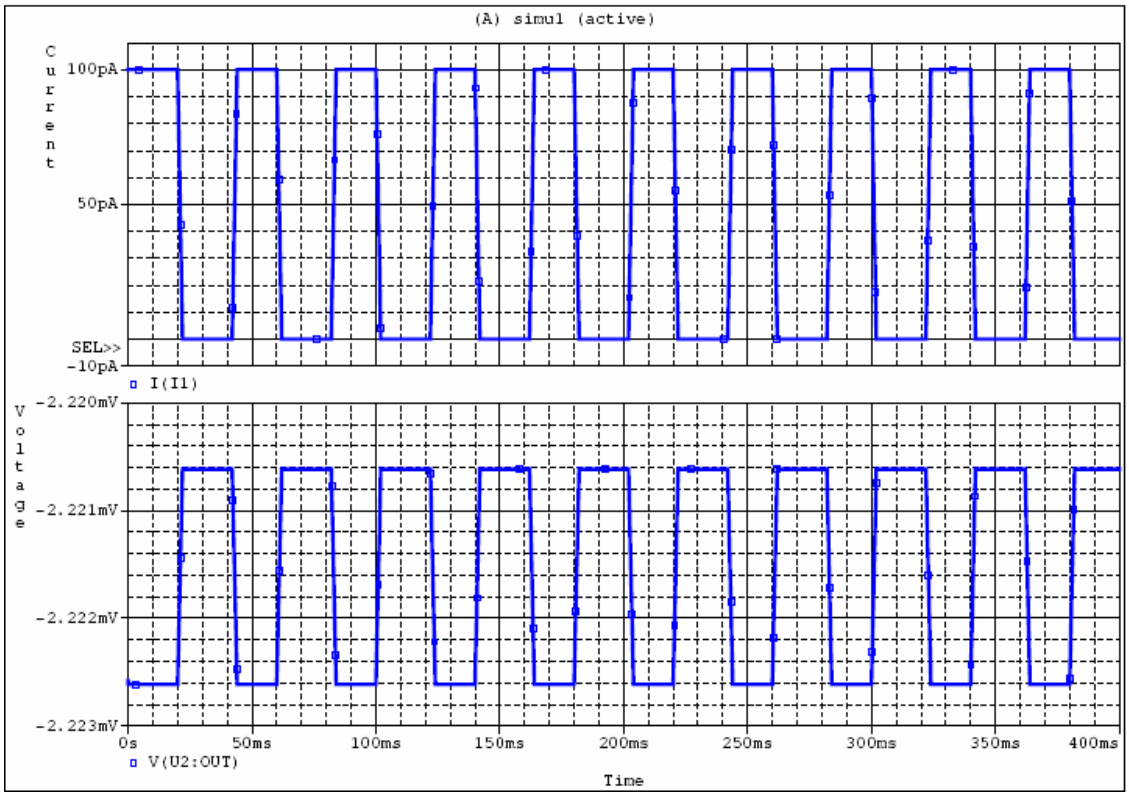


Figure 5.10: Simulated results of the circuit design a 20 K ohm feedback resistor in Figure 5.9 by Orcad 10.5

Output voltages of a detector current with 100 nA at 250 Hz and 100 μA at 250Hz are also simulated. Table 5.1 is the summarized values of varying feedback resistors and output voltages with three different input currents. To obtain an optimized signal, different feedback resistors should be connected depending on the input current level. For relatively weak infrared beam detection, a 100K resistor will be desirable to serve as a feedback resistor.

Table 5.1: Values of feedback resistor and simulated output voltage vs. three different input currents

	Feedback resistor	Output voltage
100 pA at 250 Hz	10K	0.85uV
	100K	8.5uV
	1M	0.082mV
100 nA at 250 Hz	10K	0.85mV
	100K	8.5mV
	1M	85mV
100 μA at 250 Hz	10K	0.85V
	100K	8.5V
	1M	13.5V

5.5 Beam profile analysis in the optical path

Beam profile analysis, including the beam width and the beam shape on the optical path, is critical for alignment of a hollow waveguide based gas spectroscopy system.

All infrared beams spread out, or diverge, as they travel away from their sources. Lasers are the most directional light sources available, but even the beams diverge with distance. Figure 5.11 shows a beam diverging as it leaves a laser.

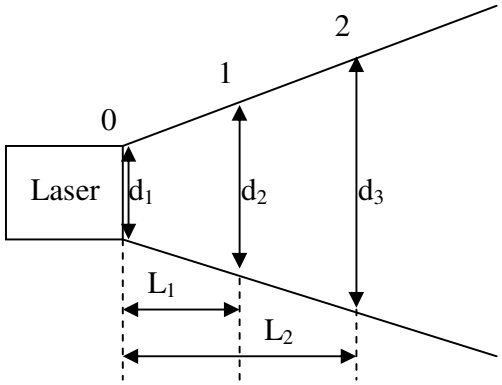


Figure 5.11: Beam profile of a laser

In the setup of the JPL ICL #J653, a ZnSe lens is placed in front of the cryostat emission window to collect diverged laser beams onto a parabolic off-axis mirror. Since the distance between ZnSe lens and laser source is approximately one inch, which is the focal length of the ZnSe lens, a collimated beam will be collected by the off-axis parabolic mirror. The off-axis parabolic mirror will further convert a collimated beam into a converged beam toward the hollow waveguide. In order to match the beam width with the small core diameter of the waveguide, a four inch focal length CaF_2 lens was placed in the path of the converged beam waist to focus the beam into the waveguide core.

The detailed setup is shown in Figure 5.12.

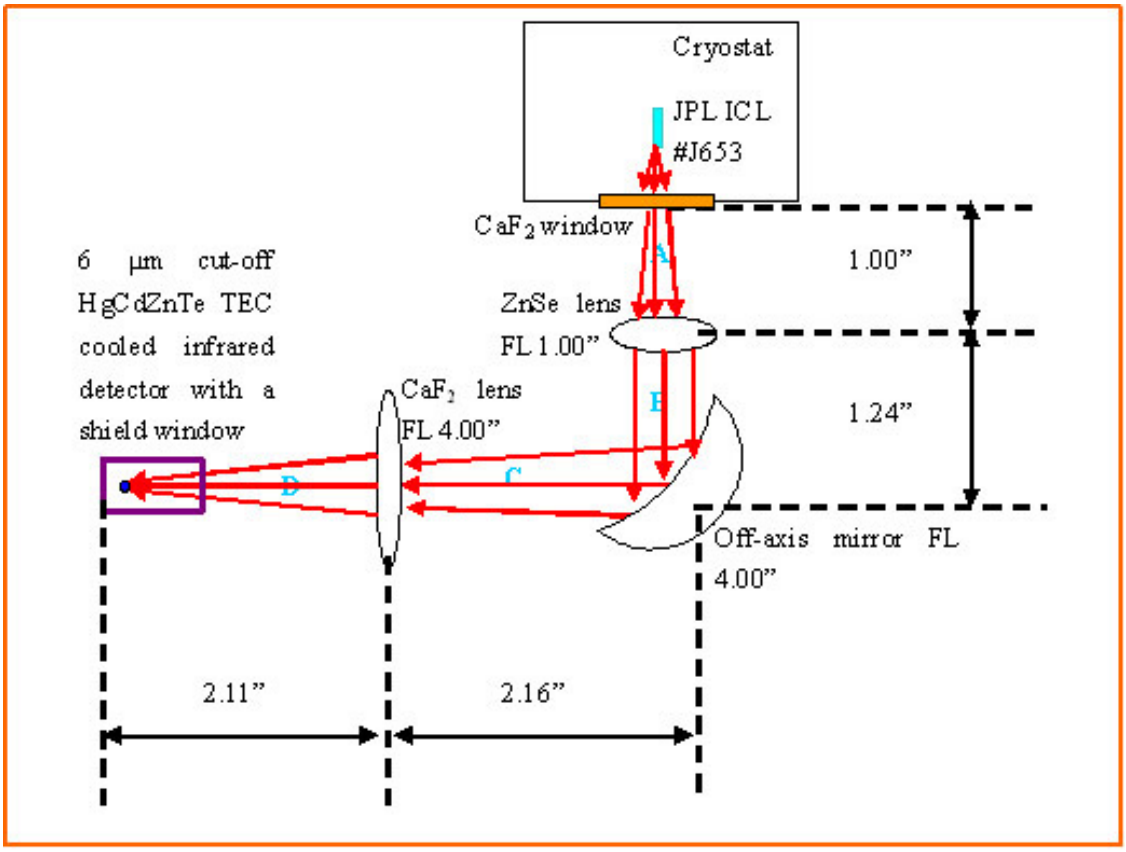


Figure 5.12: Schematic of the optics setup to focus laser beams onto the infrared detector

To analyze the beam profile, the whole optical path was split into four regions. The beam profile in these regions is as follows:

- Region A: Diverging beams
- Region B: collimating beams (Beam width around 0.8")
- Region C: converging beams

- Region D: furtherconverging beams

Without a CaF_2 lens between region D and region C, the pre-amplified detected signal is about 8 volts when the laser was pumped by a 6 mA injection current with a 82 K cold finger temperature. With a lens, the detected signal will reach 22 volts under the same injection current and the cold finger temperature. The above results indicated the 4.0" focal length CaF_2 lens focused 3.5 times more light onto the 1*1 mm^2 MCZT detector.

If a 2.0" focal length ZnSe lens replaces a 4.0" focal length CaF_2 lens to test focusing effects, the detected signal is about 15 volts when the laser was pumped by a 6 mA current with a 82 K cold finger temperature. It indicates that the longer focal length (4" focal length) CaF_2 lens is more effective in focusing mid-IR light onto a small spot.

5.5.1 Beam width analysis in region D

When the beam alignment is accomplished, the OmniGuide hollow waveguide will be placed at the detection point of the detector to accept the laser beam into the hollow core. It is important to know a distance from the detector window and detecting element as shown in Figure 5.13.

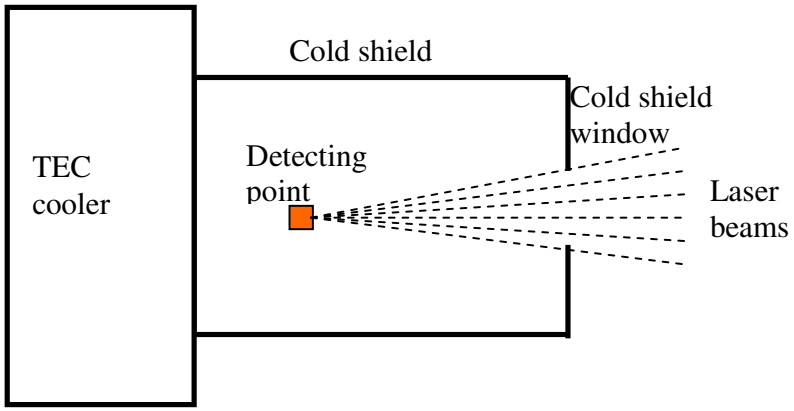


Figure 5.13: Schematic of a TEC cooler and detecting the laser beams

In Figure 5.14, to measure the distance from the cold shield window to detecting point inside the detector, beam widths at different positions are measured by an adjustable aperture in region D. Position 1 is just on the face of the outside window of the detector. The distance between position 1 and 2, position 2 and 3 are read from the translation stage.

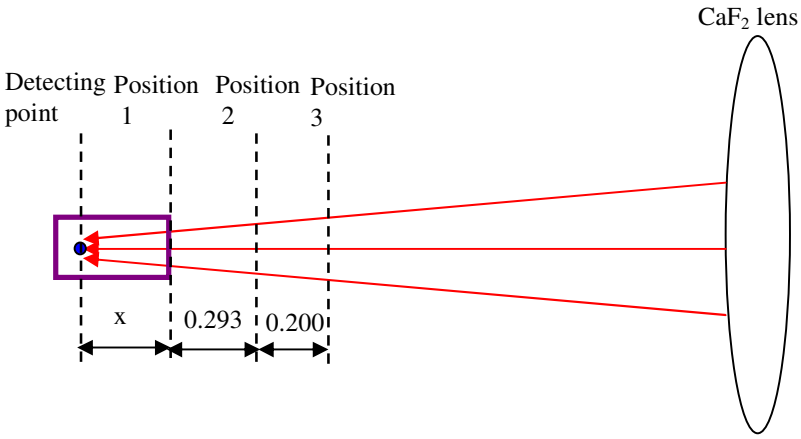


Figure 5.14: Schematic of beam width measurements in region D

Figure 5.15 depicts that the measured beam width is 0.100” at position 1, 0.177” at position 2 and 0.226” at position 3. The distance between position 1 and 2 is 0.293”, and the distance between position 2 and 3 is 0.200”. Both the distance values are directly read from the translation stage with a mounted aperture.

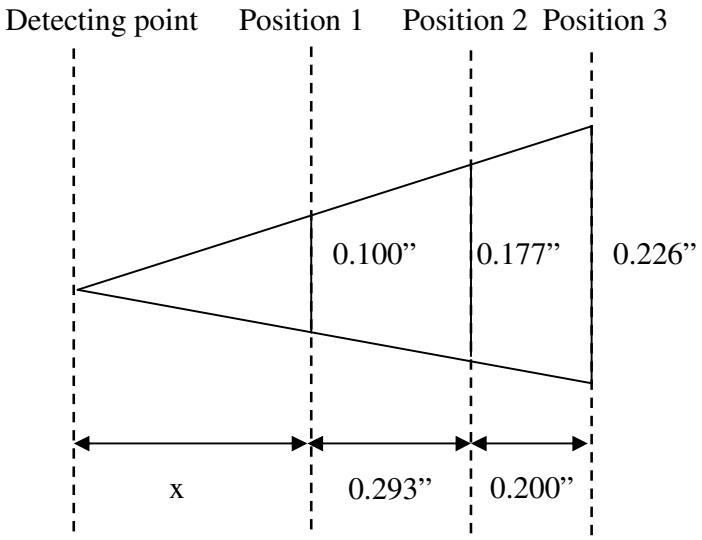


Figure 5.15: Measured beam width at positions with interval distances

If the distance from the outside window to the detecting point inside the detector is x, values of x are calculated according to the measured beam widths at different positions

Position 1 and 2:

$$x/(x+0.293) = 0.100/0.177 \Rightarrow x = 0.381"$$

Position 1 and 3:

$$x/(x+0.493) = 0.100/0.226 \Rightarrow x = 0.391"$$

Position 2 and 3:

$$(x+0.293)/(x+0.493) = 0.177/0.226 \Rightarrow x = 0.429"$$

Three different values of x are calculated based on different combinations of measured data, and the deviation is large. It may be due to the imprecisely measured values of beam widths.

The calculated average is 0.40 inches, and the actually measured distance from the outside window to detection point is about 0.40 inches. So x (the distance from the shield window to the detecting point) equals to 0.40 inches. It is also confirmed that measured beam widths at different positions are reasonable.

From x value, it is possible to calculate beam width at any position in region D if related distance is measured. Based on the measured distance from position 3 to CaF_2 lens, the beam width on CaF_2 lens can be calculated.

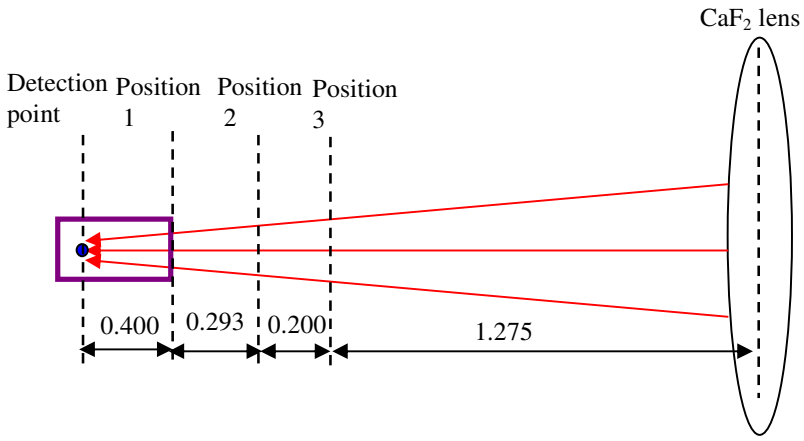


Figure 5.16: Calculation of beam width on CaF_2 lens

Assuming beam width on the CaF_2 lens is y, the measured distance from position 3 to CaF_2 lens is 1.275 inch as shown in Figure 5.16:

$$0.40/(0.40+1.768) = 0.10/y \Rightarrow y = 0.542"$$

The calculated beam width on CaF_2 lens is about 0.54 inch. Since the collimating beam width in region B (after ZnSe lens) is about 0.80 inch. So the calculated result is reasonable because the beam width in region B will be larger than that on the CaF_2 lens in region C.

5.5.2 Beam shape analysis in region D

The laser beam shape close to the hollow waveguide is a key factor to estimate how much power will be delivered into the hollow core. Based on the beam shape profile, the beam width and the hollow core diameter, percent of beam power to be delivered into hollow core can be calculated.

Figure 5.17 shows X and Z scanning direction to check the beam shape.

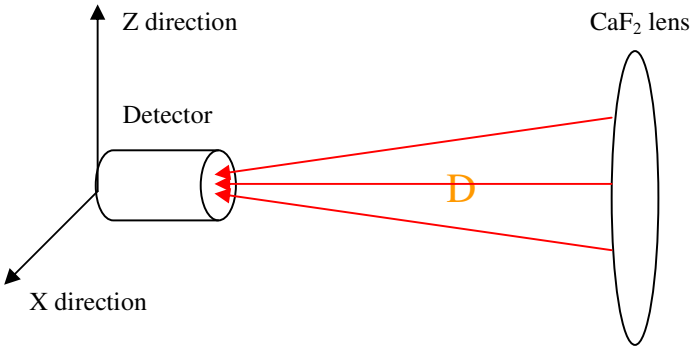


Figure 5.17: Scanning directions of detector for beam shape measurement

Both x and z direction scanning are performed by a translation stage after the detector signal reaches the maximum value, which is about 22 volts at 6 mA injection current with 82.40 K cold finger temperature.

The beam shape along x direction is shown in Figure 5.18 below and approximately symmetrical.

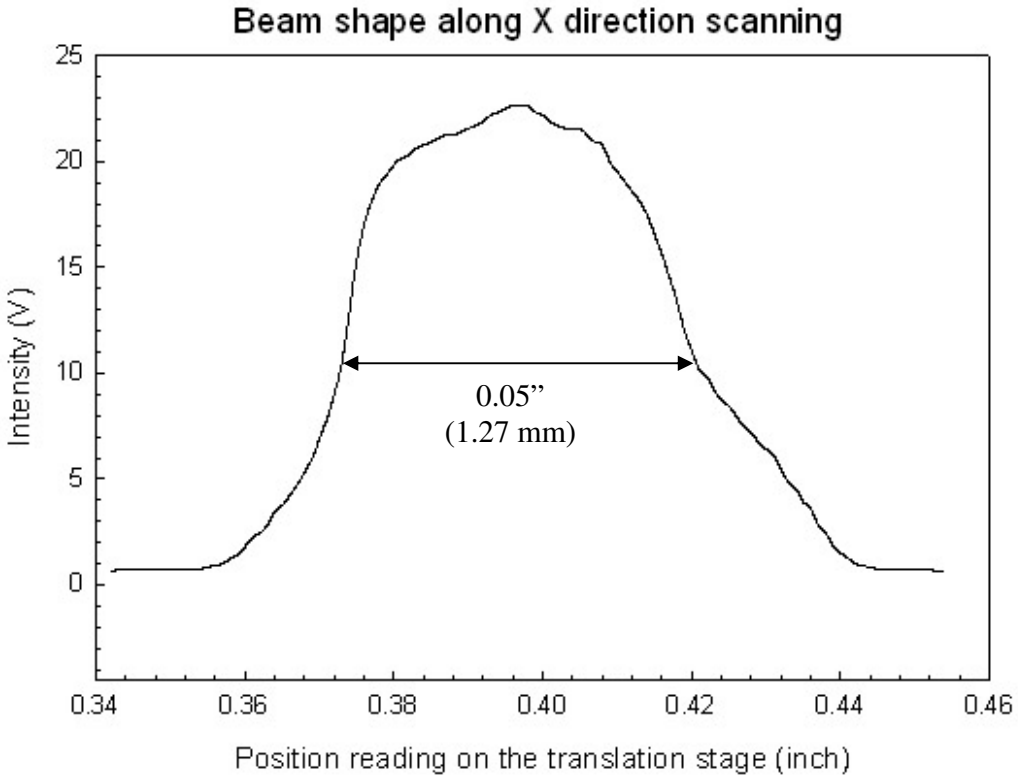


Figure 5.18: Beam shape in X direction

The beam shape along the Z direction is shown in Figure 5.19. An unsymmetrical shape is observed. From the testing process, it is maybe caused by the unsymmetrical shape of the chopper wheel.

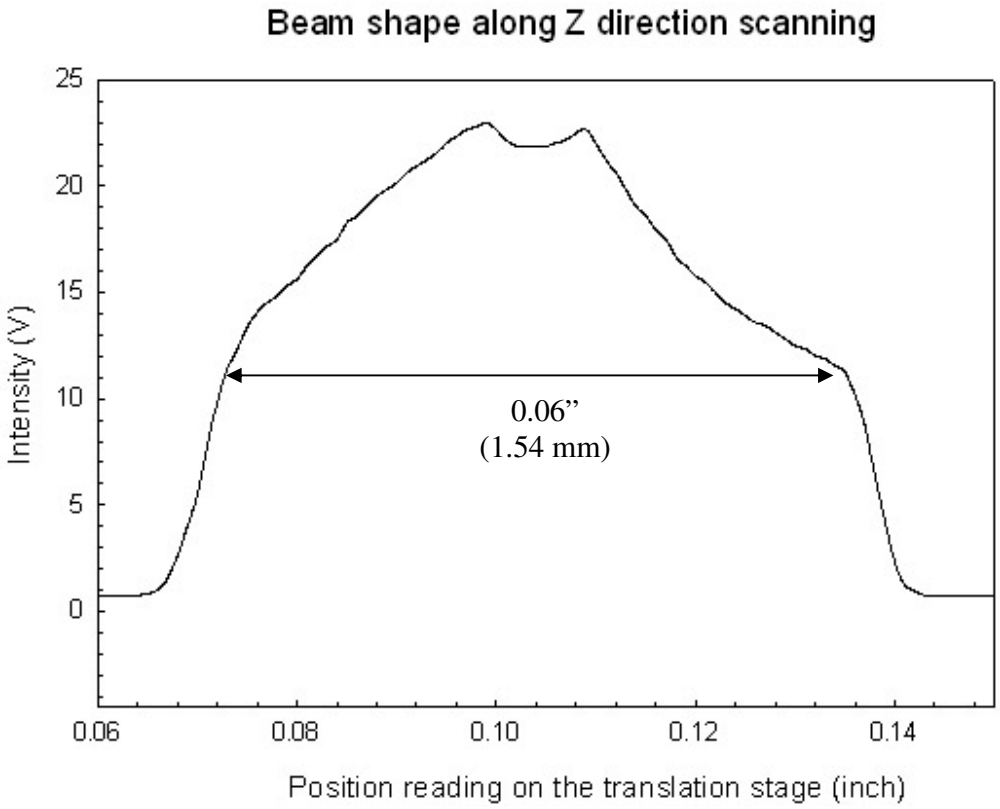


Figure 5.19: Beam shape in Z direction

From the measured beam width in Figure 5.18 and 5.19, the laser beam is approximately elliptical with the spot size of 1.27 mm * 1.54 mm.

For the 1 mm core diameter hollow waveguide from Polymicro Technologies Company, if ignoring all losses, the amount of power which will be coupled into the hollow core is calculated as follows:

$$\frac{Area_{Waveguide}}{Area_{Spot}} = \frac{(\sim 0.50mm)^2}{(\sim 0.70mm)^2} = \sim 51\%$$

From the above calculation, if a 1 mm core diameter hollow waveguide is used in the setup, half of the laser power could be coupled into the waveguide if ignoring all other losses.

For the 0.22 mm core diameter hollow waveguide from OmniGuide Company, if ignoring all losses, the amount of power which will be coupled into the hollow core is calculated as follows:

$$\frac{Area_{Waveguide}}{Area_{Spot}} = \frac{(\sim 0.11mm)^2}{(\sim 0.70mm)^2} = \sim 2.5\%$$

From the above calculation, if a 0.22 mm core diameter hollow waveguide is used in the setup, only 2.5% of the laser power could be coupled into the waveguide if ignoring all other losses. The result indicates that further narrowing the spot size is needed to focus most of the laser beam into 0.22 mm diameter hollow waveguide.

A Nikon infrared camera is used to check the focused beam spot visually. Figure 5.20 shows the position to check the size of the focused beam spot by a Nikon infrared camera. The dotted line indicates the laser beam path.

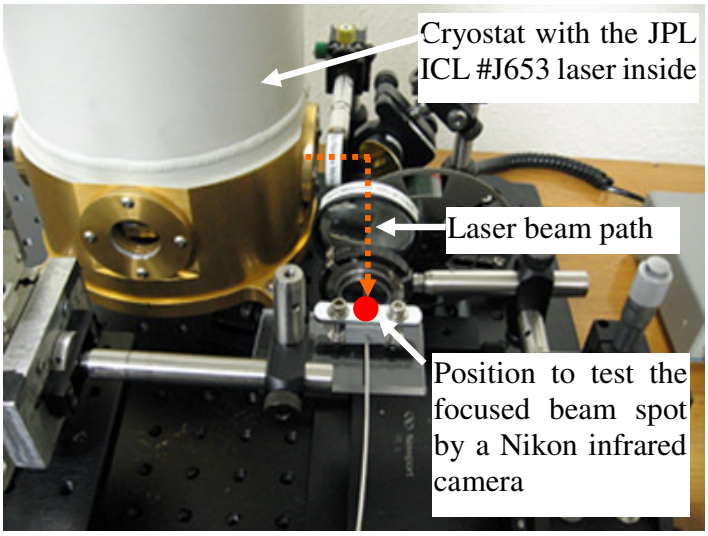
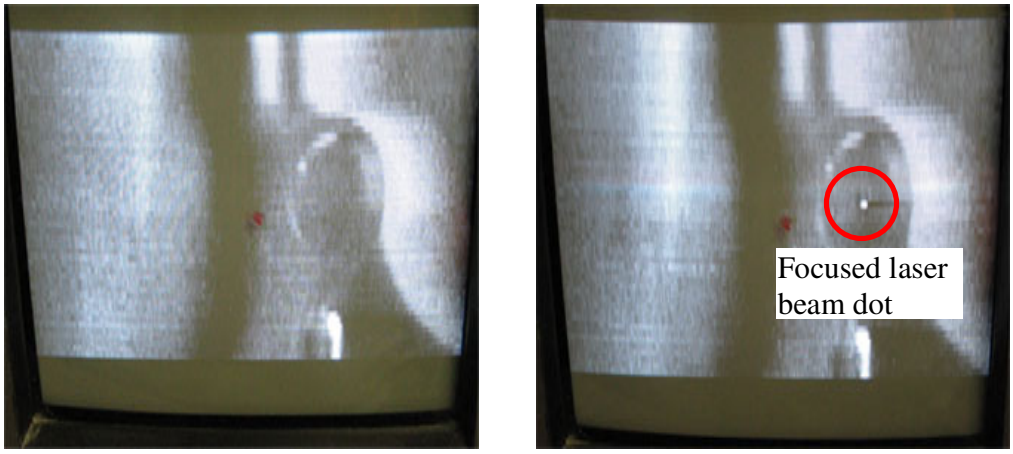


Figure 5.20: Position to check the focused beam spot

Figure 5.21 (a) is a picture taken by a Nikon infrared camera before the laser is on, and Figure 5.21 (b) is the picture taken by the same camera after the laser is on. The white spot in Figure 5.21 (b) is the focused mid-infrared beams close to the detector and it clearly indicated the focused beam position is right on the aperture. If a hollow waveguide tip is put right in front of the aperture, the beam can be coupled into the hollow core of the waveguide. The measured beam width or the spot size is about 1.4 mm.



(a) (b)

Figure 5.21: Beam spot on the focused position which was taken by a Nikon infrared camera: (a) The laser is off: (b) The laser is on

5.6 The whole optical setup and tested results

Figure 5.22 is the picture of the whole setup with a cryostat, the JPL interband cascade laser, optical lenses, a 1 mm diameter hollow waveguide and the MCT infrared detector. One tip of the 1 mm diameter waveguide is placed in front of the aperture, and the other tip is aligned with a MCT infrared detector. Since the laser beam size is ~ 1.4 mm and the hollow core diameter of the waveguide is 1 mm, the alignment is not difficult.

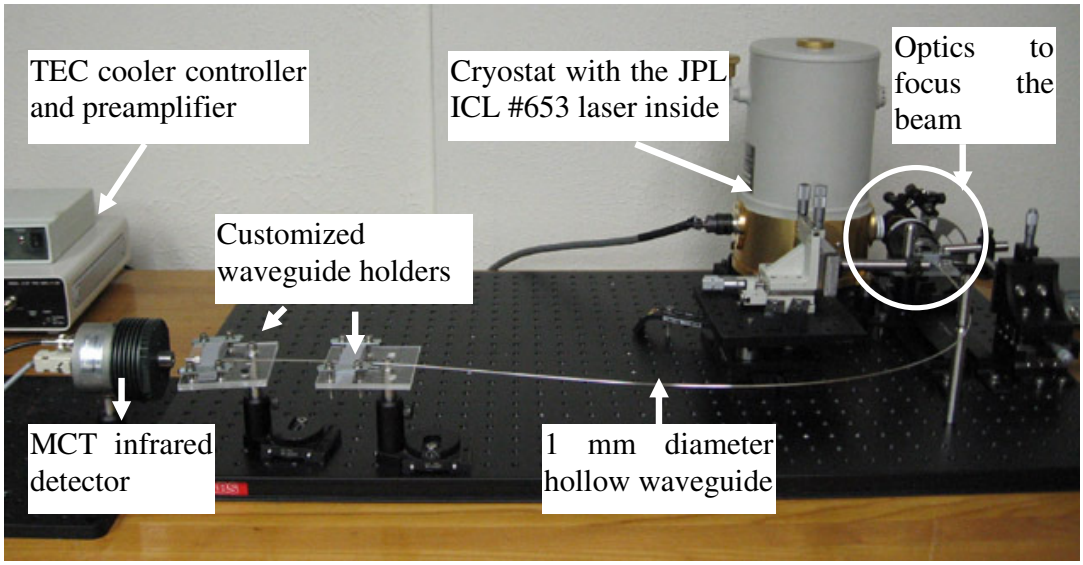


Figure 5.22: The picture of the whole setup with a cryostat with the JPL ICL laser, optics, a 1 mm diameter hollow waveguide and the MCT infrared detector

Figure 5.23 is the picture of the setup with a tip of 1 mm diameter hollow waveguide and the MCT infrared detector. Since the detection area of the MCT detector is comparable with the diameter of the hollow waveguide (1 mm), the alignment is not difficult. To get transmitted beam analysis, the MCT infrared detector was replaced by a MIR 8000 FTIR system. The tested FTIR results are shown as next.

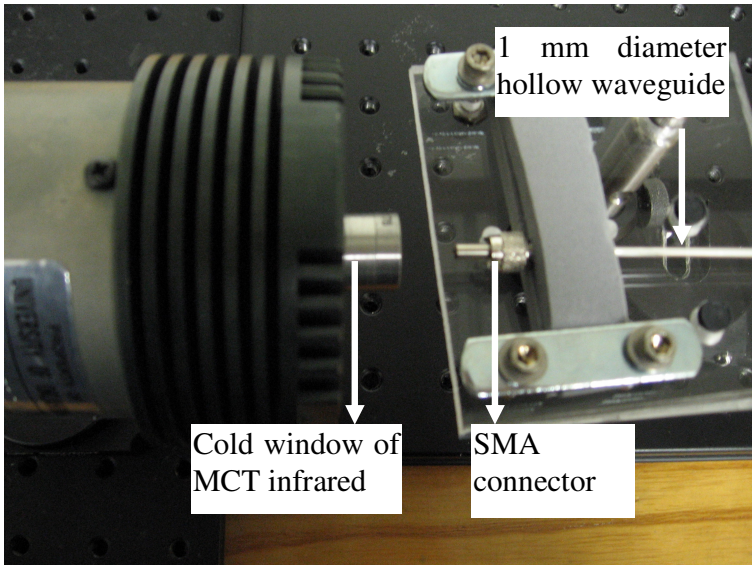


Figure 5 23: The picture of the alignment of the tip of 1 mm diameter hollow waveguide and the MCT infrared detector

Figure 5.24 is the measured result without 1 mm waveguide and with 1 mm waveguide. Without the waveguide, the ratio of side mode intensity and major mode intensity is ~0.15. And with the waveguide, the ratio is ~0.13. By comparison, it can be seen that there are no obvious difference for the laser beam profile with or without a hollow waveguide.

The major mode intensity without the waveguide is ~10 a.u., and the major mode intensity with the waveguide at the same condition is ~2 a.u.. So when the laser was operated at 29 mA injection current and 82 K heat sink temperature, the mode intensity was reduced by 80% compared with emission without the waveguide.

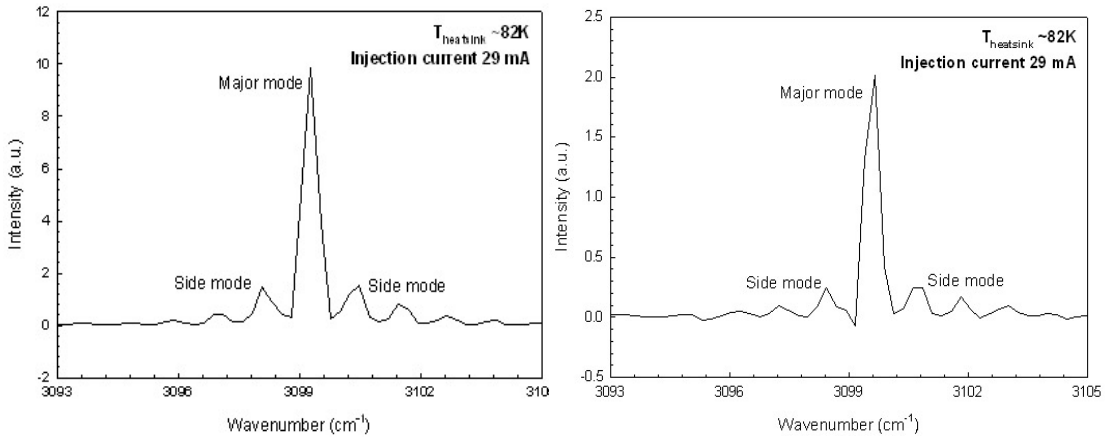


Figure 5.24: (a) Laser beam profile without the 1 mm waveguide and aligning optics; (b) Laser beam profile with the 1 mm waveguide and aligning optics

Figure 5.25 shows the laser emission of JPL ICL #J653 at different heatsink temperatures. At an injection current of 29 mA and a heatsink temperature of 82 K, the laser emission is close to a single mode emission. At other heat sink temperatures (83 K, 84 K and 85 K), multi mode emission is obvious. Even at 82 K heat sink temperature, if the injection current increases, multi mode emission become more obvious.

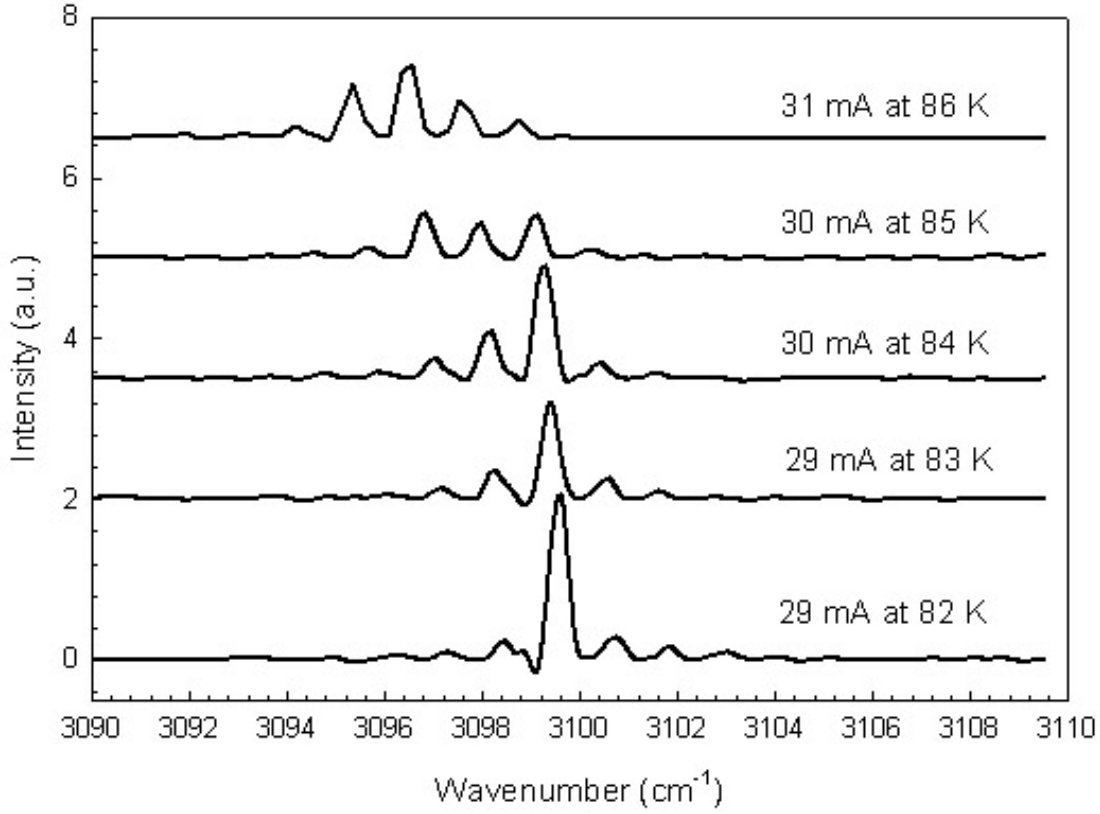


Figure 5.25: Transmitted beam profiles at the threshold conditions at different heat sink temperatures

Figure 5.26 shows that the multi mode emission is obvious at injection currents higher than 29 mA. With increasing injection currents, side mode intensity become more intense and the ratio of side mode intensity versus major mode intensity decreased. Multi mode emission becomes more obvious.

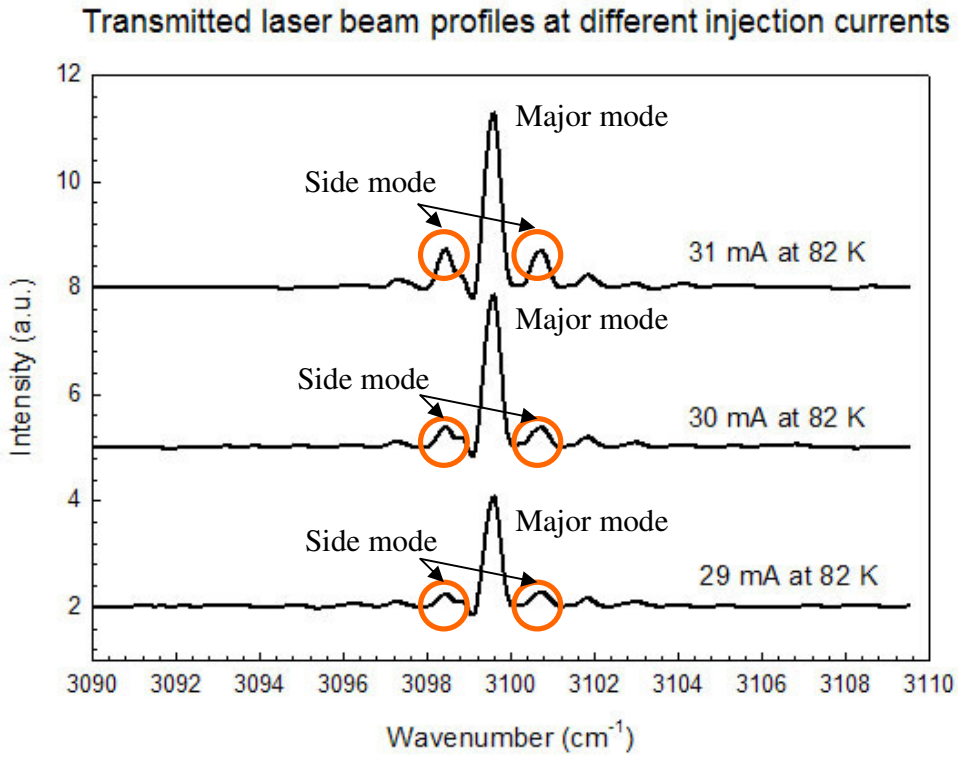


Figure 5.26: Transmitted laser beam profiles at different injection currents

5.7 Using a ball lens to narrow the beam width

In the above setup, with two lenses and an off-axis parabolic mirror, the focus beam width at the focusing point is around 1.4 mm. And this beam width or the beam spot size is able to couple a 1-mm diameter hollow waveguide. However, it is still too large to couple a 200-μm diameter hollow waveguide. To further narrow down the beam width of the laser beam, a CaF_2 ball lens is proposed to be added in front of the hollow waveguide.

Ball lenses, which are highly transparent spheres made of optical glasses, can be used to further focus the laser beam into the hollow core. Ball Lenses have high coupling

efficiency and should be much easier to align than traditional lenses due to its physical shape. Figure 5.27 is a setup with a ball lens to focus beams into the hollow waveguide. R is the distance to the central line, β is the value of tanθ, z is the distance from the incident beams to the ball lens, d is the diameter of the ball lens, and T is the diameter of the hollow waveguide.

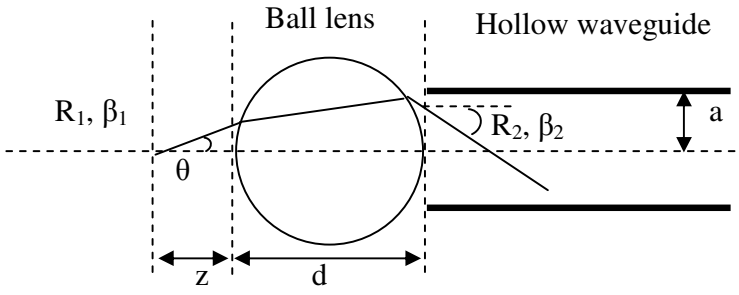


Figure 5.27: A setup with a ball lens to focus beams into the hollow waveguide [66]

In the Figure 5.27, the transmission can be expressed using the following equation [66]:

$$\begin{pmatrix} R_2 \\ \beta_2 \end{pmatrix} = \begin{pmatrix} A & B \\ C & D \end{pmatrix} \bullet \begin{pmatrix} R_1 \\ \beta_1 \end{pmatrix}$$

Since $R_1=0$ and $\beta_1=\tan\theta$, R_2 and β_2 can be calculated as follows:

$$R_2 = B * \tan\theta \quad , \qquad \beta_2 = D * \tan\theta$$

According to T. Katagiri's work [67], if n denotes the refractive index of the ball lens, B and D can be calculated as follows:

$$B = d/n + (2/n - 1)z \quad , \qquad D = 4z(1-n)/nd + 2/n - 1$$

When R_2 equals to the diameter of the hollow waveguide (T), the maximum incident angle θ and the optimized distance z can be calculated.

Supposed a CaF_2 ball lens with 2 mm diameter from ISP Optics company [68] is used in the setup. CaF_2 has a refractive index of 1.40 at 3 μm.

Since the incident beams have a path described in Figure 5.28, the value of θ can be calculated by the data in section 5.6.1. Therefore, $\tan\theta = 0.050/0.381 = 0.131$

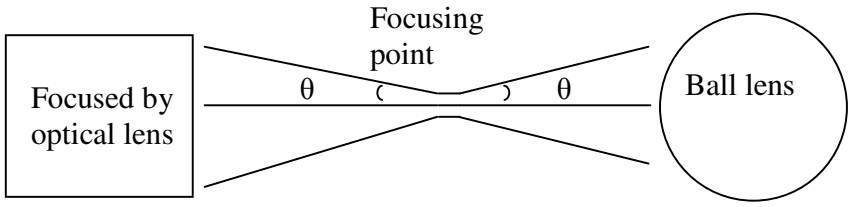


Figure 5.28: Schematic of angle θ at the focusing point

$R_2 = B * \tan\theta = (d/n + (2/n - 1)z) * \tan\theta \le D_{hw}$, where D_{hw} is the diameter of the hollow waveguide

$$(2/1.40+(2/1.40-1)z)*0.131 \le D_{hw} \Rightarrow z \le (7.634D_{hw}-1.429)/0.429$$

The calculated distances from the ball lens to the hollow waveguide (z) according to different diameters of the hollow waveguide are summarized in Table 5.2.

Table 5.2: Diameter of the hollow waveguide versus the optimized distance from the ball lens to the hollow waveguide

Diameter of the hollow waveguide (mm)	0.2	0.3	0.4	0.5	0.6	0.7	0.8	0.9
The optimized distance from the ball lens to the hollow waveguide (mm)	0.228	2.007	3.787	5.566	7.346	9.125	10.905	12.684

5.8 The whole optical setup with a ball lens

Figure 5.29 is the whole optical setup with a ball lens. In Figure 5.29, a 1.0" focus length ZnSe lens is placed at the end of the hollow waveguide. As calculated in section 5.7, the focused point by 4.0" focus length CaF_2 lens to the hollow waveguide is 0.228 mm if a CaF_2 ball lens with 2 mm diameter is used in the setup. At the end of the hollow waveguide, a pair of ZnSe lenses is used to focus the transmitted beams onto the infrared detector.

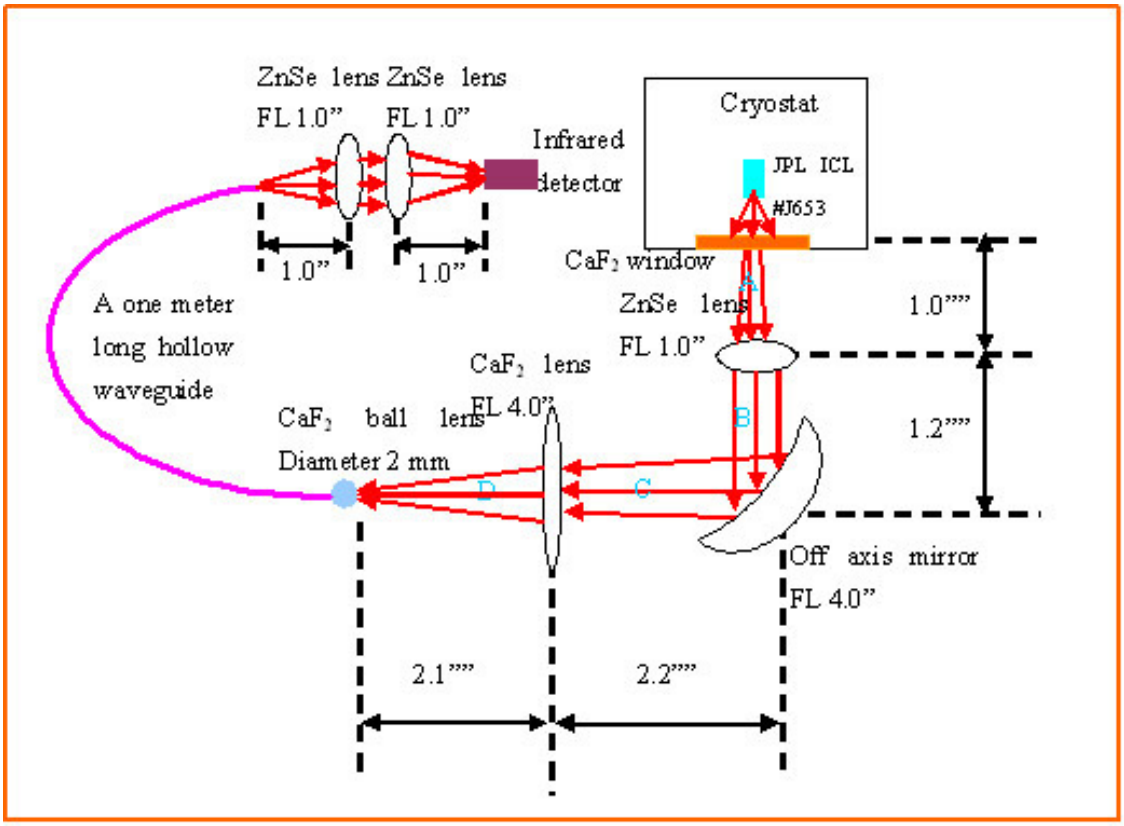


Figure 5.29: The whole setup of the hollow waveguide based system for gas sensing

5.9 Summary

Because of many advantages, the use of the hollow-core waveguide is introduced as an absorption cell for a gas absorption spectroscopy system.

One of the key considerations for a hollow waveguide based gas sensor is signal amplifying and noise reducing by a preamplifier. Based on bootstrapping method in preamplifier design, the designed preamplifier circuit can easily realize current (pA) to mV voltage (mV) conversion.

Beam profile in the optical path was analyzed by a three dimensional scanning. The results indicated that the focus laser beam is a Gaussian shape beam with a minimum focused beam width is around 1.4 mm. Further work was performed to evaluate the utility of hollow-core waveguides to manipulate mid-infrared radiation. Emission from a JPL ICL laser beam was focused and aligned into a 1 mm diameter hollow waveguide from Polymicro Technologies and measured with an FTIR spectrometer after traveling a distance of 1 meter through the waveguide. By comparison, it can be seen that there are no obvious difference for the laser beam profile with or without a hollow waveguide. When the laser was operated at 29 mA injection current and 82 K heat sink temperature, the mode intensity was reduced by 80% compared with emission without the waveguide.

A ball lens is suggested to be added in the optical setup to further focus the laser beam into the hollow core of the 0.22 mm diameter waveguide from OmniGuide company. Optimized distances between the ball lens and focused point of the CaF_2 lens are calculated on different core diameters of the waveguide. As calculated in section 5.7, the focused point by 4 inch focus length CaF_2 lens to the hollow waveguide is 0.228 mm if a CaF_2 ball lens with 2 mm diameter is used in the setup.

Chapter 6

Summary and suggestions for future work

In this dissertation, a filter wheel based mid-infrared spectrometer was developed to detect mid-infrared radiation between 1875 cm^{-1} and 3627 cm^{-1}. Based on this spectrometer, emission power of the infrared blackbody IR-12 at different temperatures (838 K, 923 K, 973 K. 1013 K and 1098 K) are calculated. Considered infrared blackbody emission factors, which include solid angles and emissvity, were considered to apply corrections to obtain more accurate emission power estimations of blackbody IR-12 at different temperatures.

Photoluminescence test of IV-VI quantum wells sample W336 was taken by the filter wheel based mid-infrared spectrometer. By calculating the ratio of the area under the measured spectral curve for sample W336 and area under different blackbody temperatures spectral curves, IV-VI quantum wells sample W336 photoluminescence power was estimated.

From different photoluminescence estimations based on different blackbody temperature curves, W336 photoluminescence power varied from 0.141 - 0.241 mW. The average was about 0.183 mW. In future work, more precise measurement of photoluminescence power emission will be performed by further improvements in data acquiring techniques and the incorporation of a quantum detector with a higher detectivity, thus allowing for photo lifetime in quantum well structure samples could be investigated.

In mid-infrared emitter device processing, thermal management is one of the most important factors for high-temperature, high-power continuous wave operation of quantum cascade lasers. A desirable packaging technique could achieve improved heat dissipation and lower laser threshold currents for optoelectronic devices. The epi-side down method is a new design for laser packaging. Since the epitaxial active region is connected directly to the heat sink, the packaged laser will have improved heat dissipation while improving operational reliability. Both epi-side down and epi-side up methods for interband quantum cascade lasers from NASA's Jet Propulsion Laboratory were studied and documented in chapter 3.

As the limited availability of lasers for packaging experiments, FTIR data were only obtained from our epi-side down packaging method with limited improvement in heat dissipation. However, some groups did get desirable improvements in heat dissipation and higher emission power using the epi-down method.

From measured FTIR data of different JPL interband cascade lasers (ICLs), it can be concluded that the number of JPL interband cascade laser (ICL) emission modes increase with increasing pumping current..

Small current tuning rates for the ICL sample #J653 at 86K were observed. The current tuning rate of the laser is less than 0.1 cm^{-1}/ mA and is undesirable for spectroscopy applications. So the main tuning technique for this type of quantum cascade laser will be realized by temperature tuning or external cavity tuning. In contrast to small current tuning rates for laser #J653, a larger current tuning rate for JPL #J435 of around 1.2 cm^{-1}/ mA was observed at 80K. This difference may be caused by different sized mesa

stripes. ICL #J653 has a mesa width of 15 μm and a cavity length of 1.5 mm, while ICL #J435 has a mesa width of 150 μm and a cavity length of 1 mm. A smaller current tuning rate is consistent with less active region heating, and ICL #J653 with its thinner mesa width will have more effective active region heat dissipation due to better lateral heat flow normal to the laser cavity. By contrast, ICL #J435 with its much larger mesa area will experience more heating with increasing current thus giving a larger current tuning rate.

Further work was performed to evaluate the utility of hollow-core waveguides to manipulate mid-infrared radiation. Emission from a JPL ICL laser beam was focused and aligned into a 1 mm diameter hollow waveguide from Polymicro Technologies and measured with an FTIR spectrometer after traveling a distance of 1 meter through the waveguide. By comparison, it can be seen that there are no obvious difference for the laser beam profile with or without a hollow waveguide. When the laser was operated at 29 mA injection current and 82 K heat sink temperature, the mode intensity was reduced by 80% compared with emission without the waveguide.

Improvement in fiber-coupling optical alignment by using an infrared transparent ball lens is also analyzed theoretically. The optimal distance between the ball lens and a 0.22 mm inner diameter hollow waveguide was determined to be 0.228 mm when placed at the focal point of a 4 inch focal length CaF_2 lens.

REFERENCES

[1] I.S. Glass, "Handbook of Infrared Astronomy", Cambridge University Press, Oct.1999

[2] R A. Smith, "Detectors for ultraviolet, visible, and infrared radiation", Appl. Opt., vol. 4, pp. 631-638, 1965

[3] Maurus Tacke, "Lead salt lasers," Philosophical transactions of Royal society of London, A, 2001, 359-547

[4] Norton, P. and Tacke, M., "MBE of $Pb_{1-x}Eu_xSe$ for the use in IR devices", J. Crystal Growth 81, 1987, 405

[5] Y. Shani, A. Katzir, M. Tacke, and H. M. Preier, "$Pb_{1-x}Sn_xSe/Pb_{1-x-y}En_ySn_xSe$ corrugated diode lasers," IEEE J. Quantum Electron., vol. 25, no. 8, p. 1828, 1989.

[6] Uwe Peter Schiebl, Hans-Edwin Wagner, Michael Hodges, " Lead salt lasers: room temperature operation and other recent developments," SPIE, vol. 3758, 0277-786X/99, July 1999, 81

[7] Irina T. Sorokina, Konstantin L. Vodopyanov, "Solid-state mid-infrared laser sources," Berlin; New York: Springer, 2003.

[8] Hong K. Choi, “Long-wavelength infrared semiconductor lasers,” Wiley series in lasers and applications, John wiley and sons, Inc. publication, 2004.

[9] Feit, Z., McDonald, M., Woods, R.J., Archambault, V., Mak, P., “Low threshold PbEuSeTe/PbTe separate confinement buried heterostructure diode lasers”, Applied Physics Letters, 68, 1996, 738-740.

[10] J. Faist, F. Capasso, D. L. Sivco, C. Sirtori, A. L. Hutchinson, and A. Y.Cho, “Quantum cascade laser,” Science, vol. 264, pp. 553–556, 1994

[11] Molecular Beam Epitaxy, edited by A. Y. Cho (AIP, Woodbury, NY,1994)

[12] Rui Yang, “Type-II Interband Cascade Lasers: Review and Prospects”, Maxion Technologies, Inc.
http://sinh.nrl.navy.mil/code6870/work2/yang_talk.pdf (Accessed 11/14/2006)

[13] Chih-Hsiang Lin, Rui Q. Yang, D. Zhang, S.J. Murry, S.S. Pei, A.A. Allerman and S.R. Kdrtz, “Type II interband quantum cascade laser at 3.8 μm”, ELECTRONICS LETTERS, Vol. 33, No. 7, pp 598-599, March 1997

[14] J.R. Meyer, L.J. Olafsen, E.H. Aifer, W.W. Bewley, C.L. Felix, I. Vurgaftman, M.J. Yang, L. Goldberg, D. Zhang, C.-H. Lin, S.S. Pei, and D.H. Chow, “Type II

W interband cascade and vertical-cavity surface-emitting mid-IR lasers", IEEE Proceedings – Optoelectronics, 1998,145, 275-280

[15] R F Kazarinov and R A Suris, "Amplification of electromagnetic waves in a semiconductor superlattice", Sov. Phys. Semicond. 5 707709, 1971

[16] J. Faist, F. Capasso, D. L. Sivco, C. Sirtori, A. L. Hutchinson, and A. Y. Cho, "Quantum cascade laser," Science, Vol. 264, pp. 553-556, 1994

[17] J. Faist, F. Capasso, C. Sirtori, DL Sivco, AL Hutchinson, and AY Cho, "Continuous wave operation of a vertical transition quantum cascade laser above T = 80 K", Appl. Phys. Lett., vol. 67, pp. 3057-3059, 1995

[18] J. Faist, F. Capasso, C. Sirtori, D. L. Sivco, A. L. Hutchinson, and A. Y. Cho, "Vertical transition quantum cascade laser with Bragg confined excited state," Appl. Phys. Lett., vol. 66, pp. 538–540, 1995.

[19] J. Faist, F. Capasso, C. Sirtori, D. L. Sivco, J. N. Baillargeon, A. L. Hutchinson, S. G. Chu, and A. Y. Cho, "High power mid-infrared (l~5mm) quantum cascade lasers operating above room temperature", Appl. Phys. Lett., Vol. 68, pp. 3680-3682, 1996.

[20] J. Faist, C. Gmachl, F. Capasso, C. Sirtori, D. L. Sivco, J. N. Baillargeon, and A. Y. Cho, “Distributed feedback quantum cascade lasers”, Appl. Phys. Lett, Vol.70, pp. 2670-2672, 1997.

[21] G. Scamarcio, F. Capasso, C. Sirtori, J. Faist, A. L. Hutchinson, D. L. Sivco, and A. Y. Cho, “High-Power Infrared (8-Micrometer Wavelength) Superlattice Lasers”, Science, vol. 276, pp. 773-776, 1997

[22] K. Namjou, S. Cai, E. A. Whittaker, J. Faist, C. Gmachl, F. Capasso, D. L. Sivco, and A. Y. Cho, "Sensitive absorption spectroscopy with a room-temperature distributed-feedback quantum-cascade laser," Opt. Lett., Vol. 23, pp. 219-221, 1998.

[23] Rui Q. Yang, JL Bradshaw, JD Bruno, JT Pham, DE Wortman, and RL Tober, “Room temperature type-II interband cascade laser”, Appl. Phys. Lett., Vol. 81, pp. 397-399, July 2002

[24] H Preier, INVITED PAPER, “Physics and applications of IV-VI compound semiconductor lasers”, Semicond. Sci. Technol. 5, (1990), S12-S20.

[25] K. Minoglou, E. D. Kyriakis-Bitzaros, E. Grivas, S. Katsafouros, A. Kostopoulos, G. Konstadinidis and G. Halkias, "Metallic bonding of optoelectronic dies to silicon wafers", "MMN 2004", November 14-17, 2004, Athens, Greece

[26] Richard R. Chromik, "Investigation of Mechanical Properties of Pb-Free Solders by Nanoindentation.", September 2002, Invited Speaker, Pb-Free Soldering Technology Symposium, SMTA International Annual Meeting

[27] Arnaud Gaetan Sow, "Packaging technology for IV-VI semiconductor laser fabrication," Master's thesis, Department of Electrical and Computer Engineering, University of Oklahoma

[28] Hutapea, P., Grenestedt, J.L., "Effect of Temperature on Elastic Properties of Woven Glass Epoxy Composites for Printed Circuit Board Applications," Journal of Electronic Materials, Vol. 32, No. 4, 2003, pp. 221-227

[29] C. Gmachl, F. Capasso, J. Faist, A. L. Hutchinson, A. Tredicucci, D. L. Sivco, J. N. Baillargeon, S. N. G. Chu, and A. Y. Cho, "Continuous wave and high power pulsed operation of index-coupled distributed feedback quantum cascade lasers," Appl. Phys. Lett., vol. 72, pp. 1430–1432, 1998

[30] T. Aellen, S. Blaser, M. Beck, D. Hofstetter, J. Faist, Emilio Gini, "Continuous-wave distributed-feedback quantum-cascade lasers on a Peltier cooler", Appl. Phys. Lett,, Vol 83, pp 1929, September 2003

[31] C. B. Roller, K. Namjou, J. Jeffers, M. Camp, P. J. McCann, and J. Grego, "Nitric Oxide Breath Testing Using Tunable Diode Laser Absorption Spectroscopy:

Application in Respiratory Inflammation Monitoring", Applied Optics 41, 6018 (2002)

[32] S. Barbieri, J. P. Pellaux, E. Studemann, and D. Rosset, “Gas detection with quantum cascade lasers: An adapted photoacoustic sensor based on Helmholtz resonance”, Review of Scientific Instruments, Vol. 73, pp. 2458-2461, June 2002

[33] Hecht, Eugene, ”Optics”, 2nd, chapter 5, Addison Wesley, 1987

[34] “Optical materials selection guide”, Janos Technology Inc, http://www.janostech.com/files/Optical%20Material%20Selection%20Giude.pdf, (Accessed 11/14/2006)

[35] Dennis W. Morelli "Interference Filter Handbook" Optical coating laboratory 1998

[36] “Circular Variable Filters (CVF)”, ISOCAM Observer's Manual, V1.0, Oct 1995

[37] A.K.G. Gattu, “A spectrometer for photoluminescence measurements of IV-VI mid-infrared diode laser materials”, The University of Oklahoma Master’s Thesis (2004)

[38] "JAMECO", Electronic components computer products http://www.jameco.com/wcsstore/Jameco/Products/ProdDS/105881.PDF, (Accessed 11/14/2006)

[39] Instruction Manual "LDC 3900Modular laser diode controller", ILX Light wave http://www.ilxlightwave.com/manuals/laser_diode_controller_LDC-3900_manual.pdf (Accessed 11/14/2006)

[40] "HgCdTe infrared detectors", P. Norton, OPTO-ELECTRONICS REVIEW 10(3), 159–174 (2002)

[41] Instruction Manual of PVI-2TE-5 detector, Vigo System, http://www.boselec.com/documents/VigoCatalogWWW4-26-05A.pdf#search=%22PVI-2TE-5%20detector%22 (Accessed 11/14/2006)

[42] "SR 830 DSP Lock-in amplifier operating manual and programming reference" Stanford research system Nov 2002

[43] "Steady state infrared emitters", Hawkeye technologies LLC

[44] Michael Fowler, "Blackbody Radiation ", University of Virginia 1997

[45] Liu, X., Hu, M., Nguyen, H., Caneau, C., Rasmussen, M., Davis, R. and Zah, C.-E., (2004) IEEE Trans. Adv. Packaging 27, 640–646.

[46] Arnaud Gaetan Sow,"Packaging technology for IV-VI semiconductor laser fabrication", University of Oklahoma, (2003).

[47] Chin C.Lee,"Fluxless bonding technology for high power laser diode arrays", Materials science and engineering, Pages 1-6, (1998-99).

[48] Manual of Thermal evaporator Denton Vacuum DV-502A system http://www.micromd.org/policyproc/files/L013-01A.pdf (Accessed 11/14/2006)

[49] Manual of K&S Model 4124 Ball Bonder http://www.engr.wisc.edu/centers/wcam/pdfs/goldbonder.pdf (Accessed 11/14/2006)

[50] Manual of Tencor P-1 Long Scan Profiler http://www.ncf.uic.edu/manuals/TencorManual.pdf (Accessed 11/14/2006)

[51] H. Okamoto and T. B. Massalski, "The Au-In system," in Phase Diagrams of Binary Gold Alloys, H. Okamoto and T. B. Massalski, eds. Metals Park, OH: ASM International, 1987, pp, 142-153.

[52] Xingsheng Liu, Martin Hai Hu, Hong Ky Nguyen, Catherine G. Caneau, Michael Heath Rasmussen, Ronald W. Davis, Jr., and Chung-En Zah, “Comparison between epi-down and epi-up bonded high-power single-mode 980-nm semiconductor lasers”, IEEE Transactions on advanced packaging, 27, 2004, 640-646

[53] R. Q. Yang, "Infrared Laser Based on Intersubband Transitions in Quantum well," Superlattices and Microstructures 17.1 (1995): 77

[54] R. Q. Yang, C. J. Hill, B. H. Yang, C. M. Wong, R. E. Muller, and P. M. Echternach, "Continuous-Wave Operation of Distributed Feedback Interband Cascade Lasers," Appl. Phys. Lett. 84.18 (2004): 3699-701

[55] J. L. Bradshaw, N. P. Breznay, J. D. Bruno, J. M. Gomes, J. T. Pham, F. J. Towner, D. E. Wortman, R. L. Tober, C. J. Monroy, and K. A. Oliver, "Recent Progress in the Development of Type II Interband Cascade Lasers," Physica E 20 (2004): 479-85

[56] Rui Q. Yang, J. L. Bradshaw, J. D. Bruno, J. T. Pham, D. E. Wortman and R. L. Tober, “Room temperature type-II interband cascade laser”, Applied Physics Letters, July 15, 2002, Volume 81, Issue 3, pp. 397-399

[57] "MIR 8000 MODULAR INFRARED FOURIER TRANSFORM SPECTROMETER" Instruction Manual Oriel Instruments

[58] Rui Q Yang, "Part of Inventory ICLs made from sample J435"

[59] Yasunori Saito, Tatsunori Kanaya, Akio Nomura, and Tetsuo Kano, "Experimental trial of a hollow-core waveguide used as an absorption cell for concentration measurement of NH3 gas with a CO2 laser", OPTICS LETTERS, Vol. 18, No. 24 / December 15, 1993, 2150

[60] M. B. Levy and K. D. Laakmann, Proc. Soc. Photo-Opt. Instrum. Eng., 605, 57(1986)

[61] A. Hongo, K. Morosawa, K. Matsumoto, T. Shiota, Y. Matsuura, and M. Miyagi, IEEE J. Quantum Electron. 26, 1510 (1990)

[62] M. Ibanescu, S. G. Johnson, M. Soljac˘ic´, J. D. Joannopoulos, and Y. Fink, "Analysis of mode structure in hollow dielectric waveguide fibers", PHYSICAL REVIEW E 67, 046608 (2003)

[63] OmniGuide Company, "Part of inventory: hollow waveguides"

[64] J. Graeme, "Photodiode Amplifiers", McGraw-Hill, New York (1996), p. 77

[65] G. Eppeldauer, "Chopped Radiation Measurements With Large Area Si Photodiodes", J. Res. Natl. Inst. Stand. Technol., 103 (2), 153-162 (1998)

[66] T. Katagiri, Y. Komachi, Y. Hattoria, Y. Matsuurac, M. Miyagid, H. Tashiroa, and H. Sato, "Hollow-optical fiber probe for confocal Raman endoscopy", Optical Fibers and Sensors for Medical Diagnostics and Treatment Applications VI, edited by Israel Gannot, Proc. of SPIE, Vol. 6083, 60830E, (2006)

[67] Y. Matsuura, T. Abel, and J. A. Harrington, "Optical properties of small-bore hollow glass waveguides", APPLIED OPTICS, Vol. 34, No. 30, p. 6842, 20 October 1995

[68] ISP Optics company, "Part of inventory: CaF_2 ball lenses"
http://www.ispoptics.com/New%20ISP%20Pages/page93b.pdf
(Accessed 11/14/2006)

APPENDIX A

Peak wavenumber, Band width and Intensity of the band pass spectrum of the filter wheel at various angles

Angle(degree)	Peak wave number(cm^{-1})	Intensity(au)	Band width (FWHM) (cm^{-1})	Band Width Difference (cm^{-1})
0	1873.1	0.68	1886-1845	41
2	1890.2	0.78	1903-1869	34
4	1893.4	0.65	1910-1876	34
6	1903.4	0.89	1927-1886	41
8	1910.4	0.82	1927-1886	41
10	1920.6	0.83	1930-1890	40
12	1937.5	0.86	1940-1907	33
14	1944.5	0.86	1957-1917	40
16	1957.2	1.01	1964-1927	37
18	1957.9	1.00	1971-1937	34
20	1971.2	0.98	1991.3-1951	40.3
22	1991.8	0.89	2005.6-1971	34.6
24	2005.4	0.87	2022.3-1981	41.3
26	2012.2	0.94	2029-1995	34
28	2015.6	0.75	2042-2005	37
30	2032.6	0.95	2056-2015	41
32	2046	0.9	2069-2029	40
34	2059.7	0.84	2080-2042	38
36	2073.3	0.92	2097-2046	51
38	2080.1	0.94	2103-2059	44
40	2097.2	0.95	2114-2069	45
42	2120.8	0.89	2137-2097	40
44	2134.4	1.01	2154-2114	40
46	2137.8	0.99	2158-2117	41
48	2151.4	0.91	2171-2127	44
50	2168.8	0.85	2188-2148	40
52	2171.7	0.84	2185-2144	41
54	2205	0.91	2226-2185	41
56	2215	0.63	2236-2195	41
58	2232	0.62	2249-2205	44
60	2239	1.00	2266-2219	47
62	2263	0.91	2287-2239	48
64	2280	0.81	2300-2263	37

66	2300.7	0.84	2314-2276	38
68	2300.7	0.84	2314-2276	38
70	2314	0.45	2334-2293	41
72	2344.8	0.43	2365-2321.1	43.9
74	2375	0.35	2395-2338	57
76	2385.3	0.67	2402-2365	37
78	2392	0.66	2412-2375	37
80	2405	0.69	2433-2385	48
82	2429	0.69	2456-2409	47
84	2456	0.63	2484-2429	55
86	2470	0.64	2497-2443	54
88	2480.3	0.57	2507-2460	47
90	2504.1	0.60	2528-2477	51
92	2531	0.64	2555-2500	55
94	2551	0.37	2579-2521	58
96	2565	0.35	2596-2541	55
98	2582	0.36	2599-2558	41
100	2606	0.56	2633-2579	54
102	2636	0.45	2660-2612	48
104	2660.3	0.35	2687-2633	54
106	2677	0.42	2718-2660	58
108	2687	0.43	2718-2660	58
110	2718	0.45	2745-2691	54
112	2745	0.45	2779-2721	58
114	2762	0.25	2803-2738	65
116	2792	0.35	2826-2765	61
118	2806	0.30	2833-2769	64
120	2837	0.28	2860-2806	54
122	2860	0.27	2901-2833	68
124	2904	0.25	2932-2877	55
126	2932	0.22	2955-2891	64
128	2938	0.21	2962-2898	64
130	2979	0.24	2999-2942	57
132	2999	0.13	3047-2982	65
134	3030	0.22	3064-3006	58
136	3057	0.18	3091-3030	61
138	3084	0.18	3111-3040	71
140	3115	0.18	3139-3077	62
142	3135	0.09	3169-3125	44
144	3176	0.07	3213-3162	51
146	3213	0.12	3254-3173	81
148	3223	0.15	3254-3193	61
150	3264	0.07	3264-3240	24
152	3305	0.1	3325-3274	51
154	3335	0.13	3386.8-3298	88.8

156	3386	0.07	3403-3380	23
158	3410.2	0.13	3430-3366	64
160	3441	0.08	3468-3417	51
162	3495	0.14	3519-3461	58
164	3536	0.11	3549-3509	40
166	3559	0.1	3583-3549	34
168	3573	0.13	3600-3559	41
170	3593	0.12	3624-3573	51
172	3621	0.11	3651-3597	54
174	3654	0.09	3688-3624	64
176	3658	0.15	3671-3624	47
178	3658	0.1	3675-3627	48
180	3627	0.13	3641-3593	48
182	3593	0.14	3624-3566	58
184	3546	0.1	3583-3512	71
186	3525	0.11	3539-3492	47
188	3509	0.11	3556-3464	92
190	3458	0.09	3481-3427	54
192	3417	0.12	3451-3393	58
194	3383	0.13	3420-3356	64
196	3369	0.16	3386-3328	58
198	3356	0.12	3369-3325	44
200	3308	0.15	3332-3285	47
202	3268	0.14	3305-3220	85
204	3227.3	0.17	3227-3200	27
206	3193	0.11	3223-3166	57
208	3189.9	0.15	3213-3159	54
210	3145	0.17	3176-3108	68
212	3108.5	0.17	3142-3074	68
214	3077	0.18	3098-3054	44
216	3044	0.18	3091-3023	68
218	3050	0.24	3074-3023	51
220	3010	0.24	3044-2979	65
222	2962	0.14	2993-2942	51
224	2945	0.24	2965-2915	50
226	2915	0.23	2942-2881	61
228	2908	0.27	2939-2881	58
230	2864	0.29	2891-2833	58
232	2840	0.30	2870-2813	57
234	2813	0.30	2850-2786	64
236	2789	0.2	P2816-2758	58
238	2779	0.39	2803-2755	48
240	2735	0.45	2765-2708	57
242	2721	0.42	2748-2694	54
244	2694	0.41	2718-2663	55

246	2674	0.5	2697-2650	47
248	2670	0.52	2691-2646	45
250	2636	0.53	2660-2602	58
252	2606	0.58	2636-2582	54
254	2582	0.49	2612-2555	57
256	2562	0.59	2592-2548	44
258	2555	0.6	2579-2524	55
260	2524	0.61	2545-2497	48
262	2497	0.60	2524-2480	44
264	2484	0.67	2524-2473	51
266	2467	0.70	2487-2439	48
268	2453	0.65	2480-2429	51
270	2426	0.68	2450-2420	30
272	2402	0.55	2422-2378	44
274	2388	0.48	2405-2372	33
276	2378	0.53	2395-2358	37
278	2372	0.37	2388-2341	47
280	2341	0.37	2365-2317	48
282	2317	0.66	2331-2300	31
284	2300	0.74	2321-2273	48
286	2290	0.78	2317-2270	47
288	2276	0.81	2297-2260	37
290	2253	0.99	2270-2232	38
292	2239	0.8	2260-2219	41
294	2229	0.95	2249-2202	47
296	2219	1.00	2236-2192	44
298	2205	1.00	2226-2181	45
300	2188	1.01	2209-2168	41
302	2164	0.89	2192-2144	48
304	2148	0.94	2171-2127	44
306	2141	0.94	2164-2124	40
308	2131	0.9	2151-2110	41
310	2110	0.98	2137-2086	51
312	2100	1.02	2117-2083	34
314	2083	0.48	2103-2066	37
316	2076	0.87	2100-2056	44
318	2063	0.74	2086-2049	37
320	2049	0.89	2076-2025	51
322	2039	0.73	2056-2019	37
324	2022	0.78	2042-1998	44
326	2015	0.94	2032-1995	37
328	2008	0.93	2029-1991	38
330	1991	0.87	2012-1974	38
332	1974	0.97	1995-1957	38
334	1961	0.74	1981-1947	34

336	1951	0.89	1971-1934	37
338	1947	0.85	1968-1934	34
340	1930	0.79	1947-1913	34
342	1913.2	0.91	1930-1896	34
344	1907	0.83	1927-1893	34
346	1896.3	0.82	1917-1883	34
348	1893.2	0.71	1913-1869	44
350	1879	0.74	1900-1866	34
352	1873.2	0.8	1886-1852	34
354	1866	0.82	1883-1852	31
356	1869	0.70	1890-1852	38
358	1869	0.73	1886-1852	34
360	1876	0.54	1896-1859	37

APPENDIX B

Manual for labview program in filter wheel based mid-infrared sprectrometer

To utilize this system a few steps should be taken:

1. The signal from the Lock-in Amplifier or other analog source should be placed on one of the eight (0-7) ACH channel. Again the correct number should be placed in the box labeled 'Analog Channel'. Similarly the clock signal if from one of the eight (0-7) digital channels on the DAQ board. Both of these values can't be changed once the are selected during the 'Calibrate.vi' seesion.

Note: The system has no way of knowing if you placed the signal on a different channel so if the above is not done correctly the user may get erroneous data.

Simple Instructions:

1.) Calibrate the system to 0 degree when promted to do so.

2.) Enter the starting and ending angles in the appropiated boxes.

3.) Press the 'Run Test' button to begin

If the above setting are made and the computer is calibrated to the 0 degree position at the beginning (or recalibrated via the front panel button) there should be no problems with the test. After the test is done and is not stopped by the 'Stop' button, a window will be displayed with a picture of the data on a graph.

The user then has three option:

1.) Save Data- To save the data as a CSV (comma separated value) test file for importing into SigmaPlot, MS Excel or similar spreadsheet program.

2.) Save Picture- To save the picture as a JPEG file. Note the picture will be the graph as seen on the screen.

3.) Close Window- This will close the window and return back the the optical system screen.

If ever the system diplayed angle and the actual angle on the filter wheel system don't match simple press the recalibrate button to input the correct value.

If the user ever wishes to simply move to a specific angle then he or she should enter the same desired angle in the 'starting angle' parameter then press the reposition switch. The system will update itself, but no measurements will be made.

Definition of the controls and indicators-

System Parameters:

Analog/Digital Channel- These indicators display the value selected by the user at the beginning of the program. Note these values can not be changed once they have been selceted during the 'Calibrate.vi' seesion.

# of Co-Adds- This selects the number of times the system scan the selected range of angles. The values are added together then averaged and the averaged value is displayed on the graph. The default is 10 co-adds and it take approximately 10 seconds per scan. The minimum and maximum value for this control are 2-400.

Starting Angle, Ending Angle- These controls allow the user to define the angles for which measurements will be taken. The user must put in the starting and ending angle. The computer will do the rest once the test start.

System Data:

Current Calculated Position- This tells what position the filter wheel should be in. Remember the computer has no sensor on the wheel so this valued is calculated and updated throught the test.

Current Scan- This is a counter which tell how many scans the computer has completed.

Lock-In Reading- This is the current reading on the corresponding analog channel. The channel selected should be that of the lock-in amplifier.

Created By: M. A. Evans on June 18, 2003

Updated by Rajesh and Chun on Jan 26, 2005

APPENDIX C

List of acronyms and symbols

Acronyms

ADC : Analog to digital converter (A/D)

AC : Alternating current

CaF_2 : Calcium Fluoride

CCTV: Closed circuit television

CSV : Comma separated value

CVF : Circular variable filter

CW : Continuous wave

DAQ : Data acquisition card

DC : Direct current

EFL : Effective focal length

FTIR : Fourier Transform Infrared

FWHM: Full width half maximum

IR : Infrared

InGaAs: Indium Gallium Arsenide

InGaP : Indium Gallium Phosphide

LED : Light emitting diode

LDC : Laser diode controller

MCT : Mercury Cadmium Telluride

MCZT : Mercury Cadmium Zinc Telluride

MIR : Mid-infrared

MBE : Molecular beam epitaxy

MQW : Multiple quantum well

NO : Nitric Oxide

OAPM : Off-axis parabolic mirror

PbSe : Lead Selenide

PbSrSe : Lead Strontium Selenide

PSD : Phase sensitive detector

PL : Photoluminescence

PLL : Phase locked loop

QC : Quantum cascade

REFL : Reflected effective focal length

SNR : Signal-to-noise ratio

TEC : Thermo-electric cooler

TDLAS : Tunable diode laser spectroscopy

ZnSe : Zinc Selenide

Symbols

III-V : Compounds made of elements that belong to the third and fifth columns of the periodic table

IV -VI: Compounds made of elements that belong to the fourth and sixth columns of the periodic table

θ : Angle of circular variable filter wheel

au : Arbitrary unit

cm^{-1} : Per centimeter (Units of wavenumber)

c : Speed of light

D : Diameter

Eg : Energy gap

ε : Emissivity

eV : Electron Volts

h : Plank constant

Hz : Hertz

γ : Wavenumber

λ : Wavelength

υ : Frequency

KHz : Kilohertz

K : Boltzmann constant

mV : Millivolt

MHz : Megahertz

nm : Nanometer

μV : Microvolt

mA : Milliampere